

Convective Wind Fields as Investigated with Doppler Lidar

By
Bonnie F. Weber

PI: Freeman F. Hall and Pete Sinclair

Department of Atmospheric Science
Colorado State University
Fort Collins, Colorado



**Department of
Atmospheric Science**

Paper No. 411

CONVECTIVE WIND FIELDS AS INVESTIGATED
WITH DOPPLER LIDAR

by

Bonnie Faye Weber

Research Supported by the
Internal NOAA/ERL Research Program

Investigators: Freeman F. Hall
Peter C. Sinclair

Department of Atmospheric Science
Colorado State University
Fort Collins, Colorado 80523

June 1987

Atmospheric Science Paper No. 411

ABSTRACT

The objective of this research was to evaluate a Doppler laser remote sensor (lidar) in the measurement of mean wind and the temporal and spatial distribution of convective elements and other perturbation features in the planetary boundary layer. Mean wind measurements from the lidar were compared to anemometry time series from the Boulder Atmospheric Observatory tower, to determine agreement between the different sensors. The lidar and tower mean flow estimates were found to agree within 1 ms^{-1} during a variety of weather conditions. Mean wind fields were removed from the lidar returns and perturbation fields were then examined. Features detected by the lidar were examined for consistency in time and space. The lidar was demonstrated to be a useful tool for the study of the time history and spatial distribution of perturbation fields.

ACKNOWLEDGEMENTS

Freeman F. Hall, of NOAA/ERL/WPL staff helped choose the convective plume structure theme; monitored the progress of the research; and made available the resources of the Doppler Lidar Program. Peter Sinclair, of Colorado State University helped to focus the research effort. Boulder Atmospheric Laboratory data and interpretation assistance was provided by Chandran Kaimal, E. E. Gossard, and John Gaynor, all on the WPL staff. R. M. Hardesty developed the original lidar data analysis computer codes and participated in the data collection along with T. Rhidian Lawrence and Ronald A. Richter. William Cotton of the Atmospheric Science Department and Chaio-Yao She of the Physics Department at Colorado State University provided constructive criticism and support.

NOAA's Wave Propagation Laboratory and the University of Colorado's Cooperative Institute for Research in the Environmental Sciences provided financial support.

TABLE OF CONTENTS

	<u>Page</u>
1. INTRODUCTION	1
1.1 Historical Perspective	1
1.2 Lidar	2
1.3 Doppler Processing	3
1.4 Radar/Lidar Comparison	4
2. THE LIDAR INSTRUMENT	6
2.1 The Laser and Optics	6
2.2 Operation and Use	7
2.3 Processing	9
3. MEAN WIND COMPARISON	12
3.1 Introduction	12
3.2 Tower Site and Data	12
3.3 Lidar Processing	16
3.3.1 Mean Wind Calculation	21
3.3.2 Parcel Processing	21
3.4 Comparison Results	27
3.4.1 Data Set	27
3.4.2 Wind Speed Comparison	33
3.4.3 Wind Direction Comparison	38
4. INVESTIGATION OF THE FLUCTUATING FLOW VELOCITY FIELD	44
4.1 Theoretical Considerations	44
4.2 Investigating the Non-Mean Wind Field	45
4.2.1 Experimental Plan	46
4.2.2 Description of Received Wind Field	46
4.2.3 Expected Structures	48
4.2.4 Deviation Field Analysis	51
4.2.5 Cases Analyzed	52
4.2.5.1 One Dimensional Case	52
4.2.5.2 VAD Case	53
4.2.5.3 Combination Vertical and Horizontal Scan	62
5. RESULTS AND CONCLUSIONS	63
6. FUTURE WORK	67
7. REFERENCES	69
APPENDIX A: Tower Data	74
A.1 Data Archiving	75
A.2 Sonic Anemometer Processing	75
A.3 Propeller-Vane Anemometer Processing	81

CONTENTS (continued)

	<u>Page</u>
APPENDIX B: The Velocity-Azimuth Display Technique	88
B.1 Characteristics of a VAD Scan	90
B.2 Wind Velocity Derivation	90
APPENDIX C: Velocity-Azimuth Technique Derivation	92
APPENDIX D: Tower Atmospheric Data and Corresponding Stability Information for Time Periods During Lidar/Tower Mean Wind Comparison	96
APPENDIX E: Analyses of the Mean Wind	103
E.1 Analysis of the Mean Wind with a First Harmonic Fit	104
E.2 Analysis of the Mean Wind with a First and Second Harmonic Fit	105
E.3 Conclusions	106

LIST OF FIGURES

	<u>Page</u>
Figure 1.1 Geometry for Doppler shift	4
Figure 2.1 Schematic of the NOAA lidar optics	7
Figure 2.2 Range-weighting function for the NOAA Doppler lidar	8
Figure 2.3 Data stream for NOAA Doppler lidar	9
Figure 3.1 Site plan for BUCOE experiment	13
Figure 3.2 Geographical location and general topography of the Boulder Atmospheric Observatory	13
Figure 3.3 BAO Tower	14
Figure 3.4 View of three-axis sonic anemometer	17
Figure 3.5 View of propeller-vane anemometer	17
Figure 3.6 VAD technique and sample VAD resultant scan	18
Figure 3.7 Geometry of 80 degree zenith angle scan as used in the lidar/tower comparison	22
Figure 3.8 Schematic of gate sliding technique as used in the lidar/tower comparison	23
Figure 3.9 Plot of VAD mean wind direction and speed versus radial range	24
Figure 3.10 Taylor's hypothesis as applied to a tower time series and a VAD run space series	26
Figure 3.11 Contour plot of terrain around BAO	26
Figure 3.12 Lidar/tower wind sensor comparison	31
Figure 3.13 Tower sonic/prop sensor comparison	32
Figure 3.14 Polar plot of wind direction deviation pattern for low wind speed cases	39
Figure 4.1 Large feature scaling for lidar VAD scan	48
Figure 4.2 Horizontal area covered by VAD scan made by the Doppler lidar	50
Figure 4.3 Thermal scale features	50

LIST OF FIGURES (continued)

		<u>Page</u>
Figure 4.4	Reflection in VAD field of vertical velocity changes expected in a convective plume	52
Figure 4.5	Radial analysis of deviation flow pattern for 60 degree arc around the mean wind direction	54
Figure 4.6	Trace of the movement of the feature identified in Figure 4.5 a and b	55
Figure 4.7	Vertical/horizontal displacement versus radial range for the area covered with a VAD scan done at 6 degrees elevation	56
Figure 4.8	Contour plot from a series of three contiguous VAD scans	57
Figure 4.9	Highlighted areas with similar features in consecutive scans	60
Figure 4.10	Velocity distribution analysis by quadrant	61
Figure 4.11	Highlighted thermal scale features seen in consecutive scans	62
Figure 4.12	Height analysis of elevation stepping sector scans . . .	64
Figure 4.13	Composite vertical plot of one radial belt as seen through eight consecutive elevation stepping sector scans	65
Figure 4.14	Vertical velocity plot as seen by Doppler sodar	65
Figure A.1	Sample of BAO "M" data sheet	76
Figure A.2	Sample of BAO "G" data sheet	77
Figure A.3	Sample of BAO "A" data sheet	77
Figure A.4	Sonic data from the 300 m level on the BAO tower	78
Figure A.5	Examples of wind profiles from tower sensors during BUCOE	79
Figure A.6	Two-minute data series of raw sonic data from BAO tower.	80
Figure A.7	Rotated sonic components	82
Figure A.8	"G" data sequences from tower data	83
Figure A.9	Average, or "A" data sequence derived from sonic along/across components	84

LIST OF FIGURES (continued)

	<u>Page</u>
Figure A.10 Sample prop data series from the 300 m level boom on the BAO tower	85
Figure B.1 Example of conic section explored when using a VAD scan technique	89
Figure B.2 Sample wind fields and their reflection as seen on a VAD	91

LIST OF TABLES

	<u>Page</u>
Table 2.1 NOAA Doppler lidar raw data mode specifications	10
Table 2.2 NOAA Doppler lidar moment processor specifications	11
Table 3.1 Tower instrumentation	15
Table 3.2 Dates and times of VAD runs at 80 degrees zenith angle during BUCOE experiment	18
Table 3.3 BAO archive record for BUCOE	19
Table 3.4 Summary of VAD and tower run times used in the lidar/tower wind comparison	28
Table 3.5 Weather conditions during lidar/tower wind comparison study	29
Table 3.6 Wind speed and direction summary for lidar/tower comparison	30
Table 3.7 Wind speed error calculation for lidar/tower comparison	33
Table 3.8 Wind direction error calculation for lidar/tower comparison	34
Table 3.9 Wind speed comparison sorted by magnitude	35
Table 3.10 Wind speed error calculation for lidar/tower comparison sorted by wind speed	36
Table 3.11 Wind speed error calculation within tower shadow	39
Table 3.12 Lidar/tower wind direction comparison sorted by wind speed	41
Table 3.13 Lidar/tower wind direction comparison sorted by wind direction	42
Table 3.14 Wind direction error calculation within tower shadow	43
Table A.1 Component averages versus speed averages for selected propeller vane examples during lidar/tower comparison	87
Table E.1 Samples of least squares algorithm fit tests results	107

CONVECTIVE WIND FIELDS AS INVESTIGATED WITH DOPPLER LIDAR

ABSTRACT. The objective of this research was to evaluate a Doppler laser remote sensor (lidar) in the measurement of mean wind and the temporal and spatial distribution of convective elements and other perturbation features in the planetary boundary layer. Mean wind measurements from the lidar were compared to anemometry time series from the Boulder Atmospheric Observatory tower, to determine agreement between the different sensors. The lidar and tower mean flow estimates were found to agree within 1 ms^{-1} during a variety of weather conditions. Mean wind fields were removed from the lidar returns and perturbation fields were then examined. Features detected by the lidar were examined for consistency in time and space. The lidar was demonstrated to be a useful tool for the study of the time history and spatial distribution of perturbation fields.

1.0 INTRODUCTION

The objective of this research was to determine if pulsed Doppler lidar is a useful tool for investigating boundary layer dynamics. We conclude that it can be quite useful.

The groundwork for the application of lidar to atmospheric wind detection owes much to developments in laser and radar research. A brief history of earlier work tracing some of the developments in the techniques and theories leading to the present study follows.

1.1 Historical Perspective

The first radars were developed for the detection of aircraft, ships, and precipitation (Ridenour, 1947). Radio frequencies have been used to study various atmospheric phenomena including inverted u-shaped echoes in vertical sections (Atlas, 1959), doughnut and ring structures (Hardy and Ottersten, 1969), and stratifications (Metcalf and Atlas, 1973). Recent developments have allowed detection of clear-air phenomena by means of refractive index gradients (Gossard and Strauch, 1981). The development of Doppler radars (Dobson, 1970; Browning et al., 1972; Gage and Balsley, 1978) has allowed the investigation of velocities, turbulence parameters, and target backscatter statistics.

Similarities exist in the measurements taken by radar and lidar systems, allowing much of the theory developed for the radar systems to be applied to

lidar systems. Major differences in the instruments are related to the differences in their wavelengths and pulse structures. The characteristic wavelengths of the instruments react to different atmospheric constituents, and therefore have different return patterns which identify same atmospheric phenomena. Pulse averaging characteristics of lidar systems require the use of intrapulse averaging, whereas phase coherent radar systems use pulse-to-pulse measurements (Hardesty et al., 1983b).

1.2 Lidar

The term LIDAR (LIght Detection And Ranging) was first used by Middleton and Spilhaus (1953) with reference to ceilometry using light beams. Lasers provide monochromatic light at defined wavelengths, which is backscattered at sufficient power levels to allow electronic detection and processing of the backscattered radiation. Scattering of laser radiation by aerosols or molecules forms the basis of atmospheric remote sensing with lasers. Early uses of optical wavelengths in atmospheric studies go back to the 1930's (Hulbert, 1937), with pulsed arc light being used in the 1930's and 40's to study the upper atmosphere. In 1963 Ligda of Stanford Research Institute operated the first lidar using a laser, calling it an "optical/radar" (Ligda, 1963). The earliest lasers used in atmospheric studies were the pulsed ruby and Neodymium glass types. Later devices used CO₂ gas, YAG crystals, and a variety of other media to obtain monochromatic light at different wavelengths (Hinkley, 1976). The first use of lasers in flow measurements was reported in 1964 by Yeh and Cummings, who employed a helium-neon instrument.

Lidar systems contain 1) a laser, which provides a coherent source of optical radiation, 2) an optical system through which the energy is transmitted to the atmosphere, and 3) a detection system for the scattered energy. The returns are analyzed to yield information about atmospheric properties. The lidar equation governing the returns is given by (Hinkley, 1976)

$$P_r(R) = P_o(c\tau/2) \beta(R) A_r R^{-2} \exp[-2 \int_{\phi}^R \alpha(r) dr]$$

P_o = transmitter power at t_o

c = velocity of light

τ = pulse duration

$\beta(R)$ = backscattering coefficient

R = range

A_r = effective receiver area

α = volume extinction coefficient of atmosphere in cm^3/cm^2

$P_r(R)$ = instantaneous power received at time $(\tau - t_o)$.

1.3 Doppler Processing

The laser's pulsed light from the transmitter interacts with aerosols moving at various velocities and is scattered. The scattered light has been shifted in frequency in a phenomenon known as the "Doppler shift," first seen in experiments in sound by the 19th century German physicist Doppler (Watrasiewicz and Rudd, 1976). This shift is caused by the movement of the scattering center by the wind. Ditchburn (1953) showed that the Doppler shift is given to the first order by

$$f_D = -2\vec{k}_o \cdot R$$

given - magnitudes \vec{k}_o , \vec{k}_s approximately equal,

f_D = frequency shift,

\vec{k}_o = incident wave vector,

k_s = scattered wave vector,

R = scatter velocity vector.

Figure 1.1 gives a diagram of the phenomenon (Eberhard, 1979) with the geometry of a Doppler experiment. Durst et al. (1976) reviewed the Doppler laser techniques used in laboratory fluid dynamic measurements. Additional problems dealing with the use of Doppler measurements in the atmosphere are pointed out in Owens (1969).

Because there is a frequency width to the Doppler spectrum due to Doppler uncertainty (Watrasiewicz and Rudd, 1976), various techniques of analyzing the

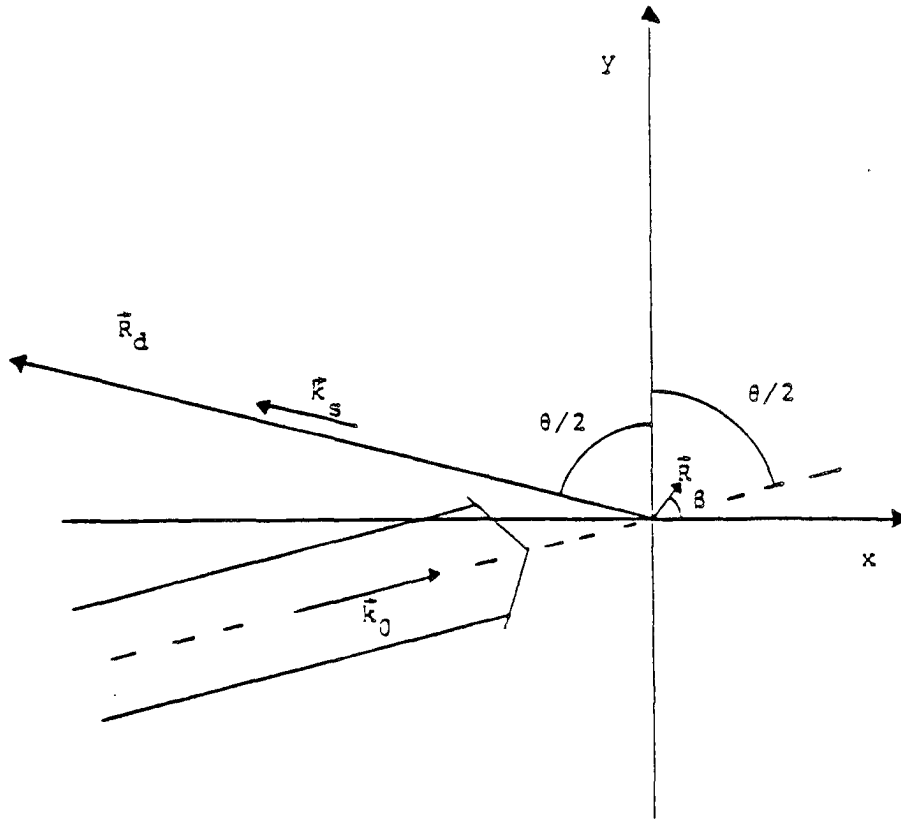


Figure 1.1. Geometry for Doppler shift (from Eberhard, 1979) generalized for any incident angle θ , with k_0 being incident wave vector with wavelength k_0 , k_s scattered wave vector with wavelength k_s , and r being environmental wind velocity.

Doppler spectrum have been investigated. These include analog filtering (Patel and Peach, 1976), FFT spectral analysis techniques, and pulse pair techniques (Zrnic, 1977). Sirmans and Baumgarner (1974) analyzed five different estimator techniques. Keeler (1980) analyzed the various techniques as they applied to the NOAA lidar. The technique of choice for the NOAA lidar was determined to be complex covariance processing.

1.4 Radar/Lidar Comparison

Though radar and lidar share some characteristics, there are also major differences between the two sensors. Some of the major differences lie in (1) operating wavelengths, (2) side lobe characteristics, (3) distribution in the atmosphere of the scatterers which the systems sense, (4) behavior in clouds, and (5) range that the systems sense.

The wavelength for lidar sensor in this study is 10 micrometers (μm). A typical radar sensor operates at 10 cm. The ratio between the two wavelengths is on the order of 10,000, which also represents the ratio of the particle sizes the sensors sense efficiently. An example of the type of particle easily sensed by the radar systems would be a raindrop with a radius of 5 mm, whereas the lidar target is an aerosol with a 0.5- μm radius, or particle size ratio of 10,000.

The second major difference in the two sensing systems lies in the differing effect of the side lobes on the reflection pattern. In both cases, side lobes, according to diffraction theory, must exist but their importance depends on the beamwidth, B , defined as approximately the wavelength divided by the diameter of the antenna area (Jenkins and White, 1937). The beam width of a typical radar is approximately 0.03 radians, that of a lidar, 0.00003 radians. The first side lobe will be down by 13 dB in both systems, but the angle to the side lobe, $3B/2$, is much greater in the radar, leading to a more significant effect on the data.

The next major difference between lidar and radar systems lies in the distribution of the respective scatters in the atmosphere. The radar targets include large raindrops and hail, which are localized in or below the clouds when they occur. The aerosols that supply the targets for the lidar are generally well mixed in an air mass. The uneven distribution of strongly scattering targets may lead to side-lobe-induced ambiguity in the radar system, which does not affect the lidar system. One of the advantages of radar lies in its ability to penetrate clouds. The lidar system is superior for detecting aerosol scattering in a clear atmosphere, but is unable to penetrate clouds owing to scattering attenuation from the cloud droplets that are large compared with the lidar wavelength.

The final major area in which the lidar and radar systems vary is in the ranges the systems sense. The maximum possible range can be determined by the square root of the power-aperture product. For the radars the power is usually on the order of 1 MW, whereas the lidar operates at 100 KW, a ratio of 10 to 1. The aperture of the radars is usually on the order of 3 m, whereas the lidar aperture is approximately 0.03 meters, a ratio of 100 to 1. Overall this gives a ratio of the square root of 1000, or 30. This ratio indicates that the radar can sense 30 times farther than the lidar sensor, or 300 km compared with 10 km.

2. THE LIDAR INSTRUMENT

The lidar instrument used in this research was the NOAA pulsed, coherent, hybrid, transversely-excited atmospheric pressure (TEA), CO₂ Doppler lidar. The system is discussed by Lawrence et al. (1983). It operates in a heterodyne mode at a wavelength of 10.6 μm .

2.1 The Laser and Optics

The transmitter laser is a hybrid-TEA design consisting of (1) a quasi-CW (continuous wave) conventional low pressure gain medium and (2) a near atmospheric pressure, transverse flow, transversely excited, UV preionized medium. The transmitter laser is operated on the P20 line of the 00 1^o-10 0^o band of the CO₂ spectrum when used for velocity measurements.

The UV preionized TEA laser is seeded by the quasi-CW portion of the instrument and produces horizontally polarized pulses of a set duration (2.0-3.3 μm) and pulse repetition rate, typically between 1 and 25 Hz (pulses per second). During the interpulse period, the low-pressure medium provides a CW output that is used to center the cavity at the P20 line center for maximum power. This centering is achieved by controlling the transmitting cavity piezo-transducer (PZT) with the output of a hill-climbing servo-loop, which derives its input from a detector monitoring the output of the laser.

A local oscillator (LO) laser is used to provide the heterodyne feature of the system. The LO's PZT is controlled from a servo-loop using the output from a detector measuring the beat frequency between the quasi-CW component of the transmitter laser and the LO. A 20-MHz offset is maintained.

The LO and transmitter laser are clamped just prior to TEA laser firing, and a pulse is then generated at the preset wavelength. Diffraction gratings are used to make the system line tunable.

The energy is directed first through a germanium Brewster coupler, which acts in the system as a transmit/receive (T/R) switch. It is then sent into a ZnSe Fresnel prism, which changes the polarization to circular. From there the beam enters an 11-inch aperture, parabolic-parabolic, off-axis telescope. The beam is then directed to the scanner by a 16-inch flat mirror.

The backscattered Doppler-shifted radiation passes through the Fresnel prism and is changed to vertical polarization. The radiation is reflected from the T/R switch onto the detector, and photomixed with radiation from the LO laser. The beat signal is then amplified, processed, displayed, and recorded digitally on tape. Figure 2.1 shows the configuration of the optics in the system.

Top View: NOAA Lidar Optics

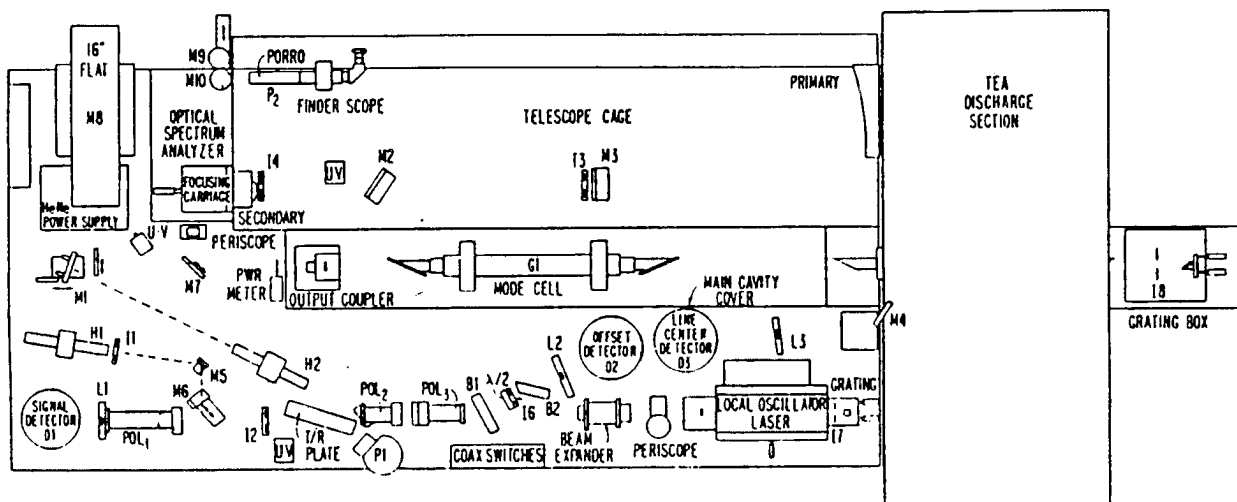


Figure 2.1. Schematic of the NOAA lidar optics (from Post, 1985).

2.2 Operation and Use

A pulsed lidar sends out a packet of light of given duration and wavelength (McCormack, 1975), in our case $10.6 \mu\text{m}$. Some of the light sent out will be intercepted by aerosols. For the wavelength in the NOAA system, the intercepted aerosol population is dominated by aerosols $1-3 \mu\text{m}$ in diameter (Post et al., 1978). The backscattered light is collected by the scanner and sensed by the receiver electronics. Ranging is achieved by observing the signal at various delay times and is given by multiplying the time from sending to receiving by one-half the speed of light (James, 1980).

$$r = c/2 (t_o - t_r)$$

t_o = time of signal sending

t_r = time of return signal receiving

c = speed of light

r = range.

Difficulties in the interpretation of the returns can be introduced by speckle, size-dependent scattering by the aerosols, and by pulse frequency chirp (Post et al., 1981). Discussion of the characteristics of a lidar signal is contained in Hinkley (1976). Hardesty (1984) discussed characteristics of the laser signal for the NOAA instrument.

Additional problems in interpreting returns from the packet of light lie in the structure of the packet itself and the observation window. The range-weighting function, i.e., the relative contribution of the scatterers from each range to the measured signal at a given point in time, is a function of the pulse intensity profile, backscatter structure, system range response, and observation window characteristic (Hardesty, 1984). The range-weighting function for the 3.3 μm pulse used in the investigations in this report is given in Figure 2.2.

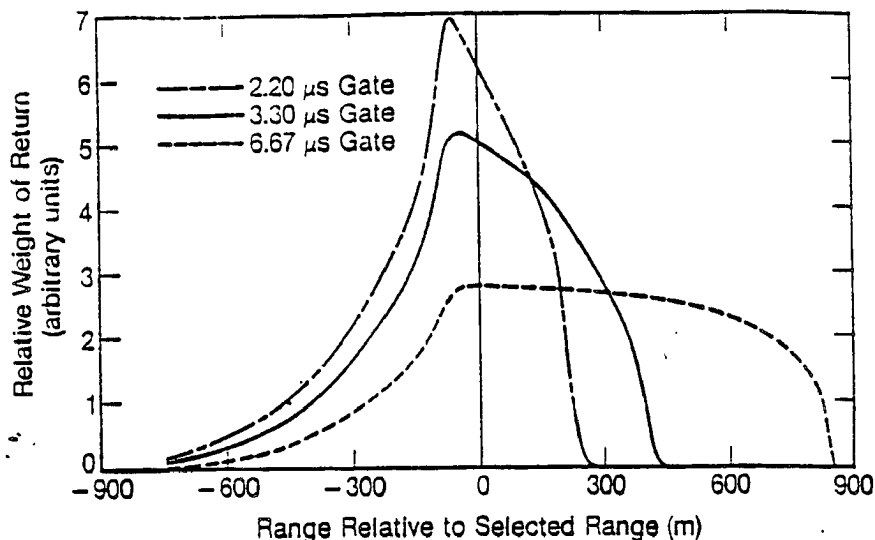


Figure 2.2. Range weighting function for the NOAA Doppler lidar (from Hardesty, 1984).

2.3 Processing

Data are collected by the lidar system in one of two modes. The data stream for the data from the receiver electronics is given in Fig. 2.3. Raw Data mode (path r) transfers the data from the system digitizer to magnetic tape, which is then post-processed at Boulder Lab Site (BL) into velocities. Moment Data (path m) are sent from the system to a hardware processor, which outputs the zeroth, first, and second moments of the Doppler spectrum. These moment data can be used for a real-time color display or transferred to magnetic tape.

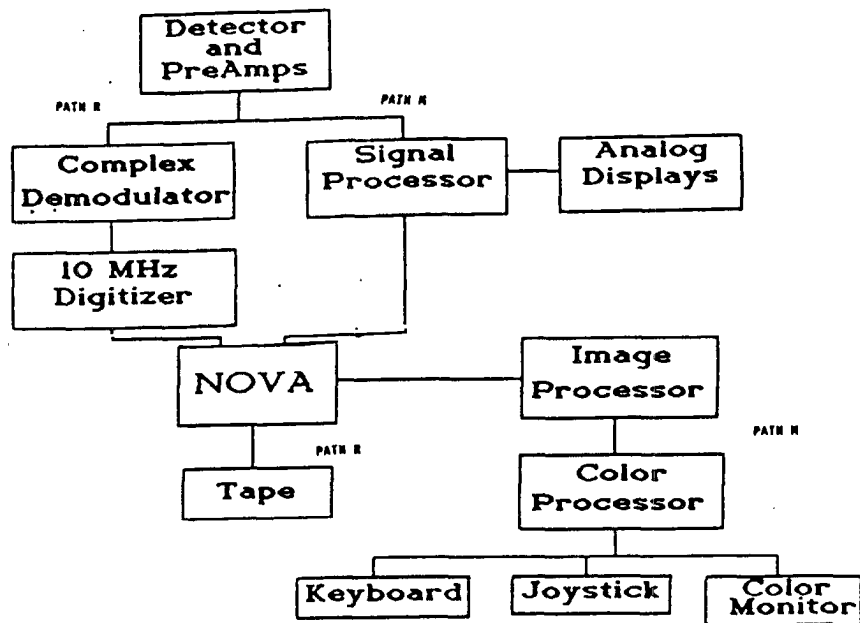


Figure 2.3. Data stream for NOAA Doppler lidar. Path m gives the path for moment data mode processing; path r gives the path for raw data mode processing.

For the raw data mode the received data are sent to the 10-MHz digitizer, which samples complex components I and Q (in-phase and quadrature) and outputs them in coded form for each data point. The data are then recorded on magnetic tape for further processing at the BL site. Table 2.1 gives the characteristics of the system when it is operated in the raw data mode. Post-processing of raw data is done at the BL site using a Data General Eclipse S200 computer. The I and Q components are decoded from the magnetic tape, and radial velocity vectors are calculated using the pulse-pair technique for frequency estimation.

Table 2.1. NOAA Doppler lidar raw data mode specifications

Wavelength	10.6 μm
Per pulse power (P20)	0.10 J
Pulse repetition rate	10 Hz
Pulse duration	3.3 μs
Polarization of transmitted radiation	Circular
Frequency chirp across pulse	200 kHz
Local Oscillator offset	20 MHz
Transmit/receive telescope diameter	0.25 m
Tunability	Grating tunable over several P & R lines
Laser mode	TEM-00 (Gaussian)
Scan capability	Alt-Azimuth
Minimum range	0.5-1.8 km
Maximum range	Greater than 20 km
Data processor	10-MHz digitizer, complex covariance estimator
Samples per record	1024,2048
Records per scan	1-10,000

The pulse-pair frequency technique has been described by a number of authors (e.g., Zrnic, 1979; Miller and Rochwargner, 1972). Our application of the technique allows choice of gate size and multiple pulse averaging. Using the information from the range-weighting function (Fig. 2.2), our 3.3- μs pulse is centered best by using a 500-m gate. By thresholding the pulse-pair, using a scheme based on return intensity, data points with insufficient return are removed before velocity vectors are calculated.

An alternative method to process the data came on line in 1983. A hardware processor was added to the data stream, which does a multiple-lag, multi-pulse pair calculation of the first three moments of the Doppler spectrum (Lee and Lee, 1981). The new processor has switch adjustments to allow choice of settings for lag and number of pulses averaged used for each moment data point. An image processor and color display that use the moment processor data were also added to the system. The display allows both real-time and recorded playback of the zeroth-, first-, and second-moment calculation. Table 2.2 gives the specifications for the signal processor and image processor.

A gate size of 300 m (as opposed to the adjustable raw system) was set for data taken by the moment system during the experiments used in this paper. The

Table 2.2. NOAA Doppler lidar moment processor specifications

Signal Processor	
Range parameters	
Sampling range	200 μ s 30 km at 2 μ s gate width
Delay	0-199 μ s
Gate width	1,2,4,8 μ s
Input bandwidth	15 MHz (\pm 40 ms^{-1})
Integration	1-400 pulses
Pulse rate	0-50 Hz
Output rate	2000 range gates/second
Output parameters	
Poly-pulse pair estimates of	Zeroth moment (amplitude) First moment (velocity) Second moment (spectral width)
# Complex covariance lags	0-8
Real-time analog display	Amplitude vs. range Velocity vs. range Spectral width vs. range
Image Processor and Display	
Microprocessor	IS 68K Q bus system
Processor memory	1.25 MBytes
Pixel format	768 \times 575
Simultaneous displayable colors	64
Displays available	Radial VAD RHI Range vs. time Azimuth vs. elevation Wind speed vs. height Wind direction vs. height Vertical component vs. height

moment processor was set for either two- or three- pulse averaging. The choice of pulses to average was based on the speed necessary to scan the complete area and the number of separate points per degree needed.

3. MEAN WIND COMPARISON

3.1 Introduction

The NOAA Doppler lidar van was located at the Boulder Atmospheric Observatory (BAO) site for the Boulder Upslope Cloud Observation Experiment (BUCOE). The BUCOE experiment was conducted from 4 March through 17 May 1982. One of the goals of the experiment was to calibrate various remote sensors against in situ sensors (Gossard, 1982).

3.2 Tower Site and Data

The lidar trailer was located within the BAO tower fenced enclosure during the BUCOE study, about 50 m from the tower base. Figure 3.1 gives the site plan and instrumentation during the BUCOE experiment.

The BAO is located 5 km to the east of Erie, Colorado. The site is on predominantly agricultural land in a region of gently rolling terrain. The foothills of the Colorado Rockies rise approximately 25 km to the west; the city of Denver is 30 km to the south and the Platte River basin is 16 km to the east of the site (Kaimal and Wolfe, 1978). Figure 3.2 shows the general topography of the site and its geographical location.

The BAO tower is a 300-meter-tall guyed structure of open lattice design (Fig. 3.3) which is instrumented at eight fixed levels. For the BUCOE study the tower instrumentation was configured with the sonic anemometers on the SSE booms and propeller vane anemometers on the NNW booms. Details of the tower and its instrumentation are given in Table 3.1. Kaimal and Gaynor (1983) described the operation of the tower and listed instrument specifications.

The tower wind sensors, sonic anemometers (sonics), and propeller-vane anemometers (prop) are located on booms at each of the tower's eight levels. During the BUCOE experiment the sonics were attached to a boom oriented 26° east of south, and the props were attached to a boom oriented 180° away from the

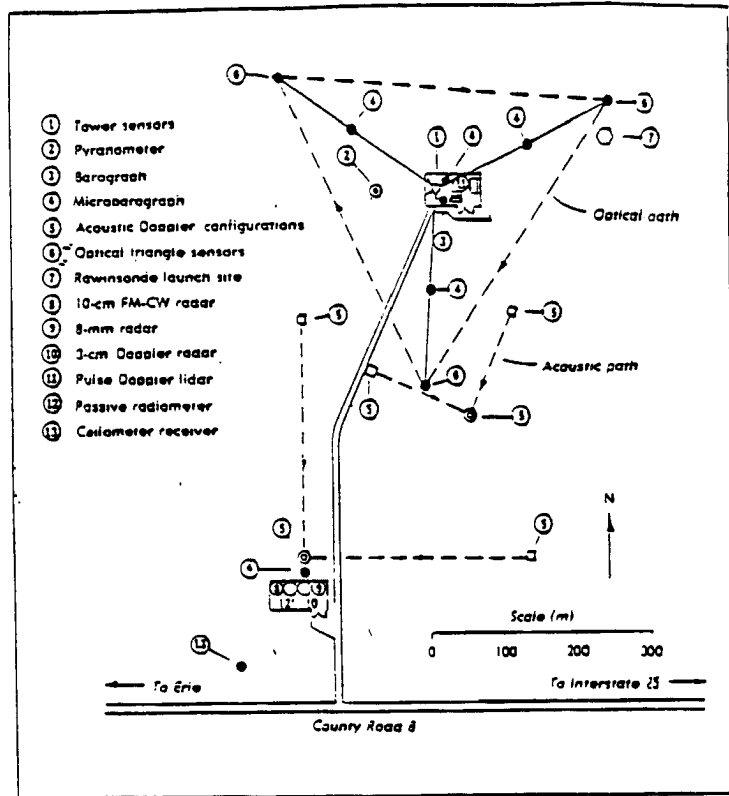


Figure 3.1. Site plan for BUCOE experiment (from Kaimal, 1980).

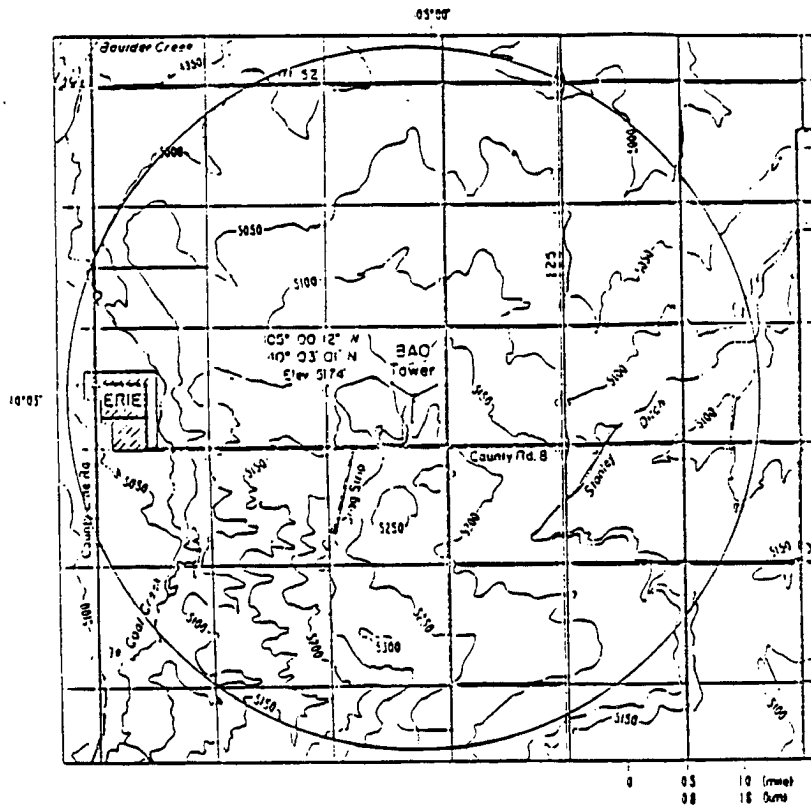


Figure 3.2. Geographical location and general topography of the Boulder Atmospheric Observatory. The circles area represents 5 km from site. (From Kaimal and Wolfe, 1978).

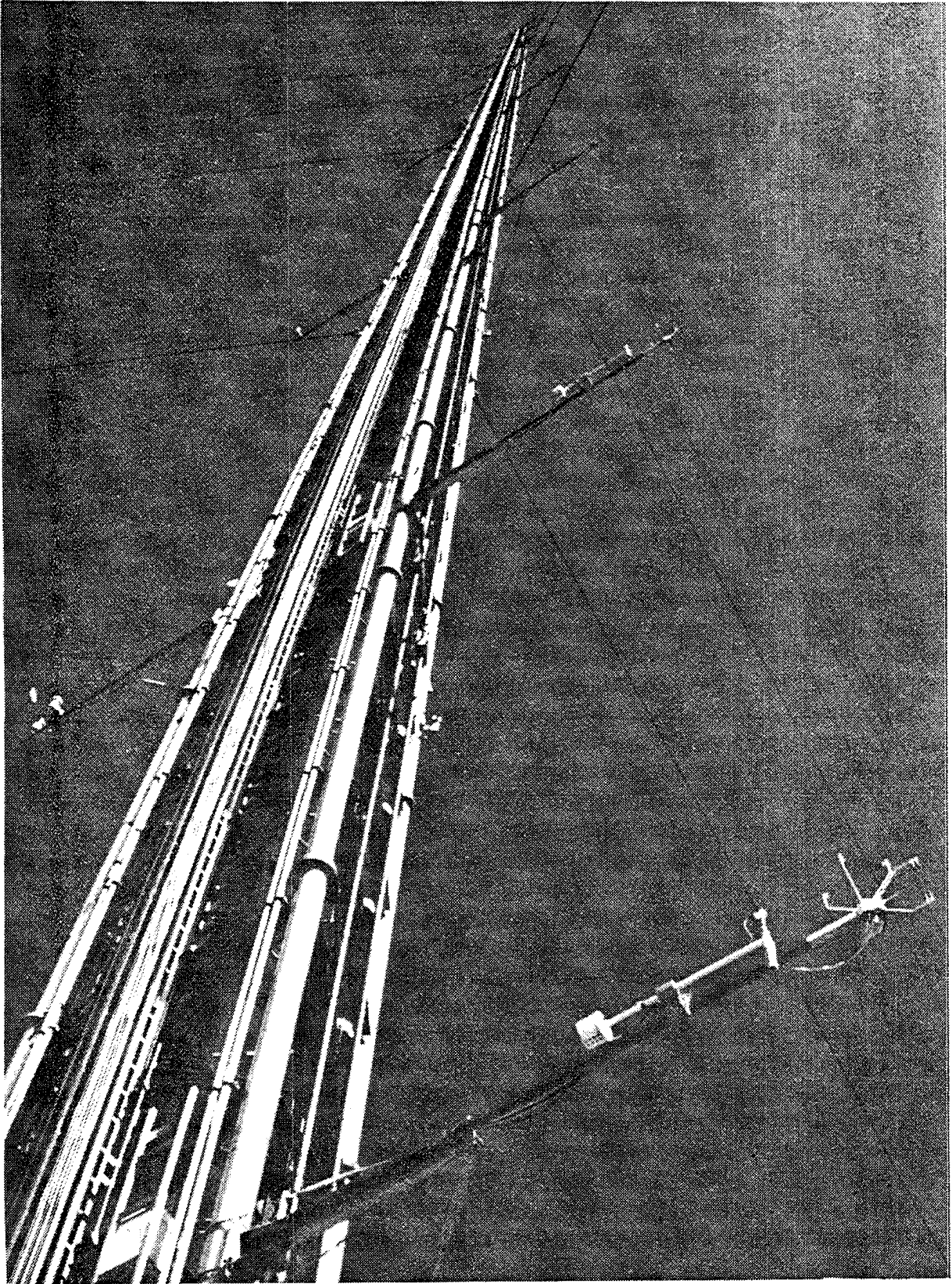


Figure 3.3. BAO Tower (Kaimal and Gaynor, 1983)

Table 3.1. Tower instrumentation*

Sensor	Parameter(s) measured	Response characteristic	Rate at which sampled	Location
Sonic anemometer	u,v,w	0.05-Hz block-average	10 Hz	SE boom (all levels)
Propeller-vane anemometer	S,D	2.4-m distance constant	1 Hz	SE boom (all except 150- and 250-m levels)
Platinum wire thermometer	T	5-10 Hz cut-off	10 Hz	SE boom (all levels)
Quartz thermometer	T	1-min time constant	1 Hz	SE boom (all levels)
Cooled-mirror hygrometer	T _d	1-s cycle time	1 Hz	NW boom (all levels)
Absolute pressure	P		1 Hz	Surface (below van)
Fluctuating pressure	P		1 Hz	Surface (5 locations)
Optical triangle	S,D, Conv, C _n ²	Spatial average over 450-m equilateral triangle	1 Hz	Surface (outer anchor points)
Solar	R	about 5 min	1 Hz	Surface
Acoustic Doppler	u,v			(REC)=receiver (TR)=transmitter
Microwave radiometer	T,q			(1) NEMS (2) SCAMS (3) MTS

* From Hooke, 1979.

sonics. An explanation of how the tower data was processed is given in Appendix A.

The sonic anemometers consist of a set of three single-axis acoustic arrays. Each acoustic array consists of a transmitter and receiver. They are pulsed at 200 Hz, and 20 point block averages are transferred to the site processor for the raw data mode (Eversole, 1978). The time difference between two pulses propagating in opposite directions provides the measure of velocity along the path (Mitsuta, 1971). Three sonic paths (separations across which velocity is measured) are used in the BAO anemometers. One path is set along the boom axis, the second path is offset 90° along the horizontal axis, and the third path is set vertically (Fig. 3.4). This configuration produces velocity components in two horizontal (along and across) and the vertical (w) directions. The 10 s average (BAO 'A') data are transformed from the path components into standard meteorological u and v component form (E-W, N-S) before being recorded on the site computer. Raw data are retained in the original component form.

The propeller-vane anemometers (Fig. 3.5) are standard Gill designs (R.M. Young, Model 35003). The props are sampled for wind speed and direction once every second. Block averages are performed for ten sample points, and the averages, "A" data, are transferred to the site processor.

3.3 Lidar Processing

The lidar scanner for the BUCOE experiment was located on the roof of the trailer about 4.5 m above ground level. The scanner was used to generate velocity-azimuth display (VAD) (Fig. 3.6) scans at various zenith angles. The zenith angle was determined by manually rotating the scanner in the vertical and then lining up the scanner to a premeasured angle mark. A parcel technique, to be explained shortly, was used to compare profiles from the lidar VAD scans with the time series profiles of the tower sensors.

For the purposes of the comparison, a listing of dates and times when the lidar was operating in an 80-degree zenith angle VAD mode during its stay on the BAO site was compiled. This VAD list (Table 3.2) was compared with the tower archived data listing (Table 3.3) for the three months of the BUCOE experiment. Times when both the tower and lidar instruments data were available were investigated for the wind comparison.

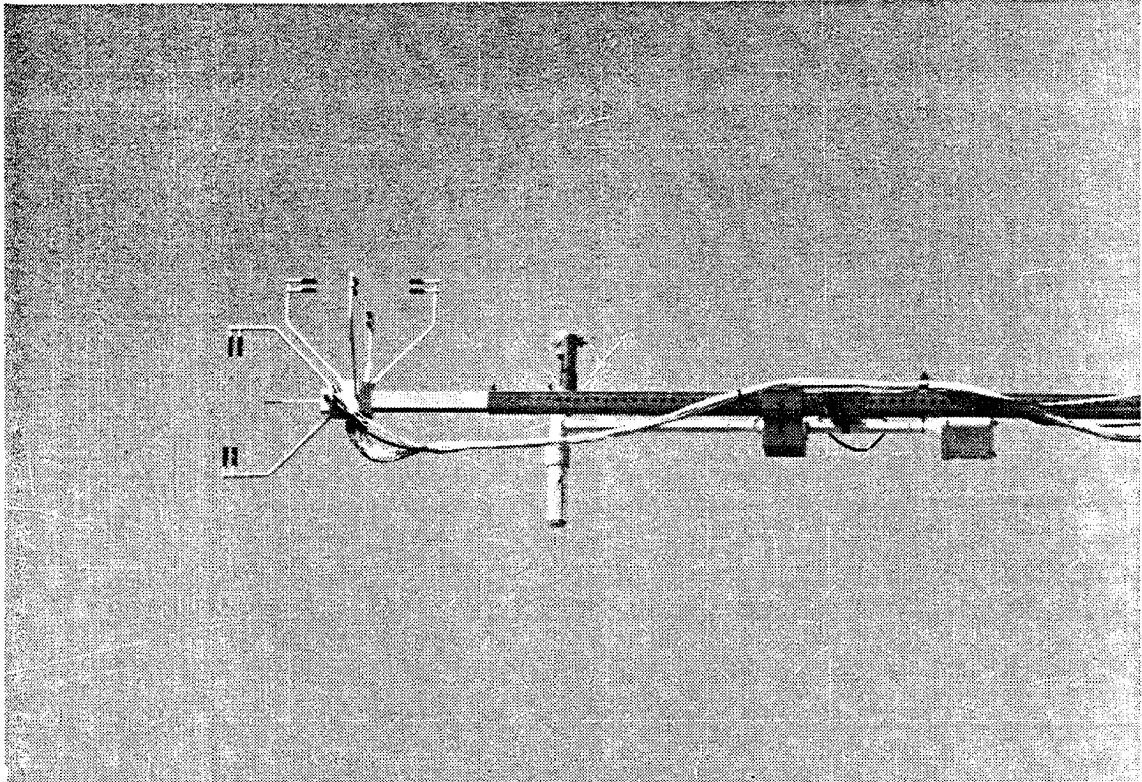


Figure 3.4. View of three-axis sonic anemometer (from Wolfe, 1985).

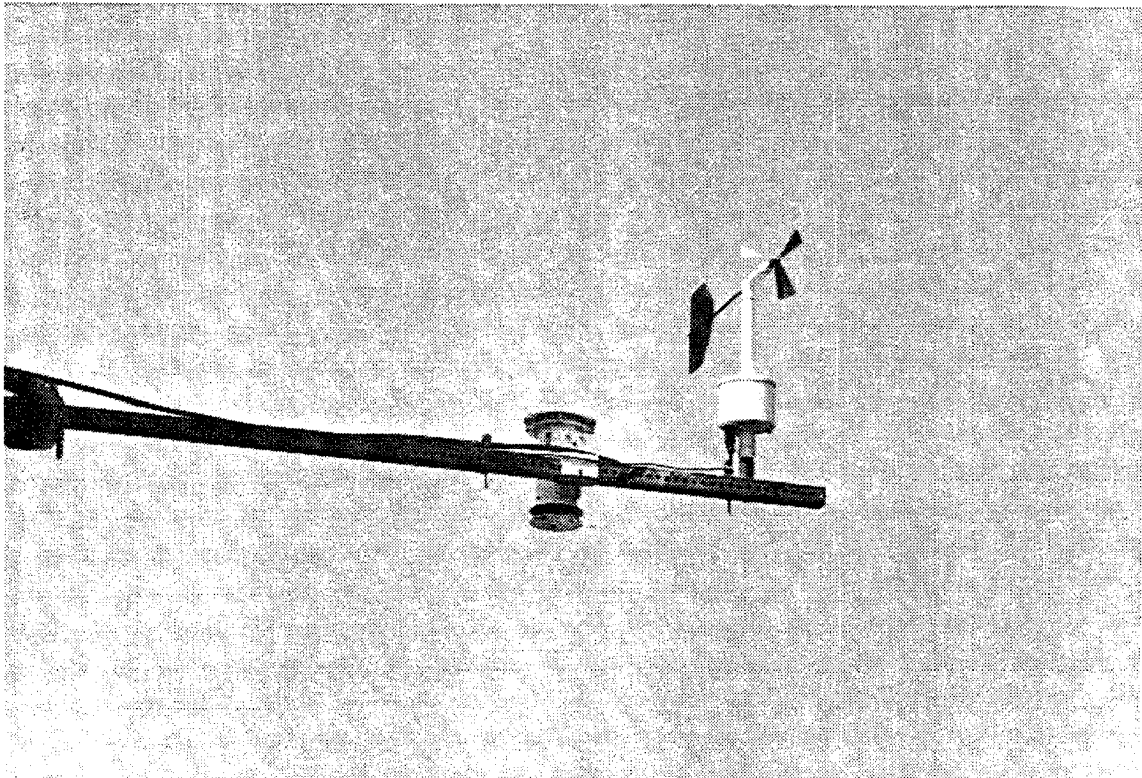


Figure 3.5. View of propeller-vane anemometer (from Wolfe, 1985).

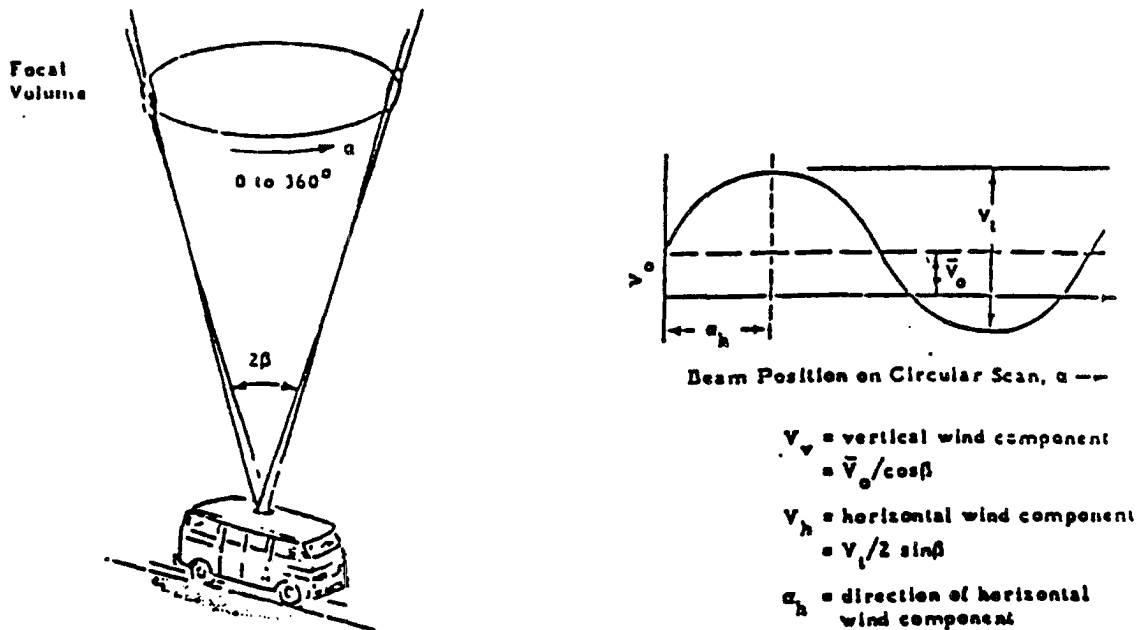


Figure 3.6. VAD technique and sample VAD resultant scan.

Table 3.2. Dates and times of VAD runs at 80-degree zenith angle during BUCOE experiment

Date	Time	Date	Time
04-Mar-82	14:23:59	27-Apr-82	11:39:13
05-Mar-82	12:03:56	27-Apr-82	11:59:22
08-Mar-82	13:59:29	27-Apr-82	13:04:03
09-Mar-82	11:43:31	27-Apr-82	13:07:34
10-Mar-82	15:44:20	29-Apr-82	14:09:07
12-Mar-82	11:01:11	29-Apr-82	15:29:58
15-Mar-82	15:14:58	10-May-82	11:40:16
17-Mar-82	12:05:20	11-May-82	11:03:29
19-Mar-82	10:23:16	11-May-82	11:05:32
24-Mar-82	14:24:22	11-May-82	11:10:03
24-Mar-82	14:27:47	11-May-82	11:48:26
24-Mar-82	15:17:11	11-May-82	12:17:01
24-Mar-82	15:31:01	11-May-82	12:18:49
24-Mar-82	15:33:43	11-May-82	12:23:44
24-Mar-82	16:09:29	11-May-82	12:59:17
24-Mar-82	16:52:20	11-May-82	13:04:46
24-Mar-82	17:07:22	11-May-82	14:16:16
24-Mar-82	17:58:58	11-May-82	14:19:23
31-Mar-82	12:27:39	11-May-82	14:27:01
31-Mar-82	12:35:38	12-May-82	10:30:49
05-Apr-82	15:46:15	12-May-82	11:28:20
20-Apr-82	09:19:36	12-May-82	11:31:46
23-Apr-82	11:18:12	12-May-82	11:36:50
23-Apr-82	11:23:46	12-May-82	11:40:13
27-Apr-82	10:22:17	21-May-82	12:20:35
27-Apr-82	10:24:16	25-May-82	10:44:04
27-Apr-82	10:28:54	25-May-82	10:55:01
27-Apr-82	10:46:42	26-May-82	13:59:13
27-Apr-82	10:50:07		

Table 3.3 BAO archive record for BUCOE - boxed areas represent possible lidar/tower comparisons

Archive data since 820301 of kind A																								
Date	Hour																							
	0	1	2	3	4	5	6	7	8	9	10	11	12	13	14	15	16	17	18	19	20	21	22	23
820301	111	111	111	111	111	111	111	111	110	111	111	111	111	111	101	111	111	111	111	111	111	111	111	111
820302	111	111	111	111	111	111	111	111	111	111	111	111	111	111	111	111	111	111	111	111	111	111	111	111
820303	111	111	111	111	111	111	111	111	111	110	111	111	111	111	110	111	111	111	111	111	111	111	111	111
820304	111	111	111	111	111	111	111	111	111	111	111	111	111	111	111	111	111	111	111	111	111	111	111	111
820305	111	111	111	111	111	111	111	111	111	111	111	111	111	111	111	111	111	111	111	111	111	111	111	111
820306	111	111	111	111	111	111	111	111	111	111	111	111	111	111	111	111	111	111	111	111	111	111	111	111
820307	111	111	111	111	111	111	111	111	111	111	111	111	111	111	111	111	111	111	111	111	111	111	111	111
820308	111	111	111	111	111	111	111	111	111	111	111	111	111	111	111	111	111	111	111	111	111	111	111	111
820309	111	111	111	111	110	100	000	001	110	111	111	111	111	111	111	111	111	111	111	111	111	111	111	111
820310	111	111	111	111	111	111	111	111	111	111	111	111	111	111	111	111	111	111	111	111	111	111	111	111
820311	111	111	111	111	111	111	111	111	111	111	111	111	111	111	111	111	111	111	111	111	111	111	111	111
820312	111	111	111	111	111	111	111	111	111	111	111	111	111	111	111	111	111	111	111	111	111	111	111	111
820313	111	111	111	111	111	111	111	111	111	111	111	111	111	111	111	111	111	111	111	111	111	111	111	111
820314	111	111	111	111	111	111	111	111	111	111	111	111	111	111	111	111	111	111	111	111	111	111	111	111
820315	111	111	111	111	111	111	111	111	110	111	100	000	100	011	111	111	111	111	111	111	111	111	111	111
820316	111	111	111	111	111	111	111	111	111	111	111	111	111	111	111	011	111	111	111	111	111	111	111	111
820317	111	111	000	000	000	000	000	111	100	111	111	111	111	111	111	011	111	111	111	111	111	111	111	111
820318	111	111	111	111	110	000	000	000	001	111	111	111	111	111	111	111	011	111	111	111	111	111	111	111
820319	111	111	111	111	111	111	110	111	110	111	111	111	111	111	111	111	111	111	111	111	111	111	111	111
820320	111	111	111	111	111	111	111	111	111	111	111	111	111	111	111	111	111	111	111	111	111	111	111	111
820321	111	111	111	111	111	111	111	111	111	111	111	111	111	111	111	111	111	111	111	111	111	111	111	111
820322	111	111	111	111	111	111	111	111	111	111	111	111	111	111	111	111	111	111	111	111	111	111	111	111
820323	111	111	110	111	111	111	111	110	111	111	111	111	111	111	101	111	111	111	111	111	111	111	111	111
820324	111	111	111	111	111	111	111	101	110	111	111	111	111	111	111	111	111	111	111	111	111	111	111	111
820325	111	111	111	111	111	111	111	111	111	111	111	111	111	111	111	111	111	111	111	111	111	111	111	111
820326	111	111	111	111	111	111	111	111	111	111	111	111	111	111	111	111	111	111	111	111	111	111	111	111
820327	111	111	111	111	111	111	111	111	111	111	111	111	111	111	111	111	111	111	111	111	111	111	111	111
820328	111	111	111	111	111	111	111	110	111	111	111	111	111	111	111	111	111	111	111	111	111	111	111	111
820329	111	111	111	111	111	111	111	111	101	111	111	111	111	111	111	111	111	111	111	111	111	111	111	111
820330	111	111	111	111	111	111	111	111	111	111	111	111	111	110	111	011	111	111	111	111	111	111	111	111
820331	111	111	111	111	111	111	111	111	111	111	111	111	111	111	111	100	111	111	000	11	111	111	111	111
820401	111	111	111	111	111	111	111	111	011	111	111	111	111	111	111	111	111	111	111	111	111	111	111	111
820402	111	111	111	111	111	111	111	111	111	111	110	001	111	111	111	111	111	111	111	111	111	111	111	111
820403	111	111	111	111	111	111	111	111	111	111	111	111	111	111	111	111	111	111	111	111	111	111	111	111
820404	111	111	111	111	111	111	111	111	111	111	111	111	111	111	111	111	111	111	111	111	111	111	111	111
820405	111	111	111	111	111	111	111	111	101	111	111	111	111	111	110	111	111	111	111	111	111	111	111	111
820406	111	111	111	111	111	111	101	111	111	111	111	111	111	111	011	111	111	111	111	111	111	111	111	111
820407	111	111	111	111	111	111	111	111	111	111	111	111	100	111	110	111	111	111	111	111	111	111	111	111
820408	111	111	111	111	111	111	111	111	111	011	111	111	111	111	111	011	111	111	111	111	111	111	111	111
820409	111	111	111	111	111	111	111	111	111	011	111	111	111	111	111	111	111	111	111	111	111	111	111	111
820410	111	111	111	111	111	111	111	111	111	111	111	111	111	111	111	111	111	111	111	111	111	110	000	111

3.3.1 Mean wind calculation

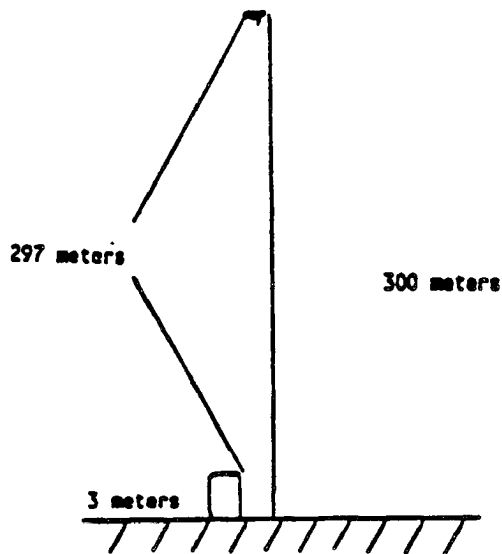
The lidar calculation of the mean wind for the comparison required processing the lidar data at the edge of the first usable range. The data were taken at an 80° zenith angle, which indicates that the desired starting range for meters in height is 1.46 km along the radial (Fig. 3.7). Because of instrumental considerations, the NOAA lidar system minimum range is approximately 1 km along the radial. An added minimum range consideration was introduced to the lidar data collected during BUCOE due to the large number of aerosols near the ground. This amplified the effect of the low-energy, high-chirp tail and caused receiver saturation and an effective extension of the minimum range. It was necessary to implement a technique to determine the first range unaffected by the combination of the receiver saturation and instrument minimum range.

Saturation of the receiver gives a false indication of a high wind return. To determine ranges subject to the saturation effect, the data were processed starting initially at 1.25 km along the radial and stepping by 0.015 km (Fig. 3.8) until at least 16 gates were processed. The mean winds from each run were recorded and plotted against height (and range). The winds recorded typically went from a very high value in the affected area to a relatively consistent wind speed with increasing height (Fig. 3.9). The wind corresponding to the best level beyond the interference but closest to the 300 m height was used in the comparison.

3.3.2 Parcel processing

A representative parcel was defined as the time sequence of tower winds that would, when extended using Taylor's hypothesis, represent the winds recorded by the lidar. The steps necessary to create each appropriate parcel were (1) identify a parcel from the VAD scan and (2) identify the corresponding tower time series.

Identifying the VAD parcel requires taking the geometry of the scan and calculating the horizontal extent of the area circumscribed by the scan. For the BUCOE runs used in the tower comparison, the angle with the zenith was 80° . The radius used by the lidar was targeted to be 300 m divided by the cosine of 80° since the 300-m winds of the tower were being used in the comparison.

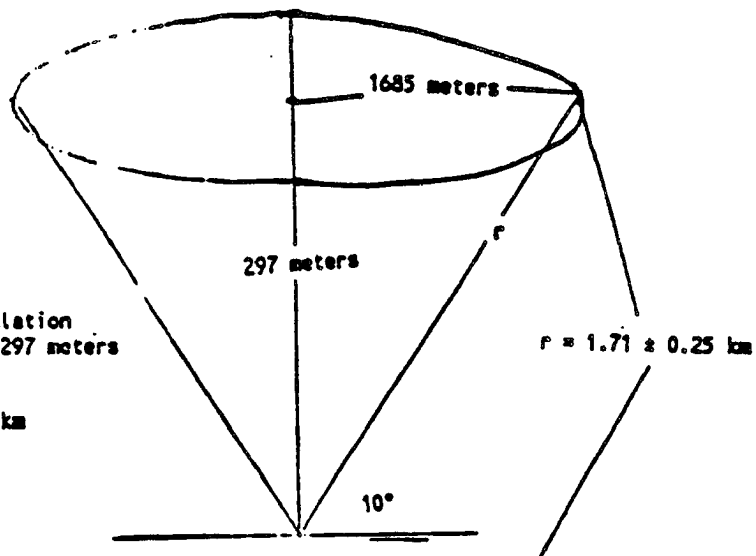


horizontal range (x) calculation

$$\tan 10^\circ = 297/x$$

$$x = 297/\tan 10^\circ$$

$$x = 1685 \text{ meters}$$



radial (r) calculation

r - centered at 297 meters

$$\sin 10^\circ = 297/r$$

$$r = 297/\sin 10^\circ$$

$$r = 1.71 \pm 0.25 \text{ km}$$

$$\text{start} = 1.46 \text{ km}$$

$$\text{end} = 1.96 \text{ km}$$

Figure 3.7. Geometry of 80 degree zenith angle scan as used in the lidar/tower comparison.

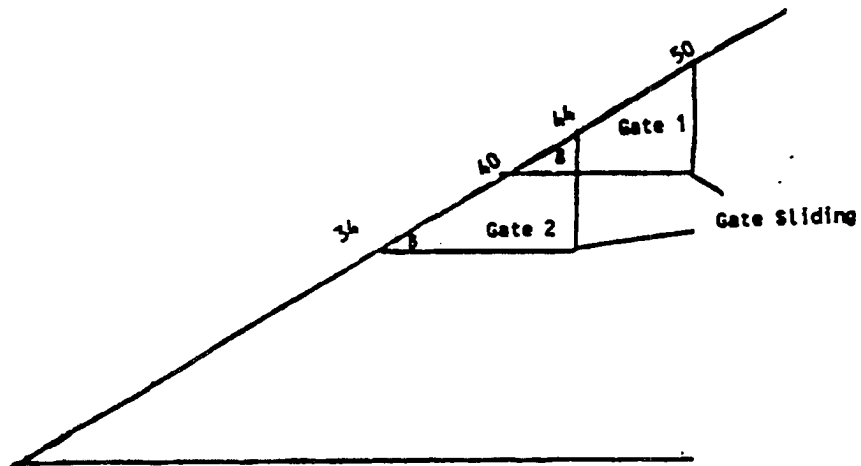
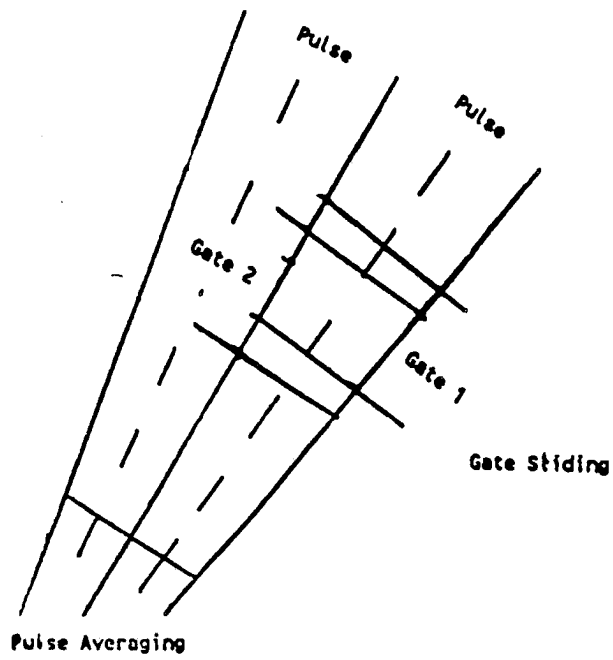
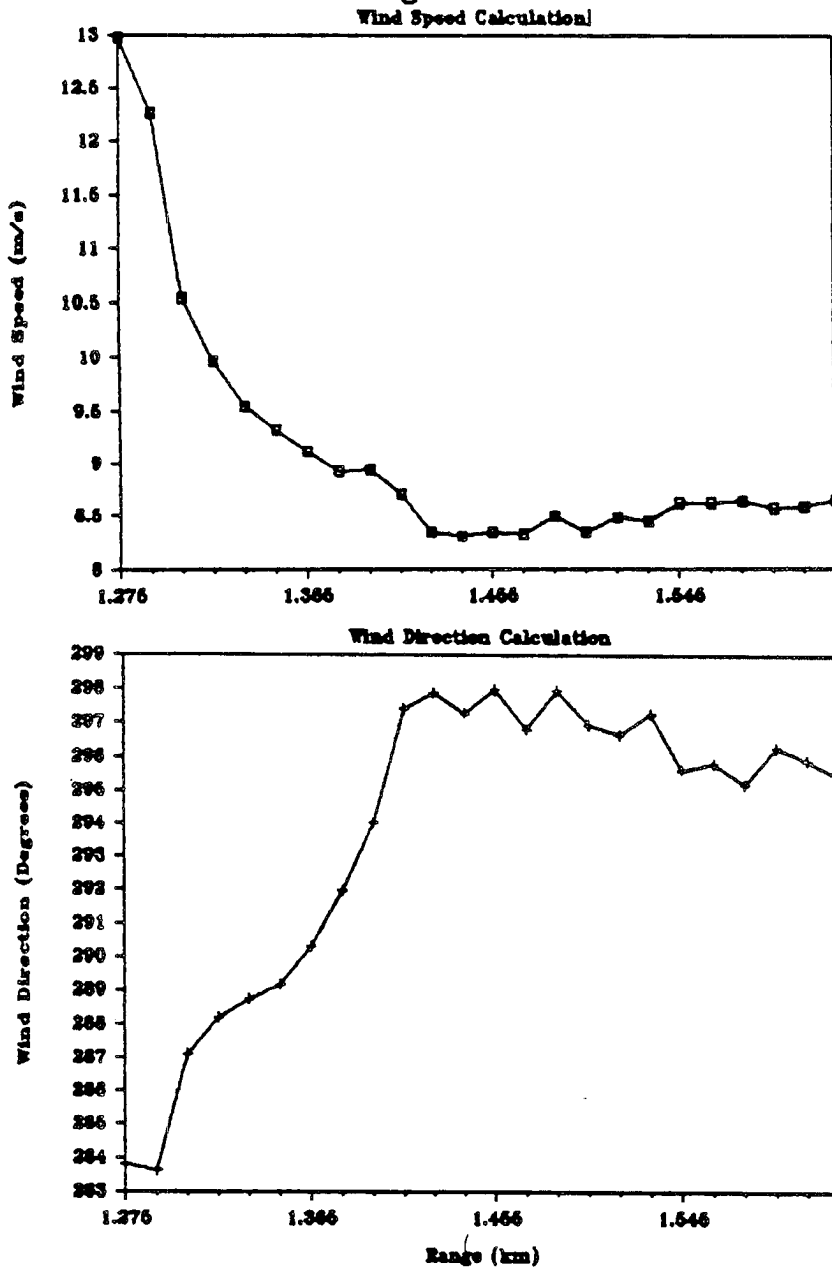


Figure 3.8. Schematic of gate sliding technique as used in the lidar/tower comparison.

Gate Sliding Wind Calculation



The time sequence of tower winds for comparison with the VAD run was calculated using the sonics mean winds at 300 m. The center of the time interval, "t_c", was chosen to match the time of the VAD run. Total time "t_T" was calculated using Taylor's hypothesis, with time equaling VAD circle diameter divided by the sonics mean wind. A time interval "t" was calculated with "t = x/s", "x" being the lidar VAD circle radius and "s" the first-guess speed mean sonics wind. Total time using this notation can be represented as

$$t_T = t_c + 2 t .$$

Beginning time was calculated by

$$t_b = t_c - t .$$

Initially the nearest 20-m mean winds were used to calculate the total time a parcel of air would take to traverse the circle represented by the VAD scan. The procedure was then iterated using neighboring 10-s sonics measurements until the time period and speed matched the parcel as closely as possible. Figure 3.10 gives a schematic of the time line and radius calculation.

The limitations of this method of comparing the time sequence to the VAD area calculation include the assumptions inherent in Taylor's hypothesis and the actual time difference in the air parcels for the two measuring devices. Taylor's hypothesis is valid only for small variations relative to the mean wind (Tennekes and Lumley, 1972). Especially for the cases with low winds and the cases with large wind variance, the hypothesis is not strictly valid, and the lidar and BAO winds should agree more poorly. The differences in the times of the measurement should not present problems for time periods that are (1) greater than the scale of a single thermal passing the tower, (2) time periods less than the scale of changes in the air masses during the measurement and (3) times unaffected by diurnal variations.

One additional assumption is made in the comparison analysis. It is assumed that conditions at the 300-m height of the tower are representative of those at the calculated radius of the VAD (Panofsky and Townsend, 1964). Figure 3.11 gives the close-in topography of the BAO tower site. When the VAD circle is

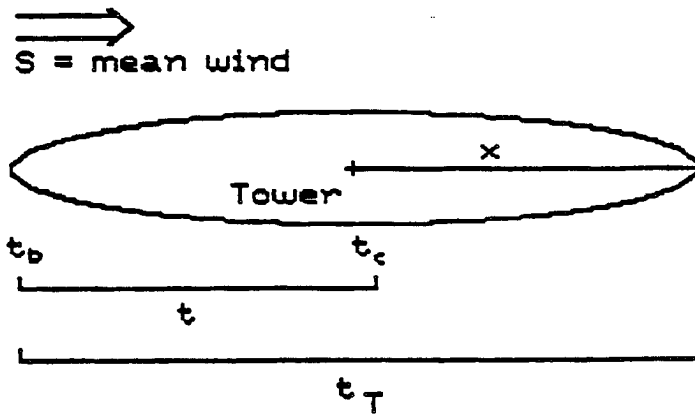


Figure 3.10. Taylor's hypothesis as applied to a tower time series and a VAD run space series.

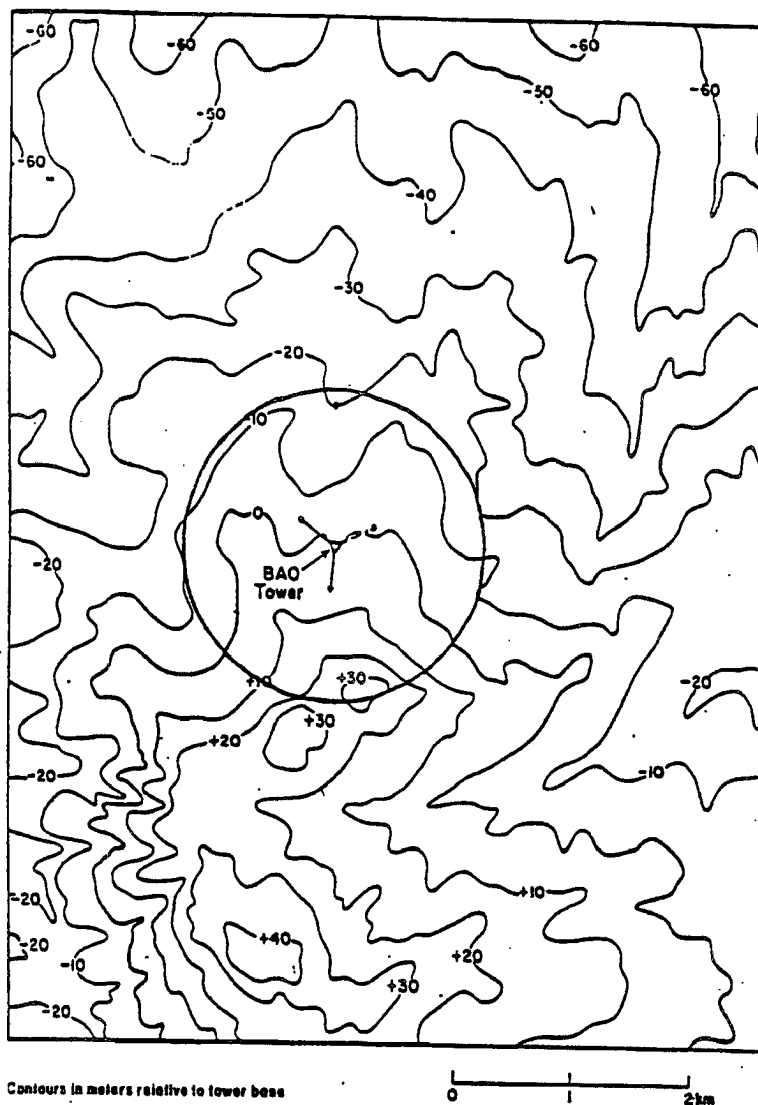


Figure 3.11. Contour plot of terrain around BAO tower. Contours are in meters relative to tower base, circle represents the approximate lidar VAD radial region used in the comparison.

traced on the topography, a change of 50-m in height above ground from one side of the circle to the other is indicated. Although this 50-m represents one-sixth of the height of the comparison level, it is initially assumed that this variation does not affect the mean wind at 300-m altitude in the experimental area.

3.4 Comparison Results

3.4.1 Data set

Table 3.4 lists the dates and times of the lidar runs and the corresponding tower times. The last column gives the spatial extension (average velocity multiplied by time) of the tower times. Since tower winds are available only every 10-s, some discrepancy in the spatial extension for the area was expected. The weather conditions during the period of the comparison varied from clear and nearly calm to driving snow. Table 3.5 gives general conditions during the times of the comparisons. Appendix D gives information on stability during the 20-m periods surrounding the comparison times. Additional data from other instruments on the site were used to help identify weather conditions, as well as information from logs of the experiments being conducted.

Certain cases were deleted from the comparison set because of instrumental problems or weather conditions. Two periods were eliminated because of insufficient lidar return from the region in the study, 2 periods were eliminated because of tower data inconsistencies, 20 periods occurred during tower down time, and 2 periods were deleted during a frontal passage at the tower that made the parcel method unacceptable. Seven periods were included in the propeller-vane data comparison but not in the sonic anemometer data comparison because of contamination. Table 3-6 gives the average wind speed and direction obtained by the tower prop and sonics and the lidar VAD for the periods used in the comparison. Figures 3.12 and 3.13 give the results of the comparison.

The wind speed analysis gave standard errors (Table 3.7) between the sonics sensor and the lidar VAD technique of less than 0.5 m/s. The lidar/prop comparison had a slightly higher standard error, 0.6 m/s, but the data set was slightly different from the lidar/sonics comparison data set as it included cases with higher wind speeds where the sonics sensor was no longer usable. The

Table 3.4. Summary of VAD and tower run times used
in lidar/tower wind comparison

Date	VAD begin time (MDT)	Tower begin time (MST)	VAD range (meters)	Tower total time (MDT)
04-Mar-82	14:23:59	14:19:40	1425	00:08:30
05-Mar-82	12:03:56	11:55:50	1620	00:08:00
08-Mar-82	13:59:29	13:53:10	1440	00:12:40
09-Mar-82	11:43:31	11:41:30	1425	00:03:50
10-Mar-82	15:44:20	15:39:50	1455	00:09:20
12-Mar-82	11:01:11	10:59:10	1425	00:03:30
15-Mar-82	15:14:58	15:12:10	1425	00:06:00
17-Mar-82	12:05:20	11:47:00	1500	00:36:40
19-Mar-82	10:23:16	10:21:30	1440	00:03:10
24-Mar-82	14:24:22	14:19:20	1590	00:09:50
24-Mar-82	14:27:47	14:25:00	1470	00:05:30
24-Mar-82	15:17:11	15:15:50	1455	00:02:30
24-Mar-82	15:31:01	15:29:40	1455	00:02:30
24-Mar-82	15:33:43	15:32:20	1455	00:02:30
24-Mar-82	16:09:29	16:08:00	1455	00:03:00
24-Mar-82	16:52:20	16:50:20	1545	00:04:00
24-Mar-82	17:07:22	17:04:50	1545	00:05:00
24-Mar-82	17:58:58	17:56:20	1620	00:05:30
31-Mar-82	12:27:39	12:19:20	1635	00:16:40
31-Mar-82	12:35:38	12:25:50	1620	00:19:20
05-Apr-82	15:46:15	15:41:40	1605	00:09:00
20-Apr-82	09:19:36	09:16:00	1620	00:07:50
23-Apr-82	11:18:12	11:10:00	1455	00:16:10
23-Apr-82	11:23:46	11:16:20	1455	00:15:00
27-Apr-82	11:39:13	10:27:50	1560	00:22:20
27-Apr-82	11:59:22	10:51:20	1455	00:22:20
29-Apr-82	14:09:07	13:03:40	1515	00:05:50
29-Apr-82	15:29:58	14:25:50	1455	00:04:30
10-May-82	11:40:16	10:31:40	1605	00:17:30
12-May-82	10:30:49	09:21:00	1620	00:19:50
12-May-82	11:28:20	10:19:40	1590	00:18:20
12-May-82	11:31:46	10:21:50	1590	00:20:00
12-May-82	11:36:50	10:26:50	1590	00:20:00
12-May-82	11:40:13	10:30:10	1590	00:20:00
21-May-82	12:20:35	11:12:10	1485	00:17:20
25-May-82	10:44:04	09:39:30	1500	00:07:10
25-May-82	10:55:01	09:51:20	1620	00:07:20
26-May-82	13:59:13	12:50:00	1620	00:16:30

Table 3.5. Weather conditions during lidar/tower comparison

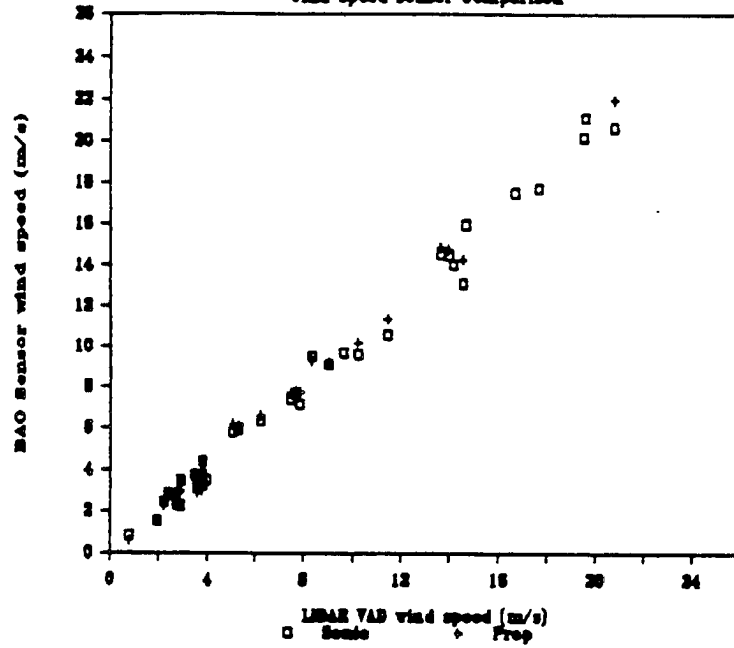
	MDT	General conditions	Solar radiation information
04-Mar-82	1400-1500	Hail and snow	Clouds covering area
05-Mar-82	1100-1400	Snow flurries	Clouds moving through area, clearing around 1400
08-Mar-82	1200-1400		Cloudy
09-Mar-82	1000-1300		Clearing in afternoon
10-Mar-82	1400-1600	Cloudy	Interspersed cloudiness
12-Mar-82	1000-1200		Clear
15-Mar-82	1400-1600		Obscured
17-Mar-82	1100-1300		Partly cloudy with clear areas
19-Mar-82	0900-1200		Clear
24-Mar-82	1200-1900	Frontal passage 1430, light to heavy precip	Afternoon cloudiness
31-Mar-82	1100-1400		Afternoon cloudiness
05-Apr-82	1400-1700		Morning cloudy with clearing in afternoon
19-Apr-82	1300-1500	Snow and graupel	
20-Apr-82	0800-1000		Cloudy
23-Apr-82	1000-1300		Clear until late afternoon
27-Apr-82	0900-1400	Extensive low clouds and fog	Cloudy
29-Apr-82	1300-1600	Light rain, frontal passage 1430	Cloudy
10-May-82	1100-1300	Upper level clouds	Some clearing in late morning, afternoon cloudy
11-May-82	1000-1500		
12-May-82	0900-1300	Light rain	Cloudy
21-May-82	1100-1300		Clear
25-May-82	0900-1200		Clear in morning, cloudy in afternoon
26-May-82	1200-1500		Clearing after noon

Table 3.6. Wind speed and direction summary for lidar/tower wind comparison

Date	VAD run time (MDT)	Prop speed (m/s)	Prop direction (degrees)	Sonic speed (m/s)	Sonic direction (degrees)	Lidar speed (m/s)	Lidar direction (degrees)
04-Mar-82	14:23:59	6.35	90.75	6.58	92.75	6.21	72.34
05-Mar-82	12:03:56	0.85	185.55	0.59	185.23	0.80	191.34
08-Mar-82	13:59:29	4.39	120.89	4.42	119.79	3.79	87.73
09-Mar-82	11:43:31	14.54	280.92	14.79	271.54	14.00	255.11
10-Mar-82	15:44:20	5.17	313.48	6.09	319.82	5.32	293.41
12-Mar-82	11:01:11	16.00	255.92			14.69	227.78
15-Mar-82	15:14:58	9.51	316.61	9.29	312.78	8.34	297.42
17-Mar-82	12:05:20	1.52	105.53	1.53	100.14	1.93	79.98
19-Mar-82	10:23:16	17.76	276.91			17.69	246.33
24-Mar-82	14:24:22	6.03	322.34			9.63	299.82
24-Mar-82	14:27:47	10.57	0.34			14.16	339.87
24-Mar-82	15:17:11	21.12	20.80	22.96	25.37	19.61	359.21
24-Mar-82	15:31:01	20.68	26.10	21.96	28.80	20.82	5.13
24-Mar-82	15:33:43	20.21	30.77	22.14	36.36	19.52	4.68
24-Mar-82	16:09:29	17.55	31.61	19.14	36.61	16.69	7.93
24-Mar-82	16:52:20	13.17	28.28	14.31	33.12	14.56	11.62
24-Mar-82	17:07:22	10.53	28.60	11.36	33.15	11.45	13.09
24-Mar-82	17:58:58	9.57	38.58	10.19	44.43	10.23	16.69
31-Mar-82	12:27:39	3.69	168.03	3.44	166.11	3.66	142.78
31-Mar-82	12:35:38	3.37	165.88	2.89	164.64	3.57	154.64
05-Apr-82	15:46:15	5.83	20.82	6.18	22.04	5.06	348.09
20-Apr-82	09:19:36	7.13	14.23	7.71	15.12	7.85	343.42
23-Apr-82	11:18:12	3.45	59.69	3.47	63.45	2.93	34.07
23-Apr-82	11:23:46	3.71	63.91	3.80	67.61	3.48	32.64
27-Apr-82	11:39:13	2.46	37.16	2.23	40.15	2.21	357.09
27-Apr-82	11:59:22	2.77	23.41	2.59	27.04	2.61	4.69
29-Apr-82	14:09:07	9.09	37.16	9.21	42.96	9.03	18.34
29-Apr-82	15:29:58	14.56	44.79	14.92	49.70	13.66	25.76
10-May-82	11:40:16	3.50	160.67	3.26	157.56	3.99	140.44
12-May-82	10:30:49	2.84	12.26	2.84	12.07	2.37	330.61
12-May-82	11:28:20	2.24	359.68	2.98	353.58	2.89	312.13
12-May-82	11:31:46	2.24	359.73	2.84	354.64	2.87	318.74
12-May-82	11:36:50	2.35	358.58	2.88	354.69	2.73	327.37
12-May-82	11:40:13	2.33	358.38	2.90	354.09	2.80	327.35
21-May-82	12:20:35	3.25	56.30	3.22	59.65	3.56	41.77
25-May-82	10:44:04	7.65	30.86	7.73	35.23	7.67	7.04
25-May-82	10:55:01	7.37	38.68	7.70	44.57	7.48	16.20
26-May-82	13:59:13	3.73	150.12	3.02	146.81	3.79	119.75

LIDAR/BAO Comparison

Wind Speed Sensor Comparison



LIDAR/BAO Comparison

Wind Direction Comparison

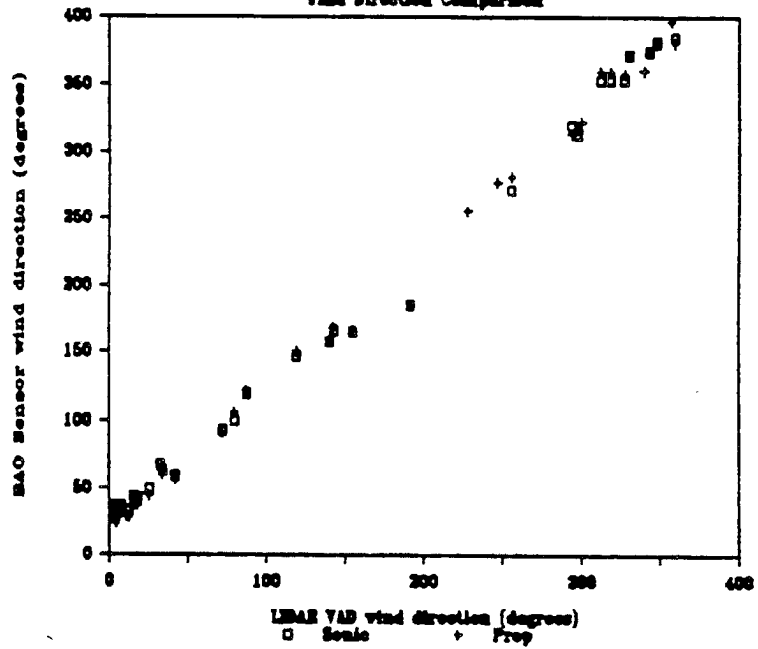
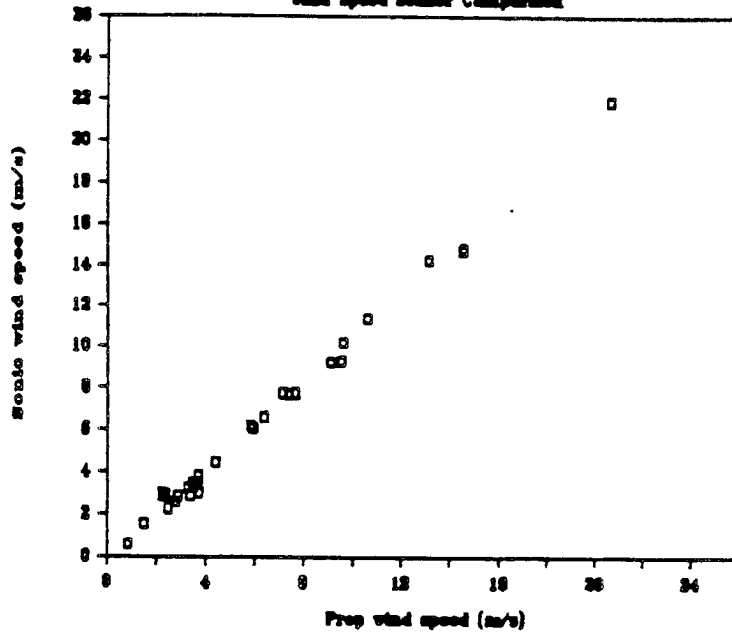


Figure 3.12. Lidar/tower wind sensor comparison
a) Upper plot - wind speed; b) lower plot - wind direction.

BAO PROP/SONIC Comparison

Wind Speed Sensor Comparison



BAO PROP/SONIC Comparison

Wind Direction Comparison

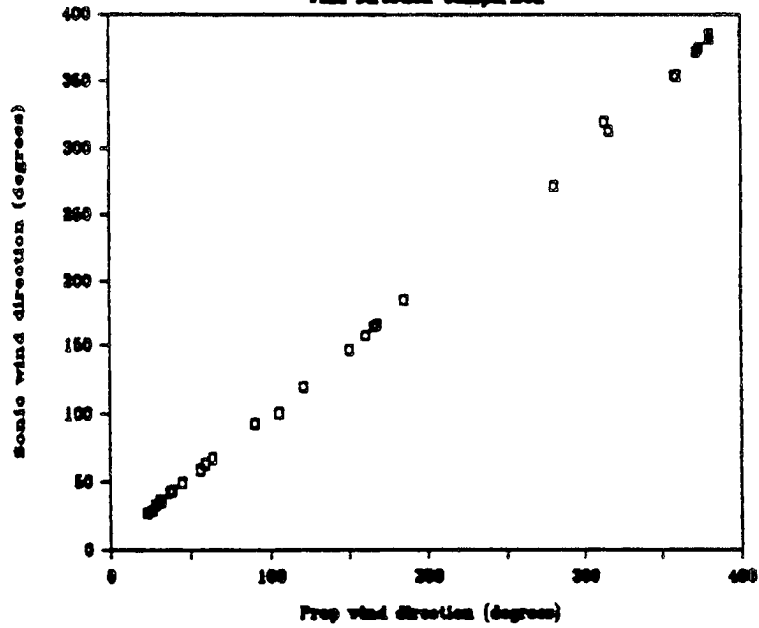


Figure 3.13. Tower sonic/prop sensor comparison
a) Upper plot - wind speed; b) Lower plot - wind direction.

Table 3.7. Wind speed error calculation for lidar/tower comparison

Regression output	Lidar vs. BAO sensors		
Constant		-0.12	
Std. err. of Y est.		0.56	
R squared		0.99	
No. of observations		69	
Degrees of freedom		67	
X coefficient(s)		1.02	
Std. err. of coef.		0.01	
	Lidar vs. prop	Lidar vs. sonics	Sonics vs. prop
Constant	-0.15	-0.14	0.16
Std. err. of Y est.	0.62	0.49	0.36
R squared	0.99	0.99	0.99
No. of observations	38	31	31
Degrees of freedom	36	29	29
X coefficient(s)	1.03	1.05	0.94
Std. err. of coef.	0.02	0.02	0.01

regression coefficient (r^2) for both sets of speed comparisons was greater than 0.99.

The wind direction comparison (adjusted for offset) demonstrated standard errors (Table 3.8) of less than 8° between the tower and VAD analysis methods. The prop sensor gave a slightly better comparison against the VAD analysis than the sonics, with a 4° offset between the two tower sensors.

3.4.2 Wind speed comparison

By resorting the data by wind speed (Table 3.9) insight into processes causing the differences could be investigated. Table 3.10 gives the wind speed standard error calculations for the three speed categories for lidar/sonics, lidar/prop, and sonics/prop comparisons. One additional category for tower sensors is the shadowed region on the tower (Hooke, 1978).

Table 3.8. Wind direction error calculation for lidar/tower comparison

Regression output	Lidar vs. all cases		
Constant		22.31	
Std. err. of Y est.		7.17	
R squared		1.00	
No. of observations		70	
Degrees of freedom		68	
X coefficient(s)		1.03	
Std. err. of coef.		0.01	
	Lidar vs. sonics	Lidar vs. prop	Sonics vs. prop
Constant	23.90	20.74	-4.05
Std. err. of Y est.	7.36	7.06	3.13
R squared	1.00	1.00	1.00
No. of observations	33	37	34
Degrees of freedom	31	35	32
X coefficient(s)	1.02	1.03	1.03
Std. err. of coef.	0.01	0.01	0.00

Table 3.9. Wind speed data sorted by magnitude

	Sonics speed (m/s)	Prop speed (m/s)	Lidar speed (m/s)
Low	0.59	0.85	0.80
	1.53	1.52	1.93
	2.23	2.46	2.21
	2.59	2.77	2.61
	2.84	2.24	2.87
	2.84	2.84	2.37
	2.88	2.35	2.73
	2.89	3.37	3.57
	2.90	2.33	2.80
	2.98	2.24	2.89
Medium	3.02	3.73	3.79
	3.22	3.25	3.56
	3.26	3.50	3.99
	3.44	3.69	3.66
	3.47	3.45	2.93
	3.80	3.71	3.48
	4.42	4.39	3.79
	6.09	5.17	5.32
	6.18	5.83	5.06
	6.58	6.35	6.21
	7.70	7.37	7.48
	7.71	7.13	7.85
	7.73	7.65	7.67
	9.21	9.09	9.03
9.29	9.51	8.34	
	6.03	9.63	
High	10.19	9.57	10.23
	11.36	10.53	11.45
		10.57	14.16
	14.31	13.17	14.56
		16.00	14.69
	14.79	14.54	14.00
	14.92	14.56	13.66
		17.76	17.69
	19.14	17.55	16.69
	21.96	20.68	20.82
	22.14	20.21	19.52
22.96	21.12	19.61	

Table 3.10. Wind speed error calculation for lidar/tower comparison sorted by wind speed category

Regression output	Lidar vs. sonics	Lidar vs. prop	Sonics vs. prop
<u>0-3 m/s</u>			
Constant	-0.49	0.24	0.50
Std. err. of Y est.	0.25	0.47	0.41
R squared	0.09	0.62	0.69
No. of observations	10	10	10
Degrees of freedom	8	8	8
X coefficient(s)	1.23	0.86	0.74
Std. err. of coef.	0.13	0.24	0.18
<u>3-10 m/s</u>			
Constant	-0.47	0.01	0.35
Std. err. of Y est.	0.58	0.50	0.28
R squared	0.94	0.96	0.98
No. of observations	15	16	15
Degrees of freedom	13	14	13
X coefficient(s)	1.11	1.02	0.93
Std. err. of coef.	0.08	0.06	0.03
<u>>10 ms</u>			
Constant	-1.05	-1.60	-0.04
Std. err. of Y est.	0.61	0.85	0.40
R squared	0.98	0.95	0.99
No. of observations	6	12	6
Degrees of freedom	4	10	4
X coefficient(s)	1.11	1.12	0.95
Std. err. of coef.	0.07	0.08	0.04

The low wind speed cases were investigated first. A number of computational differences exist between this and the remaining two categories. The low speed computation requires a longer averaging time for the BAO winds, and therefore a larger difference between the start and stop times for the temporal average and the VAD run time. For the low speed category this time reached into the mesoscale time scale, making the parcel method of processing less useful. The second important problem for the low wind speed category lies in the magnitude of the fluctuating versus the mean wind component of the wind. This problem impacts both the sonics/prop comparison and the VAD/tower sensor comparisons. Taylor's hypothesis requires the fluctuating component to be much

less than the magnitude of the mean wind. Since in the low wind speed cases the two components are of the same order of magnitude, this assumption is violated. An additional problem is introduced by the differing averaging techniques represented by the three methods of wind measurement. The sensitivity of the data to the differing techniques is greater in the low wind speed cases than in any other category. Taking into consideration these problems, it was expected that the low wind speed cases would have a higher error in measurement. The offset for the low wind speed cases was approximately the same for the comparison between the sonics and both the VAD and prop cases. Since the averaging technique for the sonics is designed to highlight the fluctuating components of the wind the sonics were expected to have the largest errors. The lidar/sonics comparison had an r^2 of 0.09 and a standard error of 0.25 m/s, indicating relatively poor agreement. The lidar/prop agreement was more consistent overall; there were some systematic problems due to shadowing differences, with an r^2 of 0.62, a standard error of 0.5, and a constant of 0.2 m/s. The sonics/prop comparison was affected by both shadowing regions; the overall r^2 was equal to 0.69 only slightly better than the lidar/prop comparison. The constant was also high, 0.5 m/s.

The medium (3-10 m/s) wind speed category had better agreement between lidar and tower. The tower sensors also intercompared much better than in the low wind speed cases. The r^2 for the two tower sensors increased to 0.98, with an offset of 0.25 and a lower standard error of 0.28. The lidar/sonics comparison had a standard error of 0.58, higher than in the low wind cases, with an r^2 of 0.94 and an offset approximately the same as for the low wind case. The lidar/prop comparison had no appreciable offset, a standard error of 0.5 m/s, and an r^2 of 0.96. The factors causing the difference in the medium wind cases differ from those affecting the low wind cases. An increase in the standard error was expected because of the increase in wind speeds. The increase in r^2 indicated the fit for the medium wind cases was very good.

The highest wind speed category was more difficult to analyze both because of data inconsistencies in the sonics data, and the small number of cases overall. The tower intercomparison gave excellent agreement for the six cases where data were available for both of the sensors, with an r^2 of 0.99, a small offset, and a standard error of 0.4 m/s. Since half of the cases had obvious sonics data problems requiring their exclusion from the comparisons, the

remaining data were expected to be of higher quality than those for the overall tower intercomparison. The offset for both lidar/tower intercomparisons were higher than expected, 1.60 m/s for the 12 prop cases and 1.05 m/s for the 6 sonics cases, with the tower consistently reporting a lower wind speed. This could be due to terrain differences over the area, the VAD area influencing the overall wind, or possible tower interference with the wind. The standard errors in the comparisons were low: 0.85 m/s for the prop comparison and 0.61 m/s for the sonics cases. The r^2 values were high for both comparisons: lidar/prop value of 0.95 and lidar/sonics value of 0.98.

The last category investigated was influenced by the shadow of the tower structure region (Cermak and Horn, 1968). With a regression constant of 0.99, the wind speeds for the lidar/prop analysis (Table 3.11) did not appear to be affected by tower shadow for the category of wind >3 m/s. The low wind cases had poor agreement; the constant was with a large and the r^2 dropped to near zero. The lidar/sonics agreement was similarly poor for the low wind speed cases within the shadow, with an r^2 of 0.25.

3.4.3 Wind direction comparison

Table 3.8 gives the error analysis for the wind direction comparison. For all cases the lidar/sonic comparison gave a standard error of 7.4° and the lidar/prop comparison a standard error of 7.1° . The comparison of the in situ sensors gave a standard error of 3.8° . The r^2 value for all three of the comparisons was excellent, all being greater than 0.99. The lidar scanner used at the time of the BUCOE experiment was oriented by magnetic compass and not set to a terrain reference directional zero point before doing the runs, so the absolute direction was unavailable. This introduced a systematic bias in the lidar wind directions as seen by the offset in the regression analysis.

The first step in analyzing the wind direction comparison was to look at the systematic bias introduced by the instruments. The sonics and prop data appear to suffer from a systematic bias overall of approximately 3° . The low wind speed category had systematic bias in the prop and sonics data which appears to be to a large extent due to tower shadowing. Figure 3.14 gives the deviation pattern in the low wind speed cases. Note that the wind directions appear to deviate around the tower structure.

Table 3.11. Wind speed error calculation within tower shadow

Regression output	Prop shadow Lidar vs. prop	Sonics shadow Lidar vs. sonics
<u>Shadow all</u>		
Constant	-0.03	1.04
Std. err. of Y est.	0.64	0.49
R squared	0.99	0.25
No. of observations	20	4
Degrees of freedom	18	2
X coefficient(s)	1.03	0.65
Std. err. of coef.	0.02	0.79
<u><3 m/s shadow</u>		
Constant	2.79	
Std. err. of Y est.	0.51	
R squared	0.00	
No. of observations	6	
Degrees of freedom	4	
X coefficient(s)	-0.05	
Std. err. of coef.	1.11	

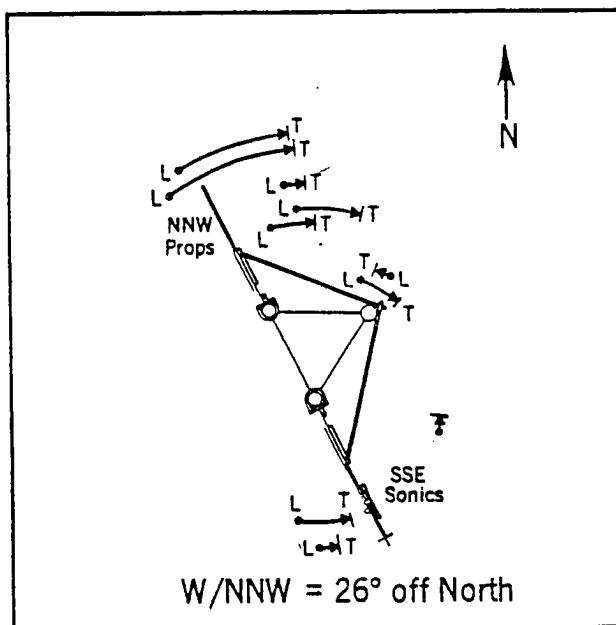


Figure 3.14. Polar plot of wind direction deviation pattern for low wind speed cases. T - tower wind direction; L - lidar wind direction. Tower structure is at center of figure, north is aligned to top of page.

The wind direction comparison was organized into categories for investigation of the differences between the sensors. The categories were defined by (1) tower-shadowed regions (Kaimal, 1978), (2) the wind speed categories (Table 3.12) and (3) wind direction (Table 3.13).

Although shadowing effects were expected for the prop sensor sectors 300° and 40° and for the sonics sensor sectors 90° and 190°, the more significant factor seemed to be the wind speed. The r^2 in the prop comparison, where 21 cases were within the area expected to be shadowed (Table 3.14) was 0.86, the low speed cases having an $r^2 > 0.99$. The low number of sonics values in the shadow of the tower decreased any overall effect on the comparison with only a minor affect on the r^2 0.96 vs. 0.99.

Of more importance than the direction categories were wind speed categories, especially when the combination of shadowing effect and low wind speed was present (Table 3.14). The wind speed categories >10 m/s and 3-10 m/s did not seem to have different characteristics in the wind direction cases; r^2 was greater than 0.99 for all comparisons and biases were consistent. The lidar/sonics 0-3 m/s category exhibited an increase in the standard error to 8.6° and a change in the bias from the other categories of 10°. Similarly the lidar/prop comparison had a standard error in this category of 8.3° with an 11° bias. Stability analysis of the 0-3 m/s wind speed category showed multilayered boundary layers, and changes of stability between tower levels. Since the VAD technique cuts through existing layers, and the area it investigated is not colocated with the in situ sensors, the agreement could be expected to suffer. The sonics/prop comparison was less sensitive in all wind speed categories; standard errors varied from 1.3° to 3.8° and difference from the overall biases was -6.6° to 0°.

The wind direction categories were determined by overall fit to the data excluding the low wind speed category. The sector 270°-340° appeared to compare poorly with r^2 's of 0.83 for the lidar/prop and 0.69 for the lidar/sonics comparison. The bias was also affected in this region; values were 94° and 111° respectively, with error estimates of only 6.3° and 7.9°.

Table 3.12. Lidar/tower wind direction comparison
sorted by wind speed

VAD (degrees)	Sonic (degrees)	Prop (degrees)
359.21	25.37	20.80
4.68	36.36	30.77
5.13	28.80	26.10
7.93	36.61	31.61
246.33		276.91
25.76	49.70	44.79
255.11	271.54	280.92
227.78		255.92
11.62	33.12	28.28
339.87		0.34
13.09	33.15	28.60
16.69	44.43	38.58
297.42	312.78	316.61
18.34	42.96	37.16
7.04	35.23	30.86
343.42	15.12	14.23
16.2	44.57	38.68
299.82		322.34
72.34	92.75	90.75
348.09	22.04	20.82
293.41	319.82	313.48
87.73	119.79	120.89
32.64	67.61	63.91
34.07	63.45	59.69
142.78	166.11	168.03
140.44	157.56	160.67
41.77	59.65	56.30
119.75	146.81	150.12
312.13	353.58	359.68
327.35	354.09	358.38
154.64	164.64	165.88
327.37	354.69	358.58
318.74	354.64	359.73
330.61	12.07	12.26
4.69	27.04	23.41
357.09	40.15	37.16
79.98	100.14	105.53
191.39	185.23	185.55

Table 3.13. Lidar/tower wind direction comparison
sorted by direction

Lidar	Sonic	Prop
5.76	29.70	24.79
12.64	47.61	43.91
14.07	43.45	39.69
21.77	39.65	36.30
52.34	72.75	70.75
59.98	80.14	85.53
67.73	99.79	100.89
99.75	126.81	130.12
120.44	137.56	140.67
122.78	146.11	148.03
134.64	144.64	145.88
171.39	165.23	165.55
207.78		235.92
226.33		256.91
235.11	251.54	260.92
273.41	299.82	293.48
277.42	292.78	296.61
279.82		302.34
292.13	333.58	339.68
298.74	334.64	339.73
307.35	334.09	338.38
307.37	334.69	338.58
310.61	352.07	352.26
319.87		340.34
323.42	355.12	354.23
328.09	362.04	360.82
337.09	380.15	377.16
339.21	365.37	360.80
344.68	376.36	370.77
344.69	367.04	363.41
345.13	368.80	366.10
347.04	375.23	370.86
347.93	376.61	371.61
351.62	373.12	368.28
353.09	373.15	368.60
356.2	384.57	378.68
356.69	384.43	378.58
358.34	382.96	377.16

Table 3.14. Wind direction calculation within tower shadow

Regression output	Sonics vs. prop	Lidar vs. sonics
<u>Sonics shadow all</u>		
Constant	0.12	32.94
Std. err. of Y est.	2.48	6.80
R squared	0.99	0.96
No. of observations	7	7
Degrees of freedom	5	5
X coefficient(s)	1.01	0.90
Std. err. of coef.	0.03	0.08
<u>Prop shadow all</u>		
	Sonics vs. prop	Lidar vs. prop
Constant	76.74	107.98
Std. err. of Y est.	1.06	7.23
R squared	0.99	0.86
No. of observations	19	21
Degrees of freedom	17	19
X coefficient(s)	0.78	0.76
Std. err. of coef.	0.01	0.07
<u>Prop shadow < 3 m/s</u>		
	Sonics vs. prop	Lidar vs. prop
Constant	-3.05	18.98
Std. err. of Y est.	3.77	6.73
R squared	1.00	1.00
No. of observations	7	7
Degrees of freedom	5	5
X coefficient(s)	1.02	1.06
Std. err. of coef.	0.01	0.02

4. INVESTIGATION OF THE FLUCTUATING-FLOW VELOCITY FIELD

Removal of the mean wind from the lidar scan leaves the residual components of the wind. Evaluating and identifying the residual components allows examination of mesoscale phenomena occurring within the volume scanned by the lidar. Typically the lidar takes 30 - 120 s to complete a 360° scan. Fluctuating field components can be traced in time and space by comparing sequential scans. The information on size and position of fluctuating components allows characterization of the non-mean flow for a given site, information that later could be applied to land use, terrain effects, and modeling applications.

4.1 Theoretical Considerations

A group of assumptions are inherent in the removal of a "mean" wind. The model parameters used to describe the "mean" for a particular flow field can affect what will be removed. Earlier it was noted that the "mean" reported by the sonics and the prop are defined differently. It is important, therefore, to be aware of the problems that can exist in both definition and technique used in mean removal process when applied to lidar cases.

One of the first requirements in calculating a mean by use of the VAD technique as defined in Browning and Wexler (1968), is the presence of a relatively homogeneous wind field over the scan area. Since a single mean will be removed, it is important that the calculated mean flow should not cause nonrepresentative changes over the areas scanned. Fields that were removed from the BAO comparison earlier included frontal passages and uneven boundary layer growth. These conditions caused a lack of homogeneity in the scan area.

Appendix B and C gives the original derivations and the applicable assumptions used to evaluate winds, using radars with the Browning and Wexler (1968) VAD (BW-VAD) technique. The assumptions in the original model were (1) the velocities can be described as a center velocity figure V_{x_0} and V_{y_0} , and deviations from the center velocities are defined as the first derivatives from the center velocities along the path, (2) fall velocities are approximately zero, (3) mean vertical velocity applies over the entire area scanned, and (4) there are no discontinuities (i.e., frontal passages) in the scanned area. The end result from the derivations given is a collapsing of the equations describing

the flow field into a harmonic analysis of the radial velocity. Several techniques can be applied to calculate the harmonic content of a data series. A number of possible mathematical techniques for data reduction require either dedicated hardware (FFT processors) or rigid assumptions (i.e., powers of 2 for number of points in a 360° scan) on the scan method.

To take advantage of the flexibility of the lidar scanning technique, the least squares (LS) fit technique was used to determine the harmonic contents of the data sequences. The LS technique yields a Fourier series, given complete cycles of data, and allows analysis of any data rate, spacing, and extent. Appendix E gives the LS technique as applied to the lidar data. Also given in Appendix E is the technique as it applies to sample scan conditions and assumptions. Because the mathematical techniques used to provide the mean wind analysis are sensitive to the degree of agreement of the experimental and assumed conditions, the test velocity patterns give an indication of problems that occur in analysis of experimental VAD patterns.

As a result of the test cases in Appendix E, certain processing decisions were made. The best analysis technique was determined to be (1) to use complete cycles to define the mean that would be removed from the data; (2) to use the least squares-first harmonic technique because it produced more consistent results and required fewer assumptions about the flow field.

4.2. Investigating the Non-Mean Wind Field

The convective boundary layer (CBL) was chosen as the ideal regime for the study of the perturbation wind field due to two of its characteristics. First, the CBL is defined as having a well-mixed aerosol population. Since the lidar reflects off the ambient aerosols, an evenly distributed aerosol population provides a good sampling of the velocities. Second, since the lidar is ground based, the closest atmospheric region to the lidar scanner is the boundary layer. As a boundary layer tool the lidar has some significant advantages. Unlike an in situ sensor, the lidar can conduct non-intrusive sensing of a region. Furthermore, it can change scan techniques to follow boundary layer features as they develop. Because the lidar can sample a large area, both an overall view of the developing boundary layer and a detailed view of the larger features are possible.

4.2.1 Experimental Plan

The experimental plan for the study was designed to maximize the information available from sampling of the CBL. The lidar's maximum sampling rate is 10 Hz. In order to have enough information for a stable velocity estimate, it is important to average more than one pulse for each velocity measurement. The radial dimension is not selectable; rather it is set by the processing mode of the instrument. Taking into consideration the possible parameters the experimenter can control, an experiment was set up where the rotation rate was slowed to allow at least one velocity measurement per degree of angle. The time tradeoff places the time to complete the 360° scan at 10 Hz with three-pulse averaging at approximately 108 s. Since the scanner moves from 0° to 360° and then reverses for a 360° to 0° scan, the time change to rescan any region is a function of both the angle and the distance from the 0/360 point. As an alternative, less than a 360° area can be scanned to rescan areas more quickly. A series of scans of a 90° sector was also planned to allow more detail in some measurements.

The unadjustable range resolution puts some limitations on the scan. Although resolution azimuthally was set to allow more than one data sample per degree, along the radial the resolution is either 300 or 500 m. This limits the resolution of smaller scale features and slightly elongates the features that are seen. Since the lidar senses points along the radial, some discontinuity between the independent radial measurements is also expected. In this study the lidar's measurements are treated as though the time scale for each scan is not important to the results of the scan. Since there is a finite time required to complete each scan, this causes some loss of fine-scale resolution.

4.2.2 Description of received wind field

Browning and Wexler (1968) described the model wind fields for the VAD technique by defining a center value for velocity in the two horizontal dimensions and a linear trend for the velocities as the distance from the center of the VAD increases. Although this may be appropriate on the synoptic scale, a different approach is important when considering smaller scale wind regimes. The traditional nomenclature for local velocity in the convective boundary layer is given by Kaimal et al., (1972):

$U = \bar{u} + u'$: The longitudinal component of the wind or the along-wind direction component.

$V = v'$: The latitudinal component of the wind or the component of the wind perpendicular to the mean wind direction.

$W = w'$: Vertical velocity, assuming no net mean vertical motion.

When these equations are translated into the radial velocity terms representing the velocity as seen by the lidar, the following results:

$$V_{\text{radial}}/\cos\phi = (\bar{u} + u')(\cos\theta) + v' \sin\theta + w' \tan\phi$$

where ϕ = zenith angle θ = mean wind direction.

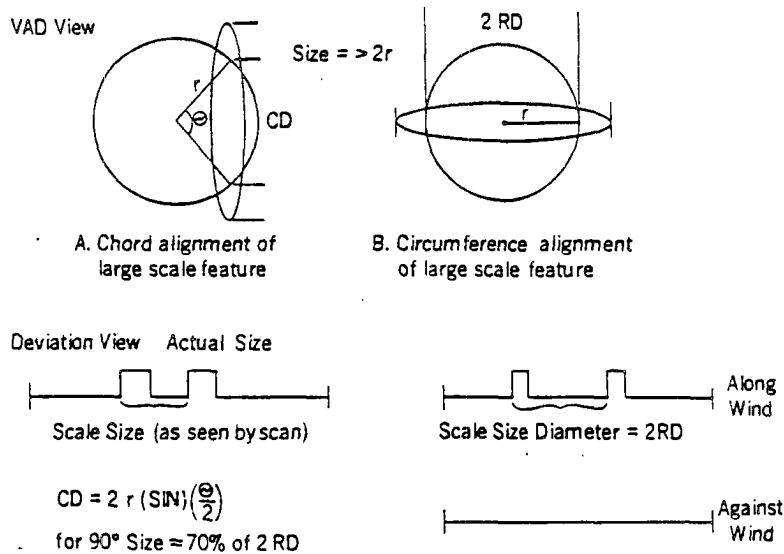
Regrouping terms:

$$\begin{aligned} V_{\text{radial}} &= \bar{u} \cos\theta \cos\phi \\ &+ u' \cos\theta \cos\phi \\ &+ v' \sin\theta \cos\phi \\ &+ w' \sin\phi. \end{aligned}$$

It is important to note that the field resulting from use of the CBL definitions varies considerably from the Browning and Wexler VAD (BW-VAD) derivation. Where the origin in the BW-VAD derivation is the location of the radar, the above CBL derivation places no position for the zero velocity location. The higher level harmonics that develop from the assumptions of movement away from the origin of the BW-VAD universe do not develop in the CBL derivation. The first harmonic fit in the CBL defines the mean wind speed and direction, and further harmonics provide information on the combined prime terms of the wind derivation.

4.2.3 Expected structures

The first step in looking for the non-mean field was to identify the type of CBL structure one can highlight. The size limitations in the azimuthal direction are defined by the scan rate and number of pulses averaged together. For data taken at $3.33^\circ/\text{s}$ using a 10-Hz data acquisition rate and averaging three pulses, data are available approximately every 20-30 m. To define a feature at least two data points are needed, which limits the minimum identifiable feature size to 40-60 m in the azimuth coordinate. This essentially eliminates horizontal scales of motion under 50 m, which includes isotropic turbulence and many of the surface layer structures. The upper limit of the size scales identifiable using the lidar could be defined either as (1) the circumference of the scan or (2) the chords of the last range ring from which velocities could be received and processed by the lidar (Fig. 4.1). Since the largest size limit of the features size can scale with two equally probable scaling numbers (around the circumference or across the circle), some problems in evaluating larger size ranges should be expected.



a) Feature is larger than one radial belt and is bisected by the scan twice in less than the diameter of the scan. The actual size can only be determined by combining a number of belts along a chord.

b) Feature is larger than the scan area and is bisected by the scan across the diameter. Actual size can be determined by comparison of the radial belts in proximity to the feature.

Figure 4.1. Large feature scaling for lidar VAD scan.

The second horizontal dimension for the lidar return is along the radial. The sampling rate along the radial is controlled by the pulse length and processing technique. The moment data processor uses a range gate of 300 m. Data taken in the raw mode with a 3.3 μ s pulse length is best centered with a gate length of 500 m. A schematic of the area horizontally covered by each data point is given in Fig. 4.2.

Boundary layer features that can be seen at smaller scales (50 m to 50 km azimuthally and 300 to 15,000 m radially) include cloud rolls, thermals, cloud roots, dust devils, and terrain-produced perturbations. On the larger scale, storm circulations, valley and mesoscale terrain flows, and irrigation and lake effects might be identified.

Thermal plumes (thermals) (Fig. 4.3) were chosen for the initial investigation, for three major reasons:

(1) Convective conditions occur daily during the Colorado summer. The low relative humidity that is typical of the area supports dry-air thermal structures. By eliminating moisture gradients from the study, interpretation of the dynamic structures is simplified.

(2) Features such as cloud rolls are not present every day in Colorado. Summer conditions that support dry convection are present a majority of the days in a Colorado summer, to the point where it can be assumed the conditions will prevail unless frontal passage or other exceptional weather is expected. This makes the choice of days available for scheduling the experiment much larger than if other features were investigated.

(3) The spatial distribution of thermals has been measured as between 20-40% of the boundary layer area; the number of thermals present and their size are dependent on the depth of the boundary layer (Lenschow and Stephens, 1980). The typical boundary layer height in Colorado ranges from 1 to 2 km (Kaimal, 1980). The thermal size ranges from 200 m (Warner and Telford, 1967) to 700 m in diameter for Colorado conditions (Lenschow, 1970). Although smaller thermals were excluded from the size range of features the lidar can sense, the larger thermals with a velocity deviation field should be identifiable.

In order to cover enough area for a good representation of the boundary layer, the lidar scanned arcs of at least 90° up to 360°, with radial extent of

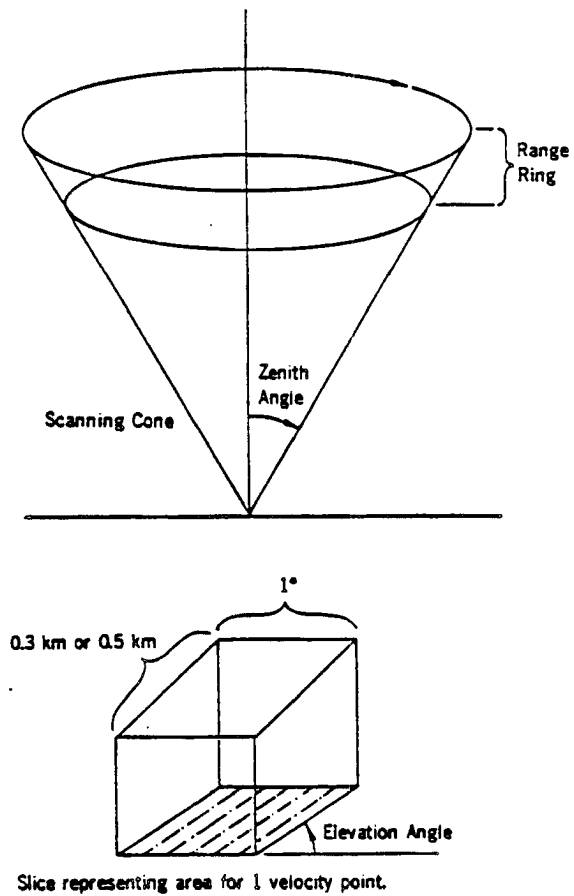


Figure 4.2. Horizontal area covered by a VAD scan made by the Doppler lidar.

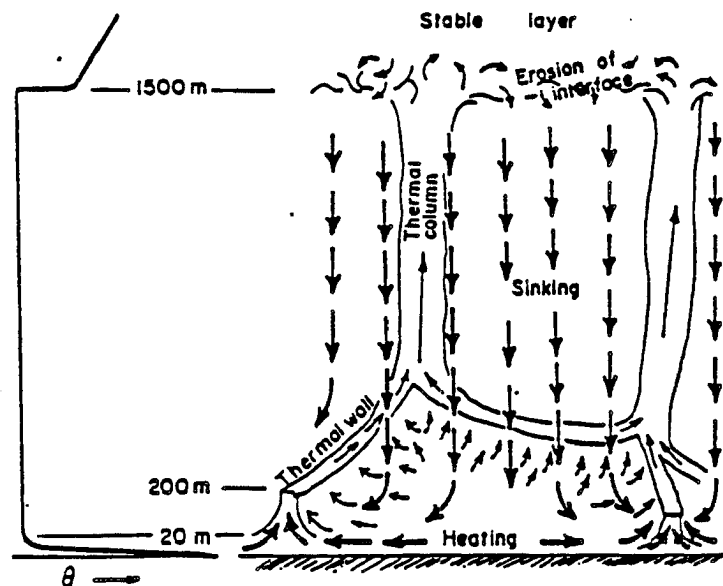


Figure 4.3. Thermal scale features (from Ting and Hay, 1977).

10-15 km. Average thermal size was set to 450 m, representing the center of the range given by Lenschow (1970). There should be approximately 60 intersections in a 360° scan, and 15 intersections for the 90° scan. Elevation scans of 2°-10° provided coverage of a vertical area between 50 m above ground level and 1700 m above ground level.

The equations developed in Sec. 4.3.1 demonstrate that removing the mean wind from a series of radial Doppler signals gives a residual deviation field that represents a combination of the u' , v' , and w' wind components. The traditional indicators for thermals are temperature, humidity, vertical velocity, and turbulent kinetic energy (Warner and Telford, 1967; Manton, 1977; Coulman, 1978; Hall et al., 1975). Since the traditional indicators are not sampled by lidar, a detectable horizontal wind signature for thermal feature had to be developed.

The first step in determining a horizontal wind signature was to make some assumptions on the flow in the experimental area. Lenschow and Stephens (1980) state that horizontal convergence into a thermal should be constant with height in the free convective layer. If that observation is used and continuity is assumed for the flow in the region, a change in the vertical velocity (which is a standard thermal indicator) in an area should be reflected in the horizontal wind field. The mean flow is not changing on the thermal scale, so the deviation horizontal flow field should be the field that would reflect convergence and therefore changes in the vertical velocities. Figure 4.4 demonstrates how these changes in the wind field would be reflected in the radial wind signature. With this in mind, the deviation horizontal wind field should indicate the presence of thermals in an area being scanned by the lidar.

4.2.4 Deviation field analysis

The equations developed in Appendix C were used to investigate the deviation fields for a number of lidar runs. The fields were created using the LSFH technique to remove the mean wind field from the radial data. Data were investigated in (1) the radial direction, (2) a two-dimensional form from data in consecutive VADs, and (3) a three-dimensional form from data taken in first incremental radial then incremented azimuth form. The fields were analyzed to

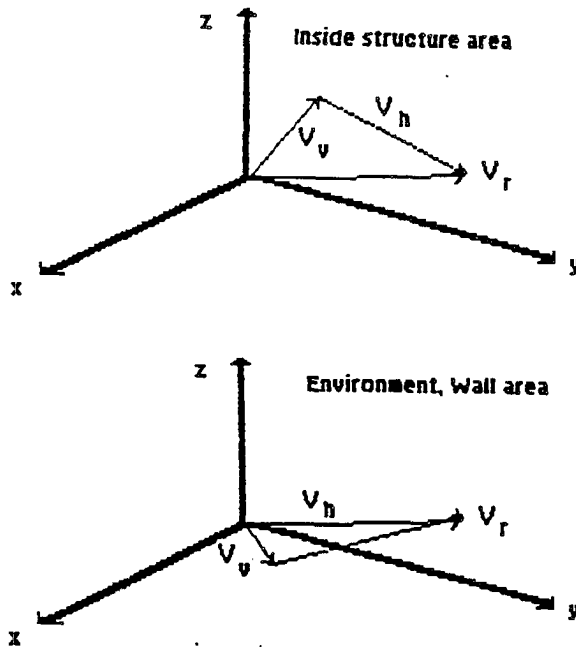


Figure 4.4. Reflection in VAD field of vertical velocity changes expected in a convective plume.

(1) highlight deviation continuity in time and space, and (2) document deviation flow patterns, looking particularly for thermal-size deviation patterns.

4.2.5 Cases analyzed

4.2.5.1. One-dimensional case

The first run (data collection sequence) was designed to investigate the continuity of the lidar velocity returns for duplicate runs made at the same elevation angle over the same horizontal area. A series of scans was made at 3° elevation. The 3° elevation angle provides a 99.9% return of the horizontal wind components and a 5% return of the vertical wind in the area. Moving along the radial, the ratio of height above ground to distance horizontally from the lidar is also 99.9:5.

The analyzed run was taken on 23 June 1984 near 1500 MDT. Dry convective boundary layer conditions prevailed, with no clouds in the experimental or surrounding area. The ground in the area was dry, with early crops in the surrounding fields. No large-scale irrigation was being done in the area, and the fields were green. Mean winds were low, and solar heating was substantial. According to the scans being done at other elevation angles, the change in wind

speed and direction indicating the transition from the boundary layer to the free atmosphere occurred more than 1.5 km above ground level. Changes in the top of the boundary layer were monitored with scans before, during, and after the experimental run.

Initial runs were made in the raw mode, which produces data in 500-m gates (radial increments). Two VAD runs were done; less than 5 min elapsed from the start of the first run to the end of the second run. Three pulses were averaged together from the 10-MHz data, which gave approximately one data point per degree around a 360° circle. The mean wind was calculated separately for each of the complete circles, and removed. The resulting deviation fields for a 60° arc around the mean wind direction are given in Figure 4.5a and b.

A comparison of the highlighted areas in Figs. 4.5a and 4.5b shows good continuity in space along the radial belts in the deviation signatures. Figures 4.5a and 4.5b demonstrate the time continuity of the feature. The size of the area was approximately 0.4 by 1.5 km, slightly longer than predicted for a thermal signature. The feature also appears elongated along the radials. Figure 4.6 demonstrates the spatial representation of the feature in the two scans along the radial belts. The time between the two scans was 198 s, and the layer mean flow was 4.55 ± 0.40 m/s. With an expected probable error in wind speed, the movement would have been 900 ± 80 m or 980 m maximum, 820 m minimum displacement. The feature moved approximately 750 m, slightly less than the layer mean, as theory predicts.

4.2.5.2 VAD Case

In the one-dimensional case in Sec. 4.3.5.1, the scan was investigated to see whether "eddy" features seen by looking radially were reproduced in two consecutive scans. This section takes the analysis one step further and looks at the deviation-signatures around entire scans. Regions were investigated to highlight features' size, position, and movement.

Three contiguous VAD scans were performed using the moment processor. The gate size radially was 300 m, three pulses were averaged together by the processor, and the data rate was set such that at least one radial velocity estimate was available for every degree in azimuth. The elevation angle for the run

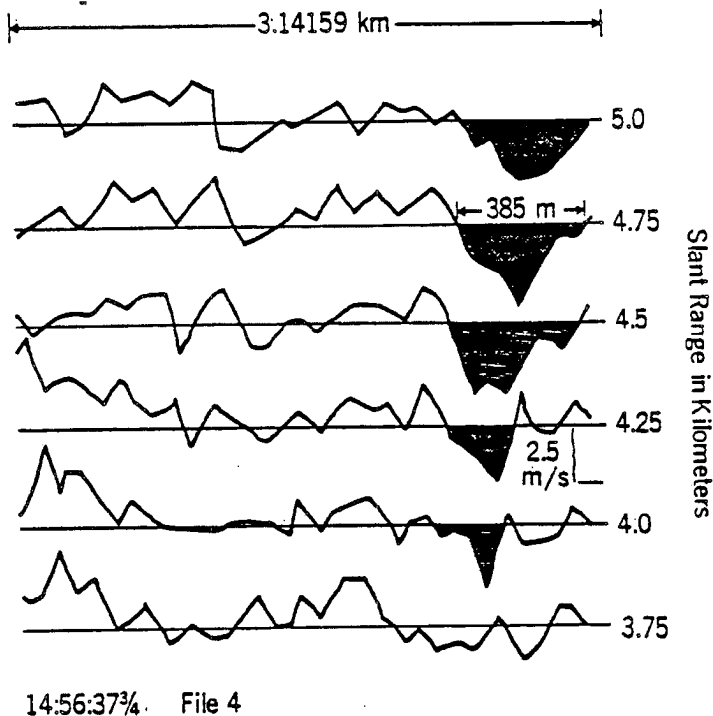


Figure 4.5a. Radial analysis of deviation flow pattern for a 60 degree arc around the mean wind direction. Shaded area represents feature under investigation. a) Run 1.

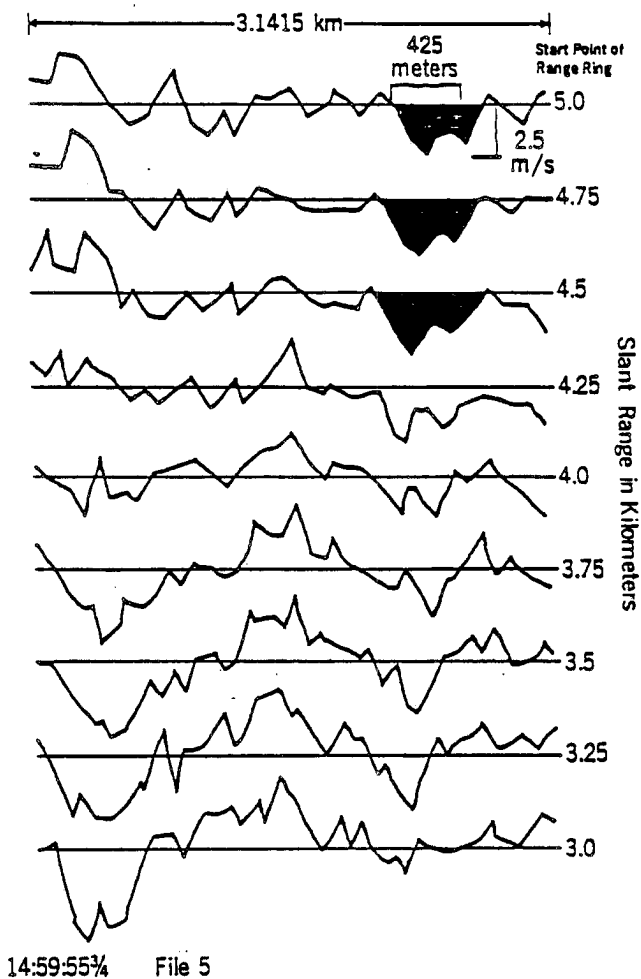


Figure 4.5b. Radial analysis of deviation flow pattern for a 60 degree arc around the mean wind direction. Shaded area represents feature under investigation. b) Run 2.

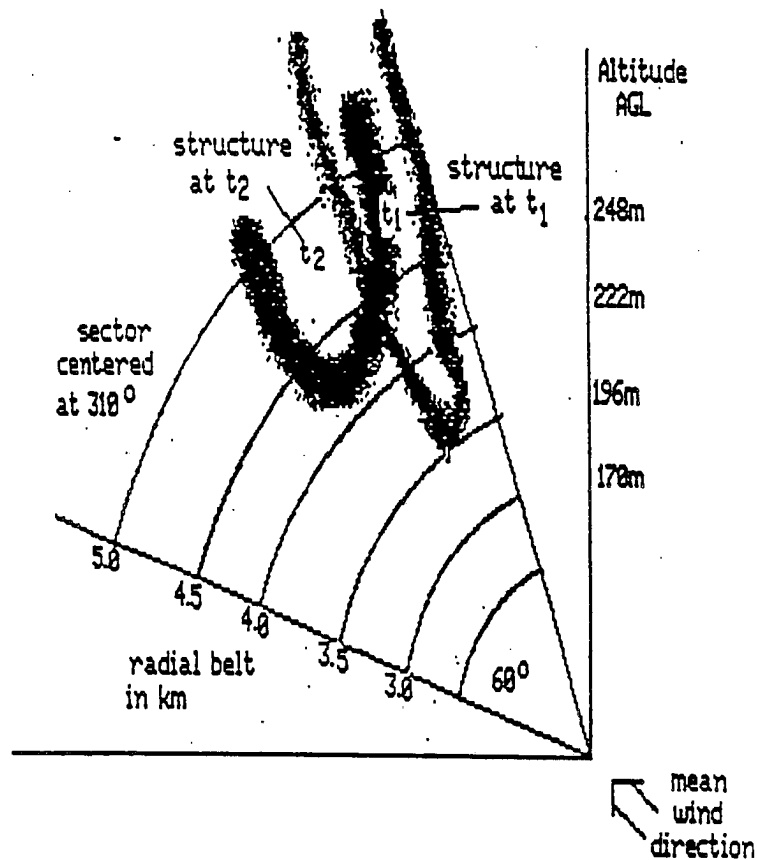


Figure 4.6. Trace of the movement of the feature identified in Figure 4.5a and b. t_1 is the approximate size and position of the identified feature at the first pass. t_2 is the approximate size and position of the identified feature at the second pass.

was chosen at 6° to minimize any surface layer effects and to cover a larger vertical extent with the scans. The runs were done just after maximum heating and after boundary layer growth had stopped, using VAD scans done surrounding the experiment time to delineate the conditions. The conditions during June were again dry convective, with early crop growth and little irrigation. The mean wind during the runs was again light (between 3 and 4 m/s) which allowed strong thermal growth, but limited advection of structural features with time. The runs were conducted in a continuous manner, with the first run from 21° to 360° , the second from 360° to 0° and the final from 0° to 360° .

The first post-processing step was to remove the mean from the VAD fields to uncover the "eddy" flow. Because the cycle was incomplete in the first case, the mean wind from the second full cycle was used as the mean removed from the first cycle. The second and third cycle means were calculated and removed from their respective scans. Minor imbalances in the remaining flow around radial

belts (due to convergence or large area differences) were corrected such that the "eddy" flow around the entire VAD scan would be zero. The remaining wind fields represent the deviation flow fields. It is important to note that the data fields have an increase in height with range. This is due to the scanner elevation angle of 6°. Figure 4.7 gives the height analysis for scans taken at 6° elevation. There may be an effect on the velocity deviation data due to the height of the radial belt within the boundary layer. Compensation for a possible height dependence was not analyzed.

Figure 4.8 gives a group of 90° sector contour plots of the deviation winds for the three runs. Overall, large areas of deviations with scales larger than expected for thermals are evident in the sector plots (Figure 4.9a,b, highlighted area on the 45° angle, 6 km long, as much as 1.5 km wide). This appears to indicate deviations on the scale that would be expected in mesoscale-influenced flows (terrain, heating differences, storm circulations). Additionally, no pattern of u' and v' fields appears as might be expected if the energy patterns of the deviation components differ (Kaimal et al., 1976). Deviation areas with the characteristic size range expected for thermals are most obvious in the 0°-90° quadrant contour area (a,d,h). Advection of patterns

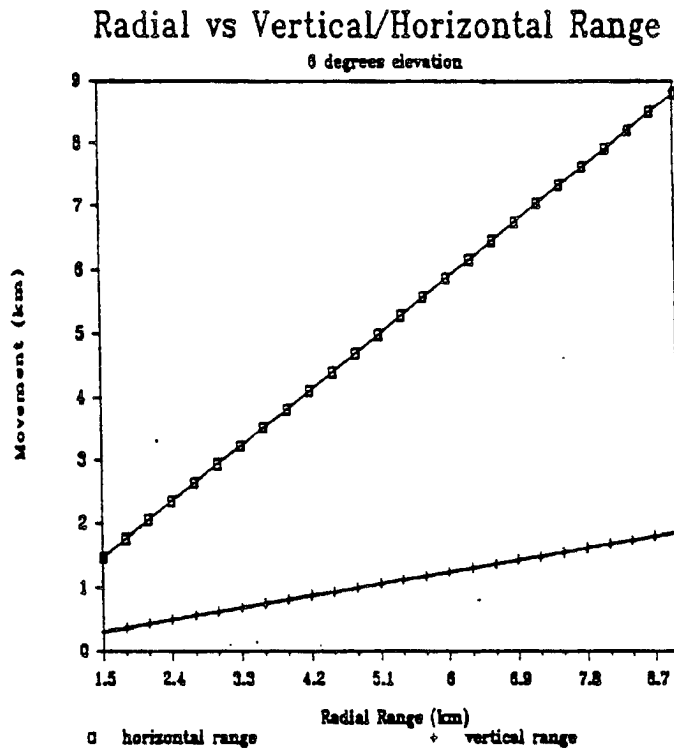


Figure 4.7. Vertical/horizontal displacement versus radial range for the area covered with a VAD scan done at 6 degrees elevation.

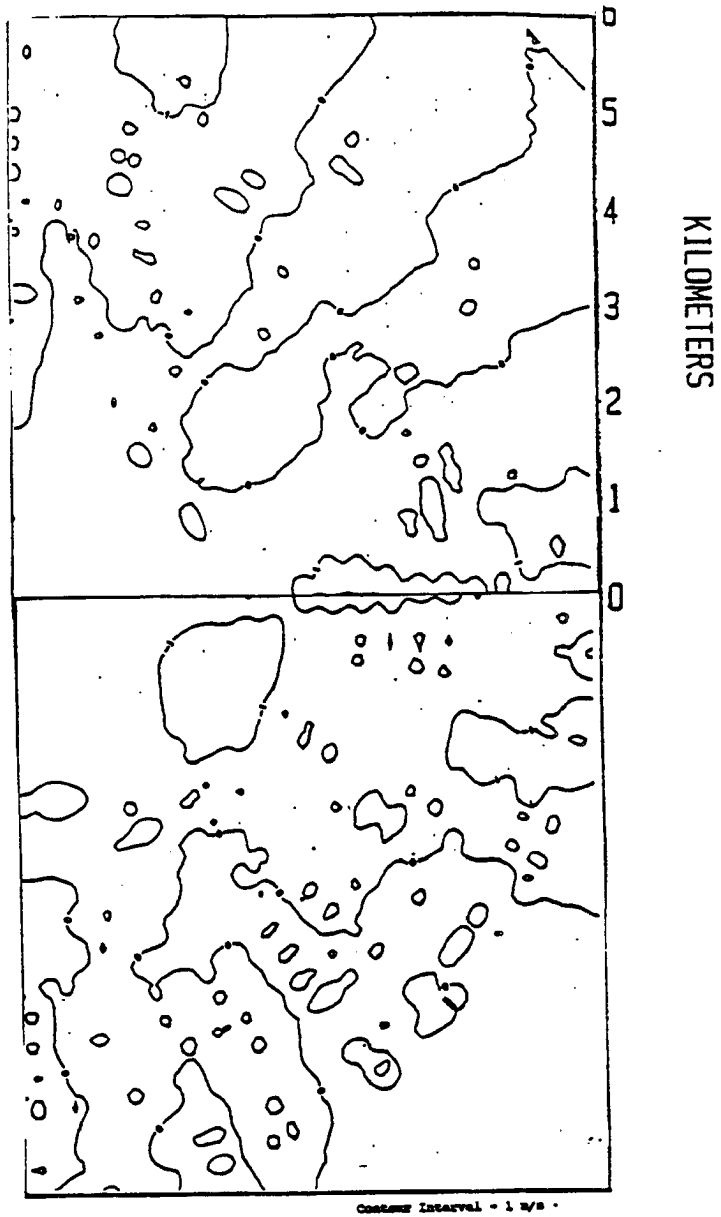


Figure 4.8a. Contour plot from a series of three contiguous VAD scans. Scan A, 0-180 degrees.

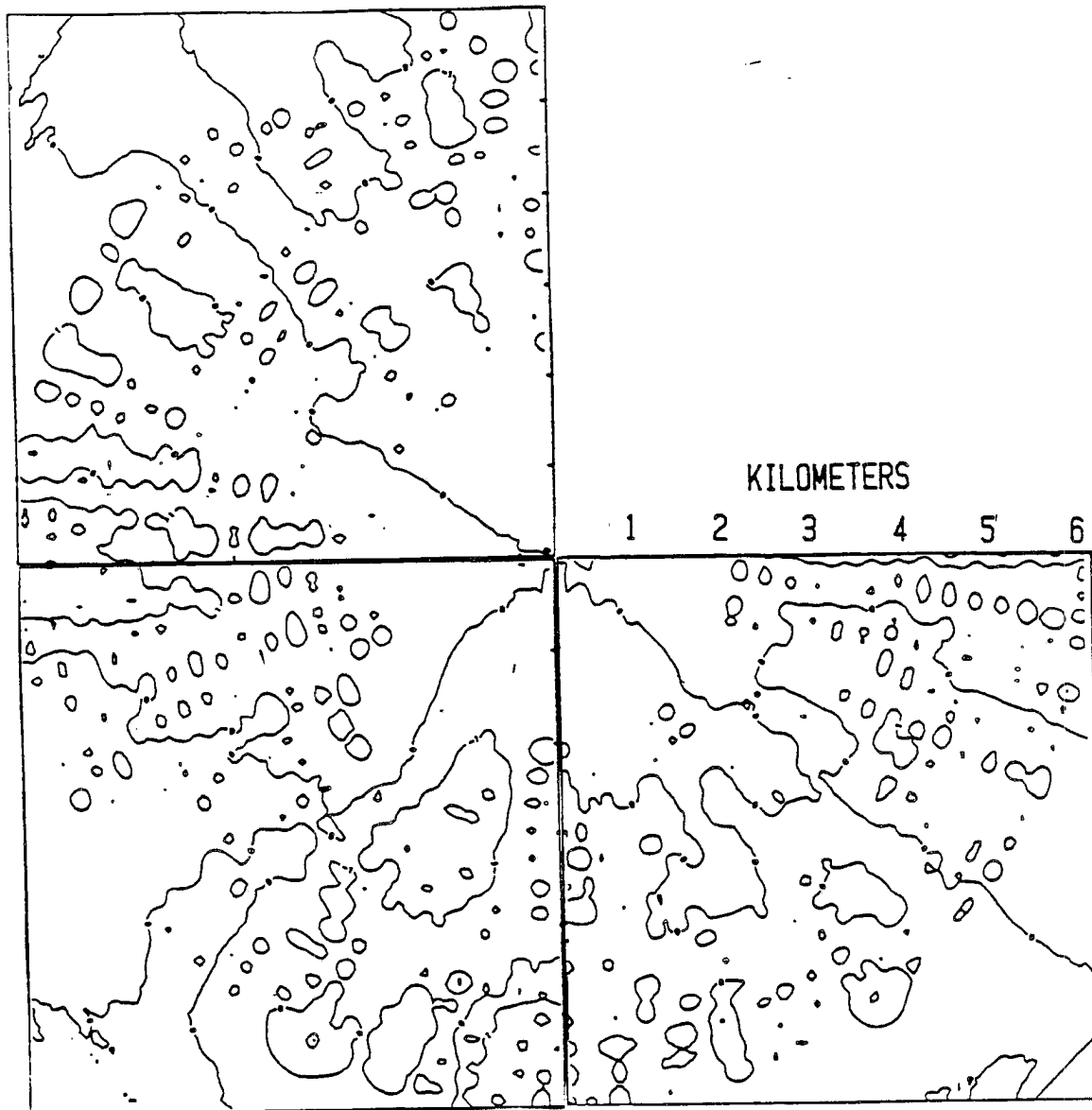


Figure 4.8b. Contour plot from a series of three contiguous VAD scans. Scan B, 90-360 degree sector.

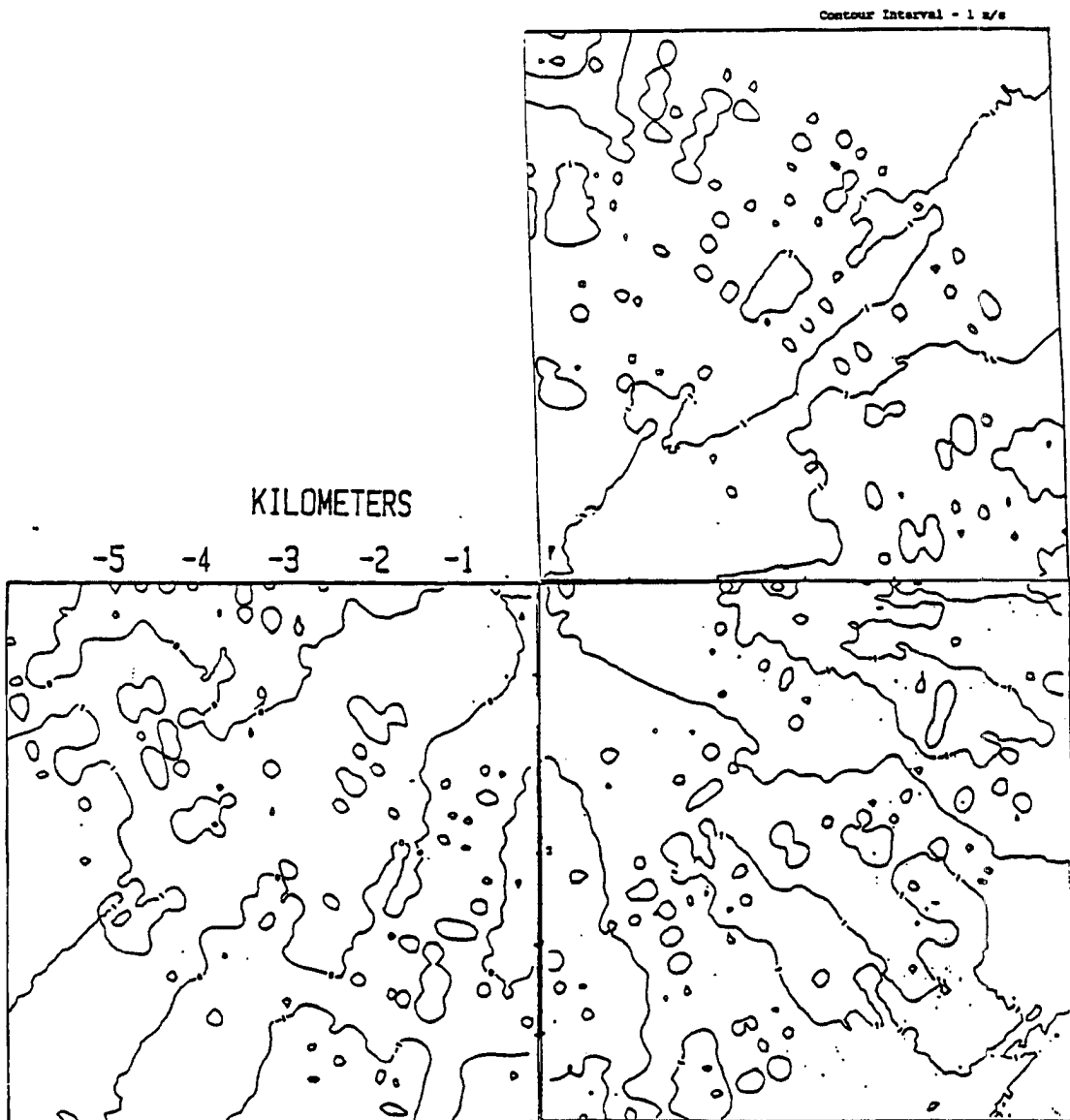


Figure 4.8c. Contour plot from a series of three contiguous VAD scans. Scan C, 0-270 degree sector.

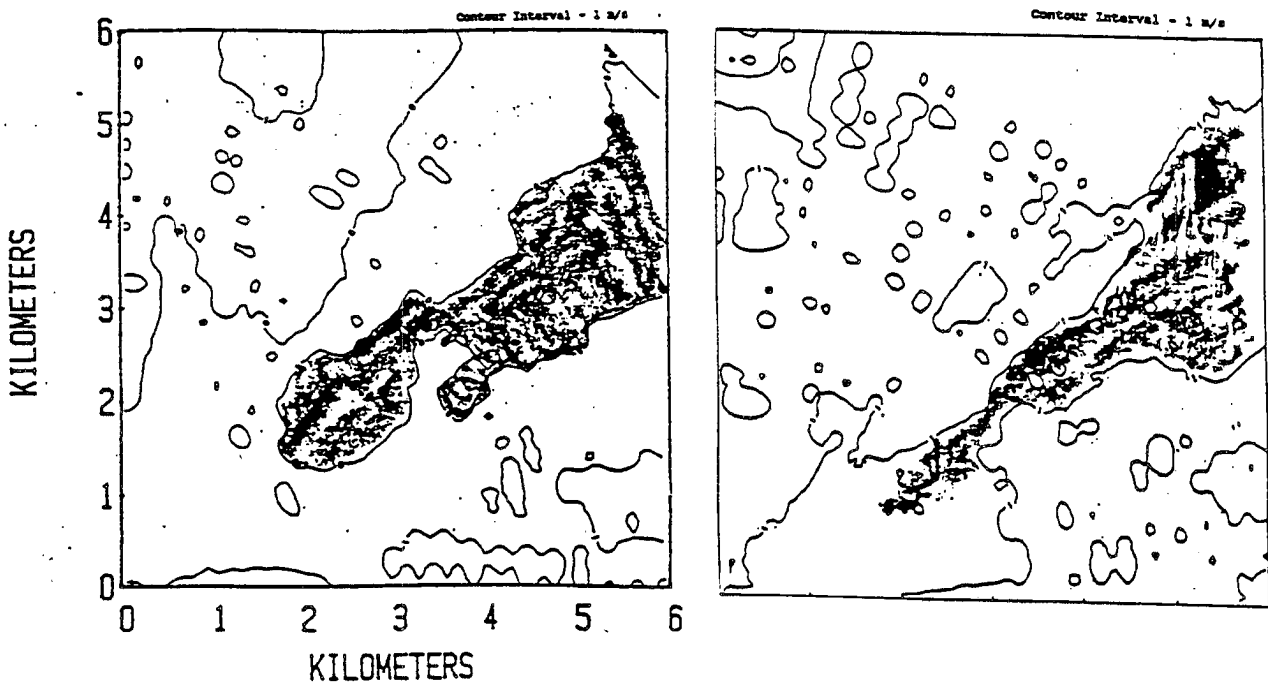


Figure 4.9. Highlighted areas with similar features located in consecutive scans. a) Scan B. b) Scan C.

with the mean flow (from approximately 100° - 120° at 3.5 m/s) appeared weak, and features with a variety of scale sizes moving throughout the area.

An analysis of the second and third complete scans was done to investigate the "eddy" velocity distribution by quadrant. This was done primarily to investigate the balance in each quadrant. Figure 4.10 gives a distribution analysis of the two scans. The third scan has a definite bias in the 0° - 90° quadrant and a bias of the opposite sign in the opposite quadrant, 180° - 170° . The wind direction, out of approximately 120° , would place these two quadrants in the v' region. The second scan, with a slightly lower wind speed, has less bias in the quadrants, but has significant differences between the 0° - 90° and 180° - 270° quadrants.

Thermal activity, as evidenced by features from 100 to 1000 m in size, did not appear to occur in any pattern, and also appeared to be relatively unskewed in any direction. Some radial dependence on shape was noted, but as the lidar has a set radial range resolution of 300 m under which features would not be defined, it was not unexpected. Figure 4.11 shows highlighted areas of thermal scale activity as seen from the second and third scans. The size scale of

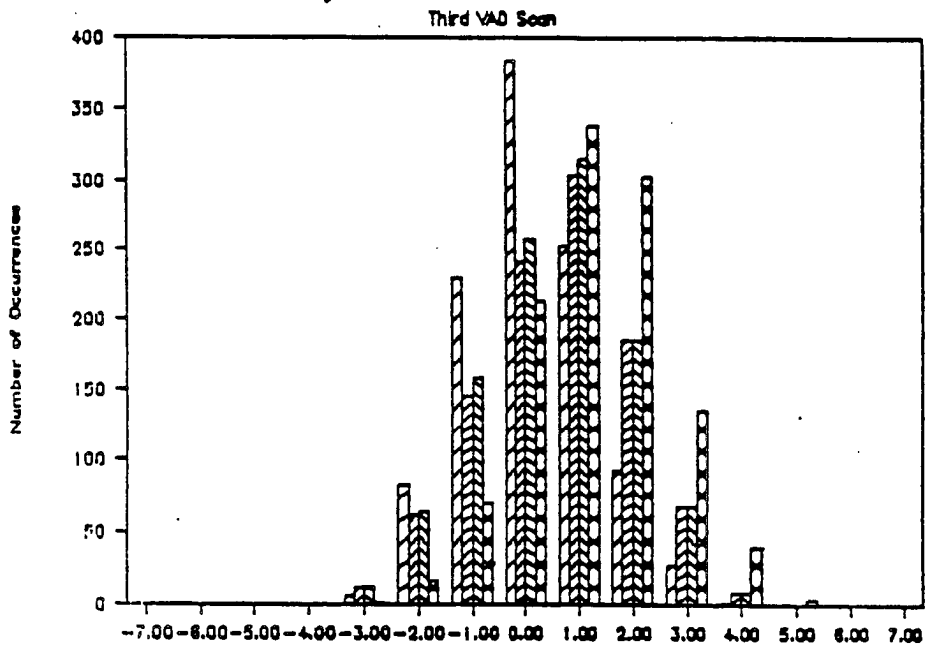
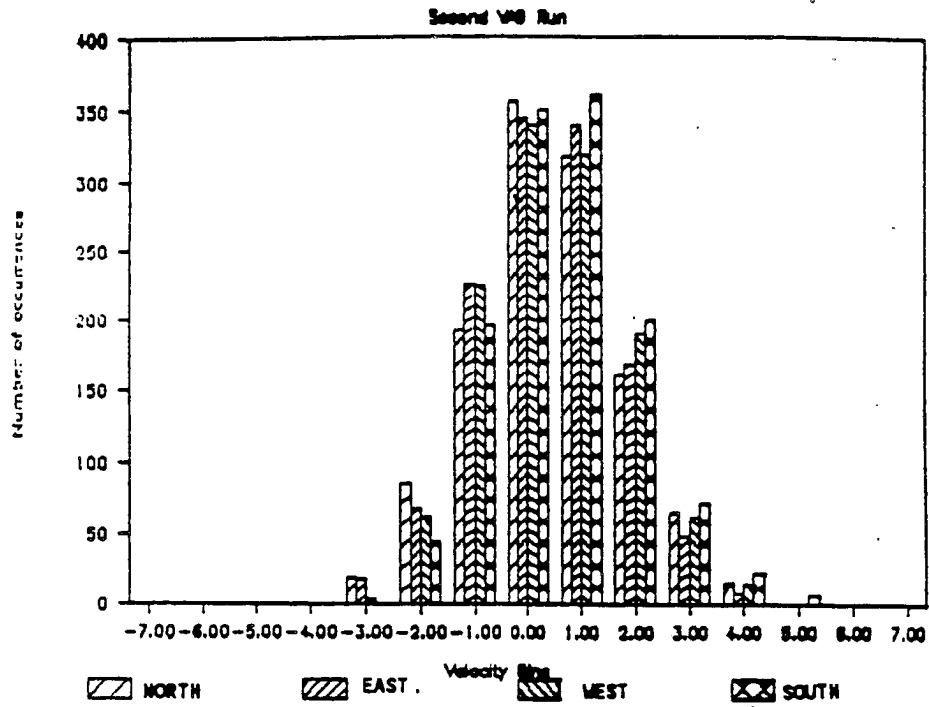


Figure 4.10. Velocity distribution analysis by quadrant. a) Upper plot is histogram for Scan B. b) Lower plot is histogram for Scan C.

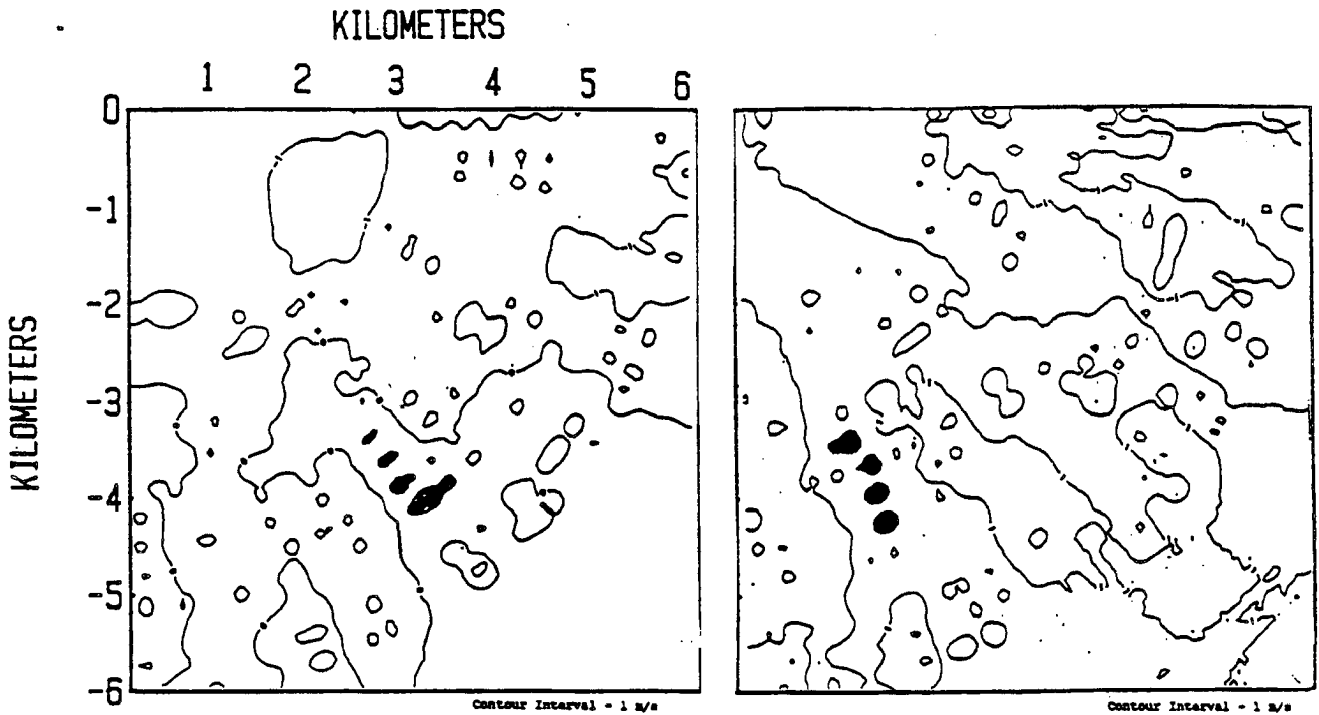


Figure 4.11. Highlighted thermal scale features seen in consecutive scans. a) Scan A. b) Scan C.

feature A is approximately 0.5 by 0.3 km, and the movement was approximately 1 km toward the southwest. The block of activity in feature B has a group of four perturbations, slightly smaller in scale (0.25 by 0.35 km). Net movement between scans is approximately 1.4 km to the west.

4.2.5.3 Combination vertical and horizontal scan

Lidar can provide an almost instantaneous snapshot both in the vertical and the horizontal. A three-dimensional snapshot of the boundary layer is useful in both tracing surface heating effects, i.e., thermal plumes, and larger scale perturbations of the boundary layer flow. To investigate this feature of the lidar scan, an experiment was designed to quickly cover a sector around the BAO tower and, stepping up in elevation angle, cover the same sector incrementing in height. Using the moment processor, scans were made in a 90° arc, with 2 to 3 radial velocity estimates per degree. The scan began at 2° elevation, and, stepping 1° in elevation per arc, and was stopped at 10° in elevation. The experiment was done the same day as the VAD case, slightly later in the afternoon, but before the boundary layer conditions changed. The mean flow from the VAD case was used to remove the first harmonic, and the flow was balanced such

that the deviations around the sector balanced to zero. Figure 4.12 gives a height analysis of the elevation stepping sector scan technique, showing the change in elevation for each of the scan increments and the corresponding change in the horizontal.

Figure 4.13 gives a vertical plot derived from the combination of horizontal scans done by the lidar during this investigation. The figure represents the horizontal deviation seen by rotating around the cylinder the VAD transcribes. Figure 4.14 gives the time/height cross section of a convective boundary layer reported by a Doppler sodar. Although sodar information is a time sequence, the deviation signatures are very similar in appearance: the elongated areas of enhanced deviation from the lidar scan roughly approximate the returns of the sodar vertical velocities. It is important to keep in mind that the lidar plot is not a vertical velocity figure; rather it represents horizontal flow discontinuities, which, using continuity, should form an image of the vertical changes.

5. RESULTS AND CONCLUSIONS

The investigations led to these conclusions:

- (1) Doppler lidar can be used as a fast, efficient and accurate mean wind measurement tool, using the VAD technique in a variety of weather conditions.
- (2) Removing the mean wind from a scan leaves significant information about the perturbation velocity fields in the scan area.
- (3) Perturbation features in Doppler lidar VAD fields can be traced in time and space, giving a temporal and advection history of a feature.
- (4) Spatial distribution of perturbation features can be documented by a Doppler lidar, and the changes in the distributions in time over large areas can be traced using the VAD technique in a variety of weather conditions.

The Doppler lidar winds were taken in a variety of meteorological conditions at the BAO site and were compared with measurements obtained with BAO wind sensors. The agreement was good, which demonstrated the lidar's useability and accuracy in a number of meteorological conditions. It also pointed out how

Cross-Sectional Vertical Plat

2-10 degrees elevation

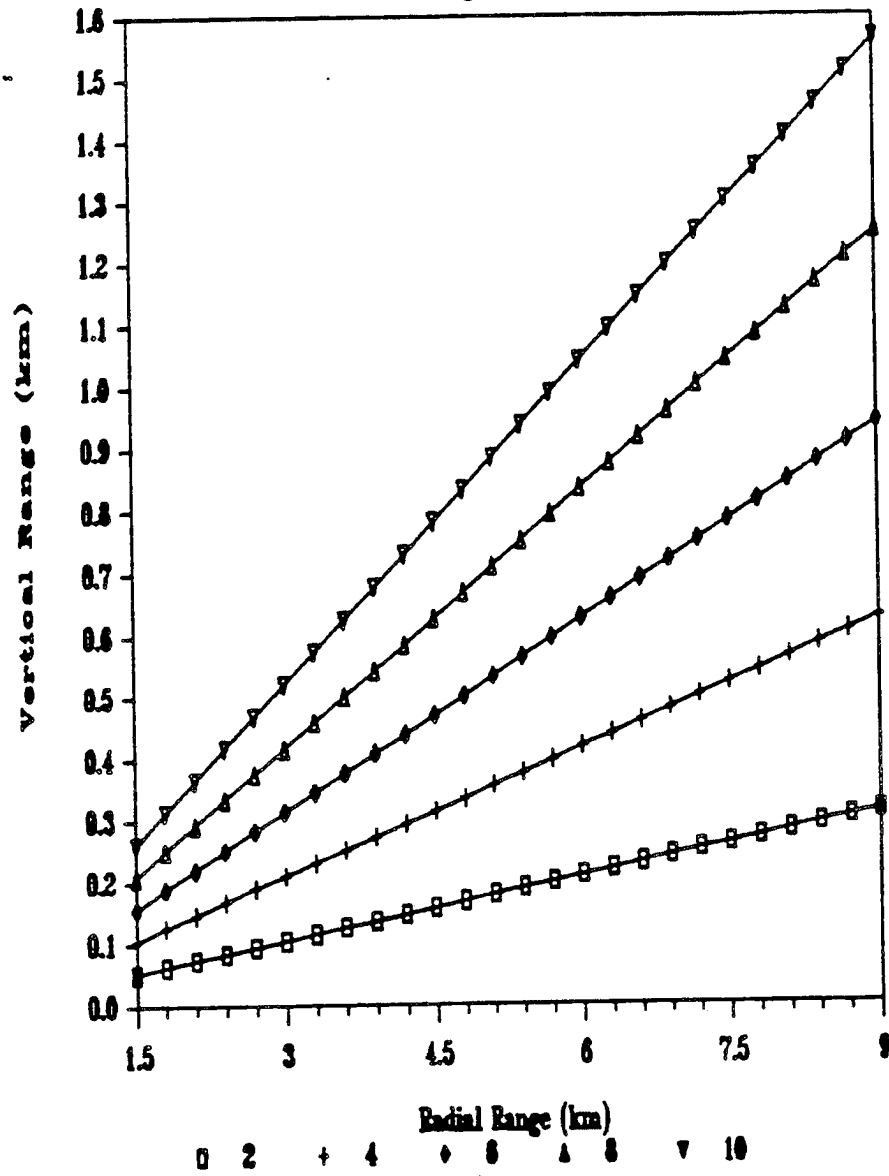
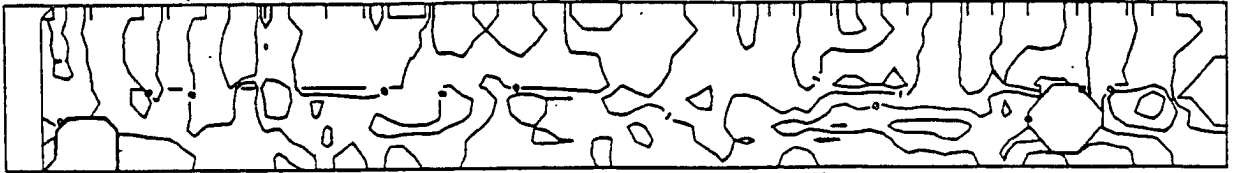


Figure 4.12. Height analysis of elevation stepping sector scans.



Constant Radial 5100 M

Figure 4.13. Plane analysis of one elevation step from a series of elevation stepping 90 degree sector plots. This scan is from the 5.1 kilometer range gate covering the sector from east to south, with the first information at 100 meters above ground and the highest information at 1200 meters above ground.

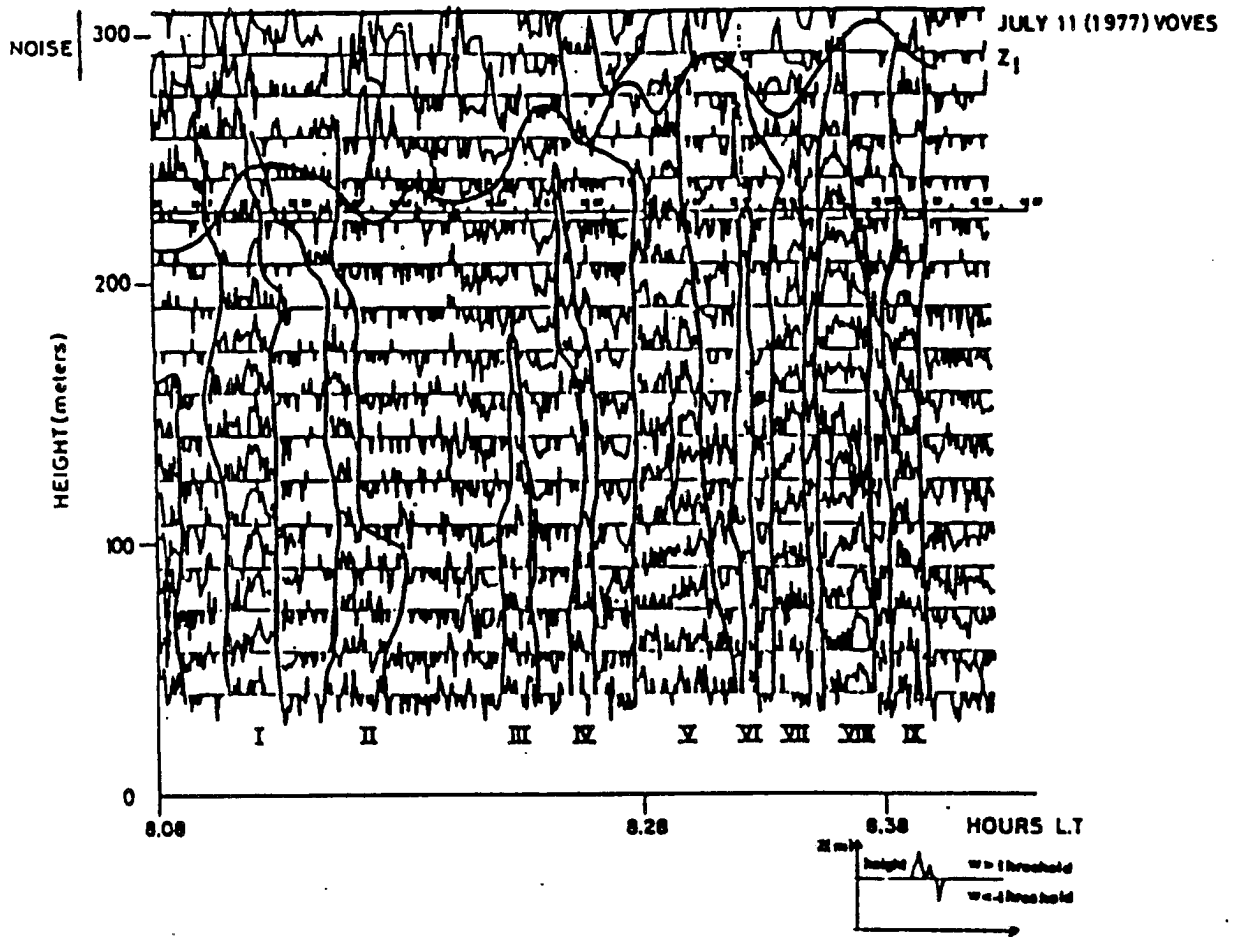


Figure 4.14. Vertical velocity plot as seen by Doppler sodar (from Taconet and Weill, 1983).

useful the lidar is in obtaining information on mean conditions very quickly; i.e., at a 10° elevation angle, the lidar remotely scanned an area of 50 square kilometers in less than a minute, providing mean information in increments of 30 m in height to altitudes as high as 1.7 km above the surface.

The mean wind removal from the Doppler lidar revealed a wealth of information on the perturbation wind fields. The location of large and small "eddy" features within a scan reveals information on the wind field's instantaneous responses to its environment, and on the instantaneous transport by the perturbation field.

The ability of the Doppler lidar to document temporal and spatial changes in the perturbation field was then investigated. Thermal scale features were traced in time, and in both horizontal and vertical planes. By combining scans, continuity in time and space was demonstrated. The technique of combining a number of scans of an area shows how powerful the Doppler lidar can be when used to document the development of wind fields.

Range limitations of the lidar preclude being used for problems that cover near synoptic-scale regions, but general studies on the 10-100 km radius scale are already done with Doppler radar, which is limited by sidelobe clutter on the 0.5-20 km scale the lidar is designed for. Additional difficulties in the lidar technique are introduced close to the scanner, where minimum range limitations of about 1.5 km prevent studies close to the trailer. Since there is no clutter or false echo region, once the minimum range is exceeded there is no difficulty in scanning along the surface, such as that experienced in radar applications. Limitations on the lidar due to the pulse length mitigate against studies of the turbulent cascade scales, limiting lidar usefulness in surface layer investigations, but incoherent lidars with short pulses designed for plume dispersion studies cover that region well.

Distributions of the perturbation fields developed in the investigations were done and demonstrate the wealth of information available using the Doppler lidar as a wind investigation tool. The demonstrated spatial information on the perturbation velocity allowed large fields to be identified in relation to their position and development. With scan rates reduced, information on features as small as 30 m azimuthally were available.

6. FUTURE WORK

This investigation dealt with verifying the Doppler lidar as a useful tool in the measurement of atmospheric boundary layer wind fields. With the demonstrated accuracy of the Doppler lidar as a wind measurement tool, the next step would be to use it to investigate specific mean and "eddy" wind fields. With a lidar coverage of at least 50 square kilometers, an area study in time and space could trace features through their development stages in the complete mesoscale area.

Investigations using the Doppler lidar to study mean wind fields should be able to provide significant understanding on boundary layer development, dynamics, and collapse. Because it provides the mean and "eddy" flow fields, the Doppler lidar should be usable to investigate the effect of changes in the wind environment from initially unperturbed fields to stressed conditions where flow is influenced by environmental conditions. The ability to scan the horizontal and then the vertical structures should allow dynamics of developing systems such as cloud convective roots to be studied. The ability to couple the identification of boundary layer features with upper level structures such as waves should provide improved understanding of the interactions between the scales of motion apparent in atmospheric phenomena, as well as documenting the time scale of the interactions.

The transportability of the Doppler lidar allows it to be used to provide information in diverse regions on changes in wind fields and effect of terrain on wind fields. A time sequence of before and after, perturbed and unperturbed wind fields in the real atmosphere can be provided by Doppler lidar, allowing analysis of natural and anthropogenic effects on an actual wind field. By making available both mean and "eddy" flow patterns, the Doppler lidar can be used to identify and study changes as they occur in a wind field, and thus improve understanding of the reasons for changes.

With the scan techniques developed in this study, the lidar can be used to study atmospheric features over a large range of scale sizes. Information from remotely sensed data for small-scale atmospheric data should provide better information on the growth, development, and dissipation of mesoscale and smaller atmospheric phenomena. The nonintrusive nature of the lidar eliminates many of the limitations of in situ instruments, and when the lidar is used in com-

combination with more traditional sensors of temperature and humidity, it can provide better specification of mesoscale events.

7. REFERENCES

- Atlas, D., 1959: Meteorological Angel Echoes, J. Appl. Meteorol., Vol. 16, pp. 6-11.
- Browning, K.A., and R. Wexler, 1968: The Determination of Kinematic Properties of a Wind Field Using Doppler Radar, J. Appl. Meteorol., Vol. 7, pp. 105-113.
- Browning, K.A., J.R. Starr, and A.J. Whyman, 1972: Measurements of Air Motions in Regions of Clear Air Turbulence Using High Power Doppler Radar, Nature, Vol. 239, pp. 267-269.
- Cermak, J.E. and J.D. Horn, 1968: Tower Shadow Effect, J. Geophys. Res., Vol. 73, pp. 1869-1876.
- Coulman, C.E., 1978: Boundary Layer Evolution and Nocturnal Inversion Dispersal, Part I, Boundary Layer Meteorol., Vol. 14, pp. 471-491.
- Ditchburn, R.W., 1953: Ultraviolet Radiation Absorption Cross sections, (in Boyd, R.L.F.; Seaton, M.J., and Massey, H.S.W., Rocket Exploration of the Upper Atmosphere) pp. 313-326.
- Dobson, E.B., 1970: Doppler Radar Measurements of Mean Wind Variations in the Clear Atmosphere, Proc., 14th Radar Meteorological Conference, pp. 69-72.
- Durst, F., A. Melling, and J.H. Whitelaw, 1976: Principles and Practice of Laser-Doppler Anemometry, Academic Press, New York, 405 pp.
- Eberhard, W., 1979: Design and Performance of an Experimental Dual Frequency Doppler Lidar for Remote Measurement of Wind Velocity, Ph.D. Thesis, U. of Arizona, 203 pp.
- Eversole, R.A., 1978: Spectral Characteristics of Boundary Layer Over Irregular Terrain, CSU Atmos. Sci. Paper 314, 115 pp.
- Gage, K.S., and B.B. Balsley, 1978: Doppler Radar Probing of the Clear Atmosphere, Bull. Am. Meteorol. Soc., Vol. 59, pp. 1074-1093.
- Gossard, E.E., ed., 1982: Boulder Upslope Cloud Experiment, NOAA Special Report, 237 pp.

- Gossard, E.E., and R.G. Strauch, 1984: Radar Observations of Clear Air and Clouds, Elsevier Science Publishing, New York, 280pp.
- Hall, F.F., J.G. Edinger and W.D. Neff, 1975: Convective Plumes in the Planetary Boundary Layer, Investigated with an Acoustic Echo Sounder, J. Appl. Meteorol., Vol. 14, pp. 513-523.
- Hardesty, R.M., 1984: Measurement of Range-Resolved Water Vapor Concentration by Coherent CO₂ Differential Absorption Lidar, NOAA-TM-ERL-WPL-118, 263 pp.
- Hardy, K.R., and H. Ottersten, 1969: Radar investigations of Convective Patterns in the Clear Atmosphere, J. Atmos. Sci., Vol. 26, pp. 666-672.
- Hinkley, E.D., ed., 1976: Laser Monitoring Of The Atmosphere, Springer-Verlag, New York, 380 pp.
- Hooke, W.H., ed., 1979: Project Phoenix, NOAA/NCAR BAO Report 1, 281 pp.
- Hulbert, E.O., 1937: Observations of a Searchlight Beam to an Altitude of 28 Kilometers, J. Opt. Soc. Am., 27, pp. 377-382.
- James, P.K., 1980: A Review of Radar Observations of the Troposphere in Clear Air Conditions, Radio Science, Vol. 15, pp. 151-175.
- Jenkins, F.A., and H.E. White, 1937: Fundamentals of Physical Optics, McGraw Hill, New York, 453 pp.
- Kaimal, J.C., 1980: BAO sensors for wind, temperature and humidity profiling. Chapter 1 in The Boulder Low-Level Intercomparison Experiment - Preprint of WMO Report, J.C. Kaimal et al., Eds., NOAA/NCAR Boulder Atmospheric Observatory Report No. 2, pp. 1-6.
- Kaimal, J.C., and J. Gaynor, 1983: The Boulder Atmospheric Observatory, J. Appl. Meteorol., Vol. 22, pp. 863-80.
- Kaimal, J.C., and D. Wolfe, 1977: BAO Site, Tower Instrumentation, and Phoenix Operations, in Project Phoenix, NOAA/NCAR BAO Report 1, W.H. Hooke, ed., pp. 16-32.
- Kaimal, J.C., J.C. Wyngaard, Y. Izumi, and O.R. Cote, 1972: Spectral Characteristics of Surface-Layer Turbulence, Quart. J. Roy. Meteorol. Soc., Vol. 98, pp. 563-589.

- Kaimal, J.C., J.C. Wyngaard, D.A. Haugen, O.R. Cote, and Y. Izumi, 1976:
Turbulence Structure in the Convective Boundary Layer, J. Atmos. Sci., Vol. 33, pp. 2152-2160.
- Keeler, R., 1980: Adaptive Frequency Estimation and New Convergence Properties for the Least Mean Square Algorithm, NOAA-TM-ERL-WPL-49, 171 pp.
- Lawrence, T.R., R.M. Hardesty, M.J. Post, R.A. Richter, and R.M. Huffaker, 1983: Performance Characteristics of the NOAA Pulsed Doppler Lidar, and its Applications to Atmospheric Measurements., Prepr., 5th Symp. on Meteorological Observations and Instrumentation, Apr. 11-15, 1983, Toronto, Canada, American Meteorological Society, Boston, pp. 481-487.
- Lee, R.W., and K.A. Lee, 1981: A Poly-Pulse-Pair Signal Processor for Coherent Doppler Lidar, Proc., Conf. on Coherent Laser Radar for Atmos Sensing, July 15-17 1980, WA2-1.
- Lenschow, D.H., 1970: Airplane Measurements of Planetary Boundary Layer Structure, J. Appl. Meteorol., Vol. 9, pp. 874-884.
- Lenschow D.H., and P.L. Stephens, 1980: Role of Thermals in the Convective Boundary Layer, Boundary Layer Meteorol., Vol. 19, pp. 509-532.
- Ligda, M.G.H., 1963: Proc., 1st Conf. on Laser Tech., USN (ONR), pp. 63-72.
- Manton, M.J., 1977: On Dry Penetrative Convection, Boundary Layer Meteorol., Vol. 14, pp. 301-322.
- McCormack, P., 1975: The Use of Lidar for Atmospheric Measurements, Remote Sensing, T. Nejat Veziuglu, ed., Hemisphere Publishing, Washington, DC, pp. 113-128.
- Metcalf, J.I., and D. Atlas, 1973: Microscale Ordered Motions and Atmospheric Structure Associated with Thin Echo Layers in Stable Stratified Zones, Boundary Layer Meteorol., Vol. 4, pp. 7-35.
- Middleton, W.E.K., and A.F. Spilhaus, 1953: Meteorological Instruments, Univ. Toronto Press, 208 pp.

- Miller, K.S., and M.C. Rochwargner, 1972: A Covariance Approach to Spectral Moment Processing, IEEE Trans. Inf. Theory, Vol. IT-18, pp. 588-596.
- Mitsuta, Y., 1971: Sonic Anemometer-Thermometer for Atmospheric Turbulence Measurement, Paper presented at Symposium on Flow, Its Measurement and Control in Science and Industry, 9-14 May 1971, Pittsburgh.
- Owens, J.C., 1969: Optical Doppler Measurement of Microscale Wind Velocity, Proc. IEEE, 58, pp. 322-326.
- Panofsky, H.A., and A.A. Townsend, 1964: Change of Terrain Roughness and the Wind Profile, Quart. J. Roy. Meteorol. Soc., Vol. 90, pp. 147-155.
- Panofsky, H.A., and J.A. Dutton, 1984: Atmospheric Turbulence, John Wiley and Sons, New York, New York, 395 pp.
- Patel, J., and L. Peach, 1976: Estimation of the Average Frequency of a Random Process Gated at a Sub-Nyquist Rate, Proc., 17th Conf. on Radar Meteorology, October 26-29, 1976, Amer. Meteorol. Soc., Boston, pp. 36-41.
- Post, M.J., 1985: Atmospheric infrared backscattering profiles: Interpretation of statistical and temporal properties. (Dissertation Univ. of Arizona). Also published as NOAA TM ERL WPL - 122, 105 pp.
- Post, M.J., R.L. Schwiesow, R.E. Cupp, D.A. Haugen and J.T. Newman, 1978: Temporal and Spatial Frequency Spectra for Atmospheric Aerosols, J. Appl. Meteorol., Vol. 17, pp. 1179-1181.
- Post, M.J., R.A. Richter, R.M. Hardesty, T.R. Lawrence, and F.F. Hall, 1981: NOAA's Pulsed, Coherent, IR Doppler Lidar - Characteristics and Data. Proc., SPIE Physics and Technology of Coherent IR Radar, San Diego, CA, August 24-28, 1981, Vol. 300, pp. 60-65.
- Ridenour, L.N., 1947: Radar System Engineering, MIT Radiation Series, Vol. 1, McGraw Hill Book Co, New York, 263 pp.
- Sirmans, D., and B. Baumgarner, 1977: Numerical Comparison of Five Mean Frequency Estimators, J. Appl. Meteorol., Vol. 14, pp. 991-1003.
- Taconet, O., A. Weill, 1983: Vertical velocity field in the convective boundary layer as observed with an acoustic Doppler sodar. Boundary Layer Meteorol.

- Vol. 23, pp. 133-151.
- Tennekes, H., and J.L. Lumley, 1972: A First Course in Turbulence, MIT Press, Cambridge, 300 pp.
- Ting, C.L., and D.R. Hay, 1977: Thermal Plumes and Turbulence Spectra in the Atmospheric Boundary Layer, Boundary Layer Meteorol., Vol. 11, pp. 243-263.
- Warner J., and J.W. Telford, 1963: Some Patterns of Convection in the Lower Atmosphere, J. Atmos. Sci., Vol. 20, pp. 313-318.
- Warner J., and J.W. Telford, 1967: Convection Below Cloud Base, J. Atmos. Sci., Vol. 24, pp. 374-382.
- Watrasiewicz, B.M. and M.J. Rudd, 1976: Laser Doppler Measurements, Butterworths, Boston, 160 pp.
- Wolfe, D.E., 1985: Early Morning Evolution of the Convective Boundary Layer at the Boulder Atmospheric Observatory, CSU Masters Thesis, Dept. Atmos. Sci., 161 pp.
- Wood, T., and R.A. Brown, 1983: Single Doppler velocity signatures: An atlas of patterns in clear air/widespread precipitation and convective storms. NOAA TM ERL NSSL-95.
- Yeh, Y., and H.Z. Cummings, 1964: Localized Fluid Flow Measurements with an He-Ne Laser Spectrometer, Appl. Phy. Letters., 4, pp. 176-178.
- Zrnic, D., 1977: Spectral Moment Estimates from Correlated Pulse Pairs, IEEE Trans. Aerosp. and Electron. Syst., Vol. AES 13-4, pp. 344-354.
- Zrnic, D., 1979: Estimation of Spectral Moments for Weather Echoes, IEEE Transactions on Geoscience Electronics, Vol. GE-17, pp. 113-128.

APPENDIX A

TOWER DATA

A.1. Data Archiving

Data recorded at the BAO tower are kept in archival format at the NOAA Wave Propagation Laboratory (WPL) in Boulder. Time periods are available in blocks of 20 minutes. Listings of available dates and times can be made for periods of interest. These data are archived in:

- (1) Twenty minute averages, moment or "M" data (Fig. A.1),
- (2) samples of the actual raw data, one sample from every 100 points, "G" data, (Fig. A.2),
- (3) data that are averaged from the 10 samples per second to one sample every 10 seconds, coded "A" data (Fig. A.3).

Additional data are available when special arrangements are made to record the raw (10 Hz and 1 Hz) data.

A.2. Sonic anemometer processing

The "A" data for the sonics were used in the sensor comparison. The time series for both the "A" and the "G" data for the possible comparison times were plotted (Fig. A.4). Vertical profiles of the 'M' data series for all tower levels were run for the periods under investigation (Fig. A.5).

The quality of the sonics "A" data was investigated before using a data series for the comparison. Two separate problems which could occur with the sonics data were investigated. The sonics "A" data represent data created from combining and transforming the sonic path data from the acoustic arrays. In addition to transforming the data, the data are averaged from the 10-Hz data to 0.1-Hz data. In that this data reduction represents a substantial possible loss of information, the sonics information was investigated to determine the effect of the possible losses on the comparison.

The transformation effect was investigated by looking at a raw data series and performing the same processing on the series as is done by the BAO processing. Since a raw data series was not available for the comparison period, a different time was used. Figure A.6 gives a raw along and across boom 10-Hz

BOULDER ATMOSPHERIC OBSERVATORY DATA SUMMARY

AVERAGING PERIOD- 20.00 MIN

19 MAR 62 1920 MET

Z(M)	SONIC					PROPANE		T	TD	L
	VMS	VSDU	U	VM	AZ	SPD	DIR			
10	6.49	-8.67	0.91	10.83	323.	10.80	142.	12.90	-4.67	-83.41
22	6.74	-8.26	0.22	10.66	321.	11.93	237.	12.11	*****	*****
50	7.34	-10.99	0.34	12.97	324.	12.47	91.	11.47	*****	-48.33
100	6.82	-9.80	-0.03	11.94	325.	12.16	10.	10.93	-4.83	*****
150	6.43	-8.84	0.10	10.93	324.	12.68	109.	10.32	-5.39	*****
200	2.87	-3.09	-0.13	3.85	321.	12.13	23	10.02	-3.59	*****
250	3.63	-4.34	-0.23	3.67	320.	11.73	353.	9.72	-6.04	*****
300	3.34	-2.81	-0.01	4.36	310.	12.48	328.	9.19	-5.80	*****

Z(M)	UU	VV	WW	TT	UV	VW	UT	VT	UW	WT
10	12.1377	2.2868	0.4991	0.4473	1.1190	-0.0340	-0.2930	-0.2374	-0.2699	0.1379
22	50.3464	3.2035	0.3206	*****	7.7814	0.0861	*****	*****	0.4178	*****
50	13.8073	1.4874	0.5043	0.1008	1.3780	-0.0678	-0.0748	-0.0485	-0.1647	0.1217
100	42.2313	6.1763	0.3732	0.1130	3.7737	-0.0131	0.2971	-0.1222	0.2370	0.1647
150	61.1631	2.8064	0.3371	*****	10.3052	0.0783	*****	*****	1.0002	*****
200	*****	9.8917	0.4398	0.0821	43.0424	0.0933	0.6731	0.0917	0.3794	0.0104
250	*****	9.3339	0.3678	0.0933	43.7949	0.0378	0.9084	0.1663	0.1148	0.0018
300	*****	8.8648	0.4226	0.0088	43.8148	0.0338	0.4444	0.0983	0.2304	-0.0843

Z(M)	MAINTENANCE DATA		
	US	VS	TP
10	10.64	2.03	12.67
22	10.38	2.44	*****
50	12.77	2.19	8.76
100	11.80	1.83	6.91
150	10.77	1.90	*****
200	9.84	0.33	8.58
250	8.50	1.37	11.83
300	3.99	1.77	6.16

OPTICAL TRIANGLE				PRESSURE STAMP. DEV. (MICROBARS)				
V (M/SEC)	AZ(DEC)	CONV(1/SEC)	LOG10 CH-SOR	STN 1	STN 2	STN 3	STN 4	STN 5
7.89	390.	-0.02640	-13.40688	*****	*****	*****	*****	*****

PRESSURE(MB)
819.37

SOLAR RAD(LY/MIN)
0.34

Figure A.1. Sample of BAO "M" data sheet.

KIND 0

DATE	TIME	1	2	3	4	5	6	7	8
840129.	1200	0.49487	0.28091	-0.40327	-0.23363	-0.71415	-1.0363	-1.4861	33.462
		0.36914	0.87514	-0.32717	-1.76188E-02	-0.49457	-1.1100	-1.3447	33.200
		-6.55008E-02	-2.25491E-02	-0.77452	-0.36844	-0.33198	-1.1824	-1.8777	33.249
		0.28445	2.87894E-02	1.75968E-02	-0.26915	-0.74604	-0.81939	-1.8738	33.559
		0.10054	0.28811	-0.16049	-0.30520	-0.37925	-1.0074	-1.7434	33.737
	0.47681	0.83247	0.21020	-0.31647	-0.29480	-1.6759	-2.1341	-1.2318	
	1201	0.10644	0.85657	0.55835	4.49764E-02	-0.32833	-1.7643	-1.8004	33.127
		0.12528	0.55398	0.33443	-0.31864	-0.15398	-0.88824	-1.6990	-1.5407
		-0.24412	0.42812	0.84565	2.90608E-03	-0.28337	-1.2104	-1.8298	-1.6426
		0.31089	0.57922	4.92414E-02	-0.59278	-0.34443	-1.2244	-1.4744	-1.9752
0.24472		0.94447	0.39823	-0.39388	-0.29013	-1.0202	-1.6744	-2.5117	
-0.19690	0.36975	0.22272	-0.21073	-0.37877	-1.1834	-1.5484	-2.4134		

Figure A.2. Sample of BAO "G" data list.

KIND A

DATE	TIME	1	2	3	4	5	6	7	8
820308.	1320	-2.2507	-3.0227	-3.1289	-2.9328	-3.5088	-1.00000E+38	-3.2974	-4.3881
		-1.8973	-2.7103	-3.0346	-2.8369	-3.2385	-1.00000E+38	-2.2393	-3.6045
		-1.3781	-2.1799	-3.0503	-3.3623	-2.5612	-1.00000E+38	-1.2913	-2.7172
		-1.2983	-2.2092	-2.8267	-3.4600	-1.4209	-1.00000E+38	-1.2197	-2.1135
		-0.89829	-2.1493	-2.5303	-2.3663	-1.4571	-1.00000E+38	-1.2439	-1.7637
	-0.60087	-2.2483	-2.8603	-2.4818	-1.1900	-1.00000E+38	-1.0387	-2.0809	
	1321	-0.67379	-2.3274	-2.3983	-2.6418	-1.3334	-1.00000E+38	-0.78630	-1.6112
		-1.4027	-2.6739	-2.2663	-1.6694	-1.1349	-1.00000E+38	-0.77952	-2.3099
		-1.9852	-1.7396	-2.2228	-0.90334	-0.96260	-1.00000E+38	-0.54069	-3.0728
		-0.56304	-2.1187	-1.9849	-1.2612	-1.1179	-1.00000E+38	-1.2553	-3.9293
-0.66914		-1.8089	-1.9639	-2.0043	-0.84357	-1.00000E+38	-1.6818	-2.6432	
-0.55613	-2.2567	-2.4042	-2.3101	-0.92438	-1.00000E+38	-1.0561	-1.3547		

Figure A.3. Sample of BAO "A" data list.

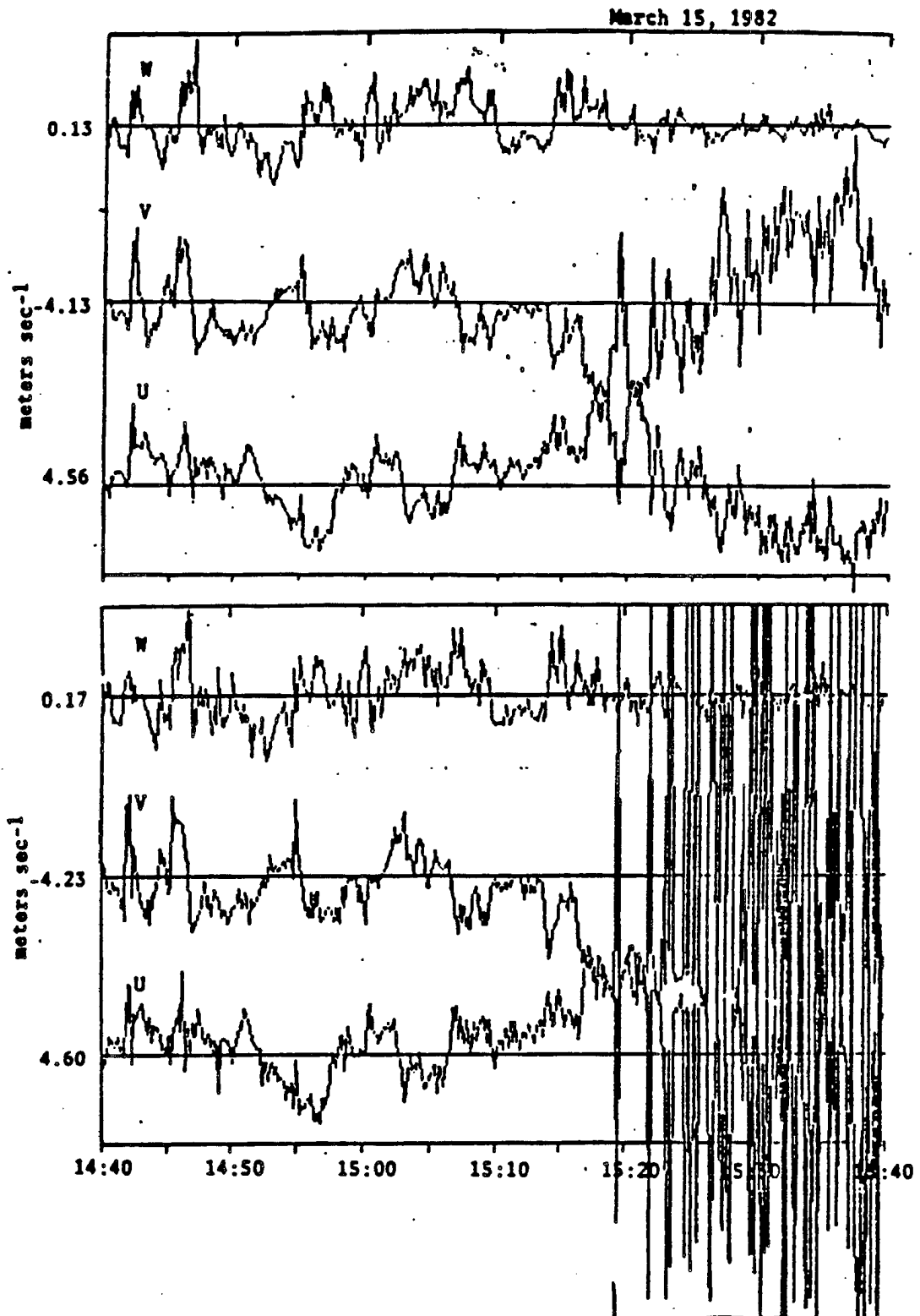


Figure A.4. Sonic data from the 300 meter level booms on the BAO Tower.
 a) Upper plot is "A" data. b) Lower plot is "G" data.

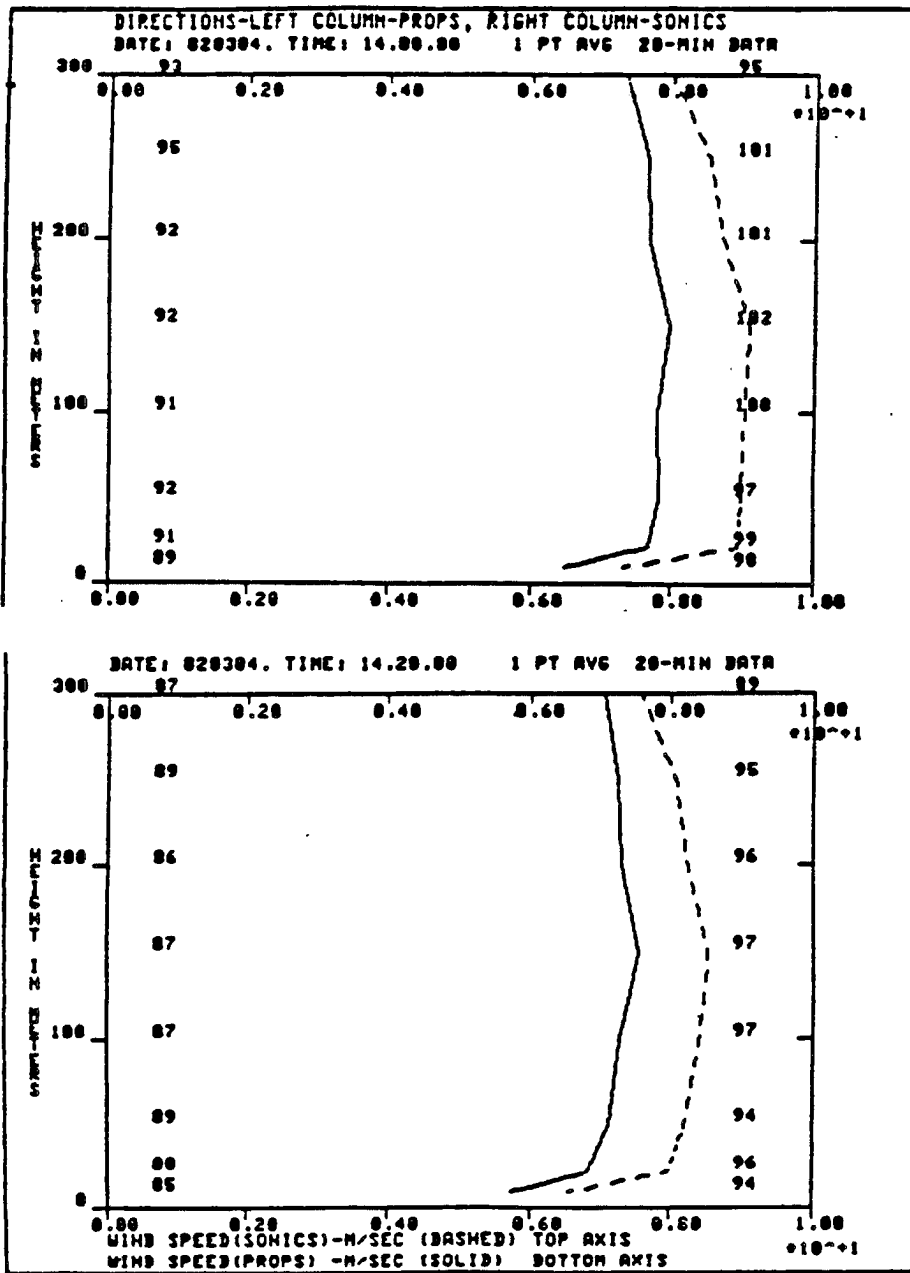


Figure A.5. Examples of wind profiles from tower sensors during BUCOE.
 a) Upper plot is 14:00-14:20 MST. b) Lower plot is 14:20-14:40 MST.

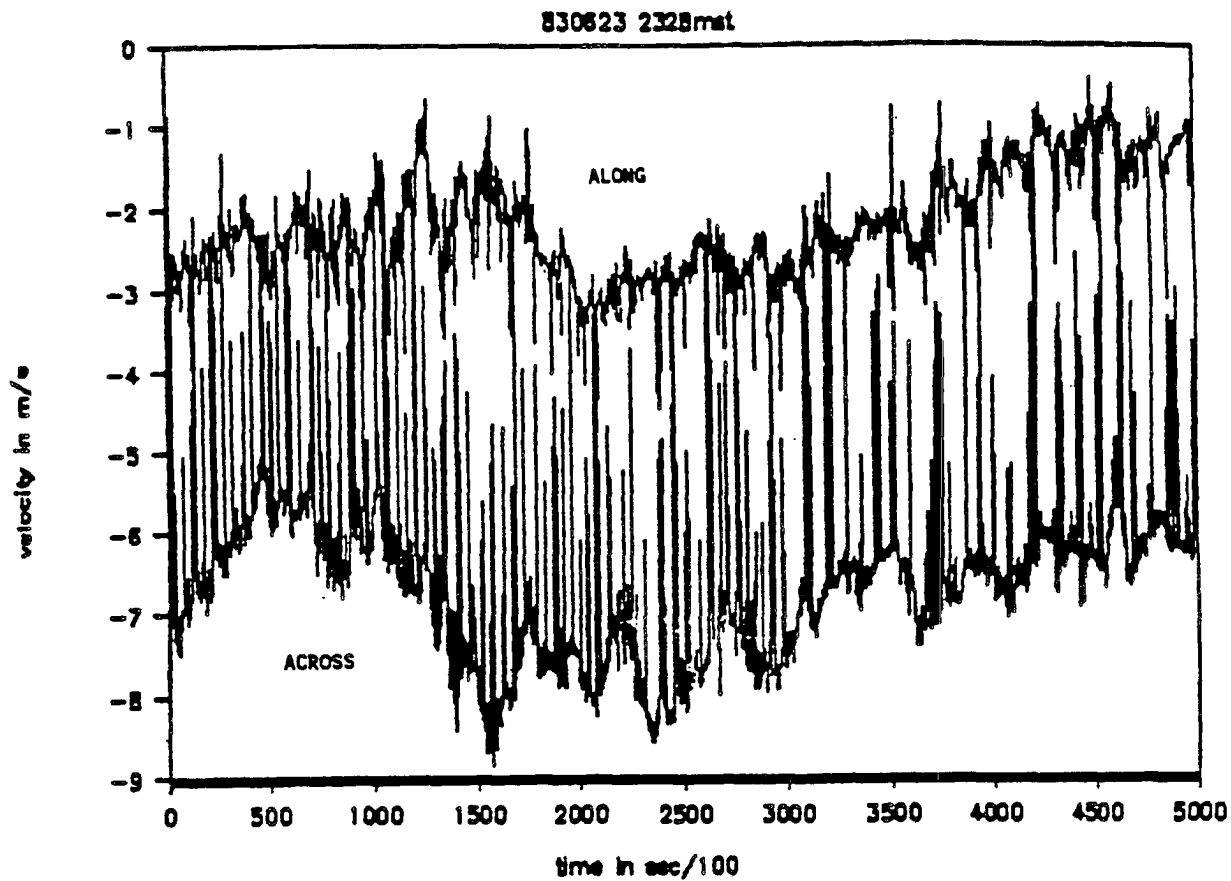


Figure A.6. Two minute data series of raw sonic data from BAO tower. a) Upper curve is the along boom component. b) Lower curve is the across boom component. Note the poor behavior in the along boom component signified by the numerous spikes of greater than 3 m/s.

data series. The important features in this plot are the 'spikes' or obvious discontinuities in the data. Figure A.7 shows the effect of transforming the data series. In this plot, the 'spikes' are reflected in the two new "u" and "v" components but are mixed into both of the new components. The next step in processing is to reduce the data rate to 0.1 Hz. Sequences of raw and transformed "G" data (Fig. A.8) and a transformed "A" data sequence (Fig. A.9) was created. The transformed, averaged data in Fig. A.9 shows small departures from the mean but not outside the range of standard atmospheric variability. The "G" data series in Fig. A.8 does a better job of indicating possible data problems, but the magnitude of the problem is masked.

The best indication of data series contaminated by "spikes" is contained in the raw data, but since the raw series were not available for the comparison, a combined inspection of both the "A" and the "G" data series was done to identify inappropriate data series. Figure A.4 gives a set of "A" and "G" time series for a period that was investigated for possible use in the comparison. The "G" data were plotted to take advantage of the unaveraged data's better resolution of the presence of possible data problems. The highlighted areas in the "G" data are indicative of data problems. Data series that demonstrated the same type of deviations were deleted from the comparison.

Since the data are retained in component form throughout the averaging technique, it should be noted that the resultant wind magnitude and direction represent what can be thought of as a "transport" or net mean wind. The calculation represents a record of the net movement of air over the period of the time series. Some cancellation of wind components, especially in light wind cases, will occur.

A.3. Propeller-vane anemometer processing

The "A" data wind speed and direction for the prop data during the time periods under investigation were plotted in 1-h time divisions (Fig. A.10). Data were checked for instrumental problems and it was determined that no obvious exclusions were necessary. The prop data are reduced to an average magnitude and direction for each 10-s period at the tower site. Further averaging into the comparison time periods was done initially by using BAO lab programs. These programs take the "A" data speed and direction information,

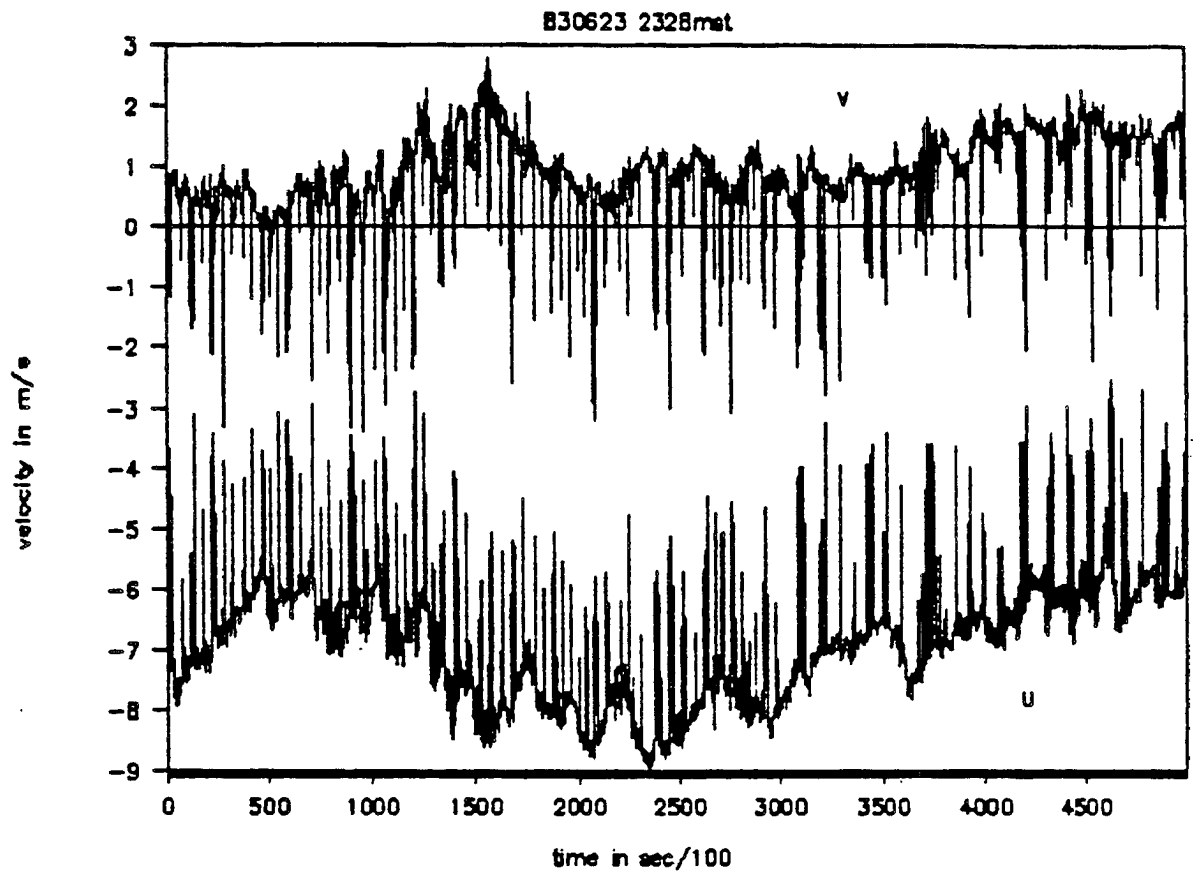
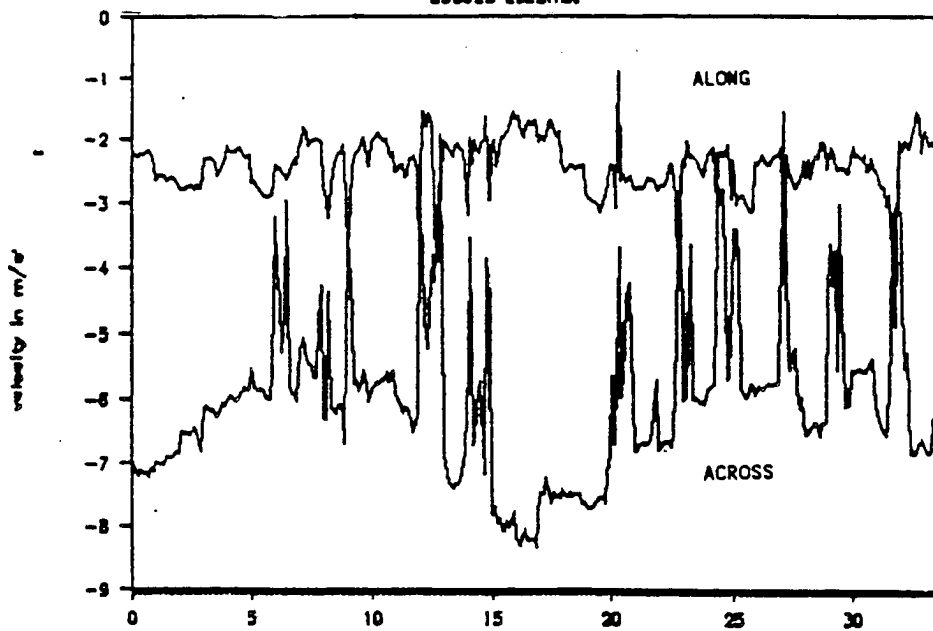


Figure A.7. Translated sonic component data from BAO tower. a) Upper curve is the north or "V" component. b) Lower curve is the east or "U" component. Note the spikes from original data sequency are distributed in both components.

Grab sample of Raw Data

830623 2328mst



Grab U V Components from Raw Components

830623 2328mst

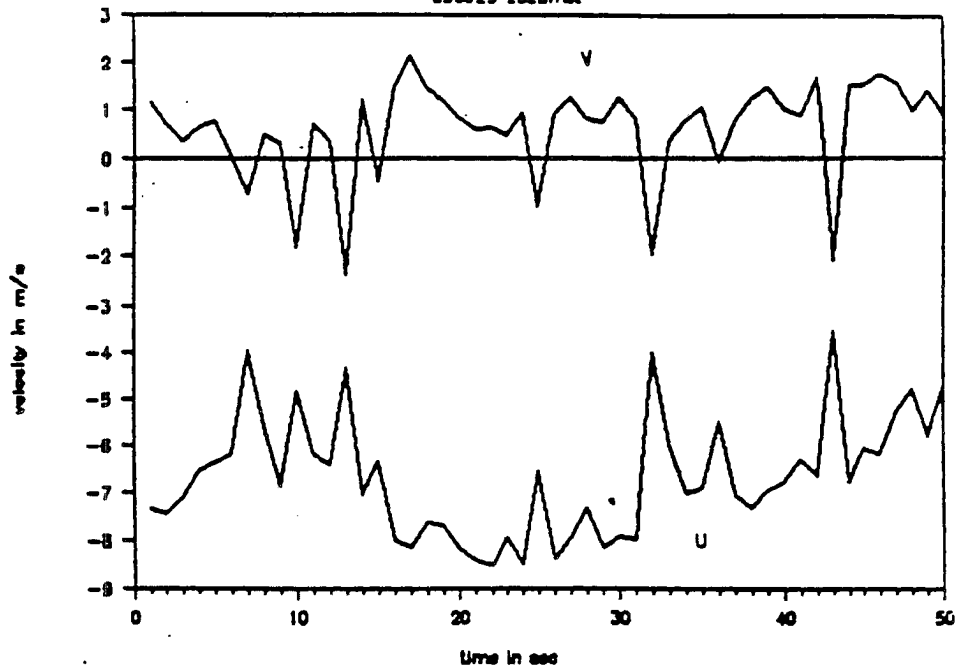


Figure A.8. "G" data sequences from tower data. a) Along/across boom sonic components. b) "U"/"V" derived components.

Avg U V Components from Raw Components

830623 2328mat

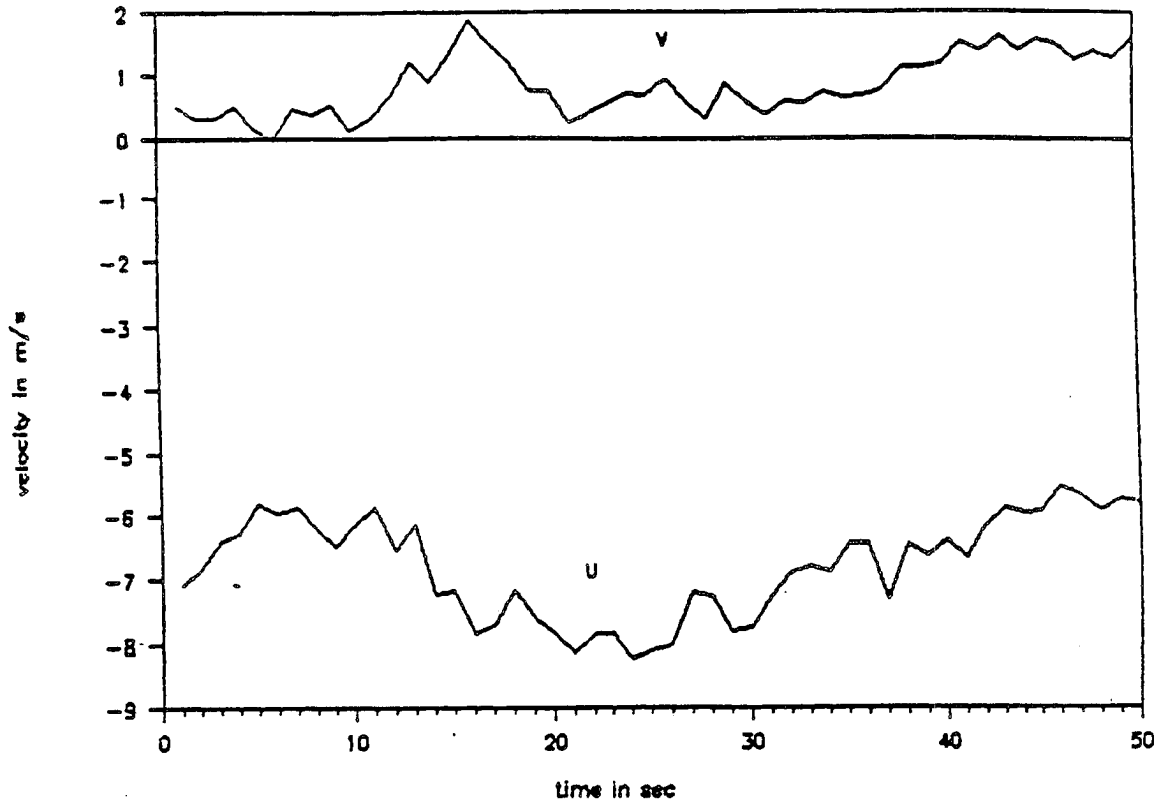


Figure A.9. Average, or "A" data sequence derived from sonic along/across component data.

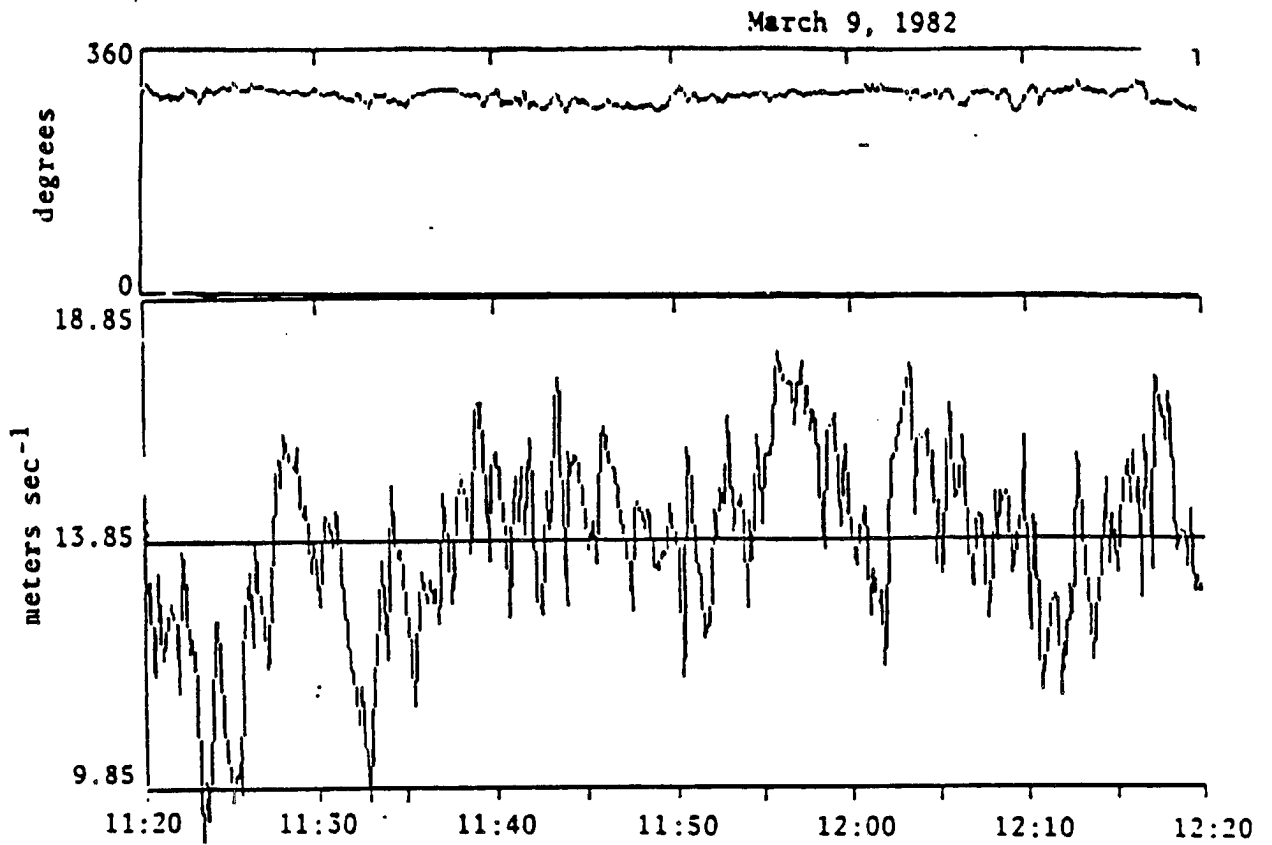


Figure A.10. Sample prop data series from the 300 meter level boom on the BAO tower. a) Upper plot - wind direction. b) Lower plot - wind speed.

calculate the u and v components, average the components for the period requested, and then recalculates the speed and magnitude. Since the BAO lab averaging method is inconsistent with the on-site averaging, the first half of the data were reprocessed using averages of wind speed and direction for the periods previously defined. The difference in the averaging techniques is important only for the speed calculation, since division (used for the tangent function in the direction calculation) is linear. The difference is represented mathematically as

$$(\Sigma u^2 + \Sigma v^2)^{1/2} \text{ vs. } \Sigma(u^2 + v^2)^{1/2} .$$

This procedure for the wind produces a mean "average wind speed." Differences were not large between the two techniques, but in isolated cases the technique of averaging the magnitude rather than components of the wind speed better matched the VAD profiles. Table A.1 gives a group of prop wind speeds for a sequence of recalculated cases. Both the net winds and the average winds are expected to differ in some cases from the results of sonics averaging, owing to the response differences in the instruments and the cancellation inherent in the component averaging of the sonics.

Table A.1. Component averages versus speed averages for selected propeller vane examples during lidar/tower comparison

Date	Time (MDT)	Component	Speed
04-Mar-82	14:23:59	6.35	6.34
05-Mar-82	12:03:56	1.60	0.85
08-Mar-82	13:59:29	4.59	4.39
09-Mar-82	11:43:31	14.65	14.54
10-Mar-82	15:44:20	5.93	5.17
12-Mar-82	11:01:11	16.03	16.00
15-Mar-82	15:14:58	9.55	9.51
17-Mar-82	12:05:20	2.75	1.52
19-Mar-82	10:23:16	17.80	17.76
24-Mar-82	14:24:22	9.70	6.03
24-Mar-82	14:27:47	14.07	10.57
24-Mar-82	15:17:11	21.15	21.12
24-Mar-82	15:31:01	20.70	20.68
24-Mar-82	15:33:43	20.22	20.21
24-Mar-82	16:09:29	17.56	17.55
24-Mar-82	16:52:20	13.18	13.17
24-Mar-82	17:07:22	10.59	10.53
24-Mar-82	17:58:58	9.58	9.57
31-Mar-82	12:27:39	3.90	3.69
31-Mar-82	12:35:38	3.71	3.37
05-Apr-82	15:46:15	6.01	5.83
20-Apr-82	09:19:36	7.16	7.13
23-Apr-82	11:18:12	3.62	3.45
23-Apr-82	11:23:46	3.84	3.71

APPENDIX B

THE VELOCITY-AZIMUTH DISPLAY TECHNIQUE

The Velocity-Azimuth Display (VAD) technique for determining winds from remotely sensed data was first described and used in connection with radar studies. Much of the following summary of the methodology was taken from Browning and Wexler (1968). Differences will exist in the application of the VAD technique to lidar because of the differing targets and beamwidth of the lidar versus the radar to which the technique was first applied.

The VAD technique is a scanning technique in which the beam is pointed at a given angle from the zenith and the scanner is then rotated about the vertical axis. (Fig. B.1). The returning signal includes (1) a horizontal velocity return with a sine function related to the azimuth angle (the angle in the plane of the rotation) and the mean wind direction, and (2) a vertical velocity return dependent on the zenith angle. This radial velocity can be separated mathematically into the vertical and horizontal components of the wind field. There are some restrictions on the information that can be derived from the relationship, as well as some conditions during which the technique will not give results appropriate to the wind field being studied.

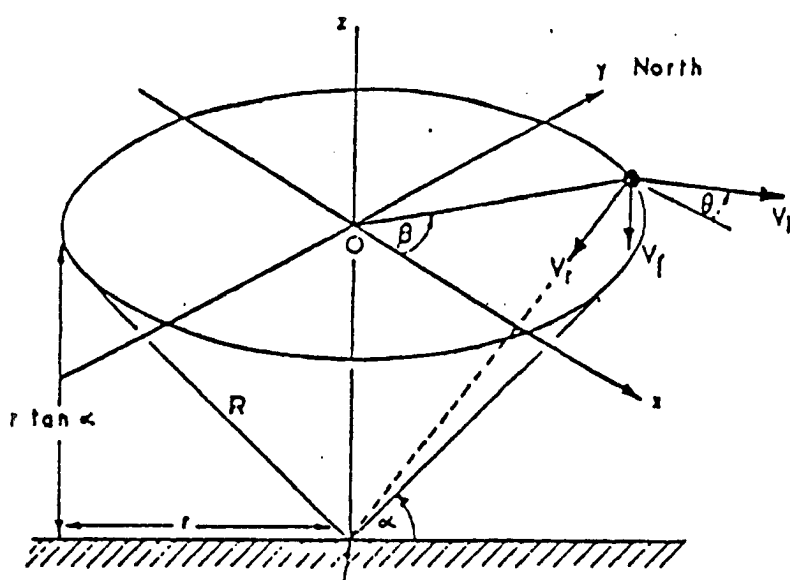


Figure B.1. Example of conic section explored when using a VAD scan technique (from Browning and Wexler, 1968).

B.1 Characteristics of a VAD Scan

The VAD sinusoid contains information representing a variety of characteristic wind fields. The standard derivations apply to the wind field that is constrained by horizontal homogeneity, mean vertical velocities, and linear changes in the field. Other characteristic flows can be analyzed with a standard VAD technique. Figure B.2 gives three fields that were developed by Browning and Wexler (1968). Wood and Brown (1983) also analyzed and published a number of solved wind field cases for the VAD technique.

The VAD technique solves the mean flow characteristics of given wind fields. Once the flow is identified, significant non-mean characteristic flows can be analyzed. Examples of cases that can be investigated include winds that are not horizontally homogeneous or whose variances from the mean represent physically significant transport terms. Measures of convergence, divergence, and deformation fields with turbulent statistics can ideally be determined from intensive harmonic analysis of the return (Gossard and Strauch, 1983). Identification of specific transport regions on the scale that the scan covers can be determined by identification and removal of advective transport mechanism terms.

B.2 Wind Velocity Derivation

Given the radial velocity positive toward the lidar and vertical velocity positive downward, the component wind velocity field can be derived as follows:

$$V_r = - V_h(\cos(\beta-\alpha)) \sin\theta + V_v \cos\theta ,$$

where V_r = radial wind velocity,
 V_h = horizontal wind velocity component,
 β = the azimuth angle taken clockwise through the scanning circle, north taken as zero degrees,
 α = the angle from north the mean wind direction makes,
 θ = the angle from zenith the scanner is positioned.

Figure B.1 gives a schematic of the angles as used in the above equation.

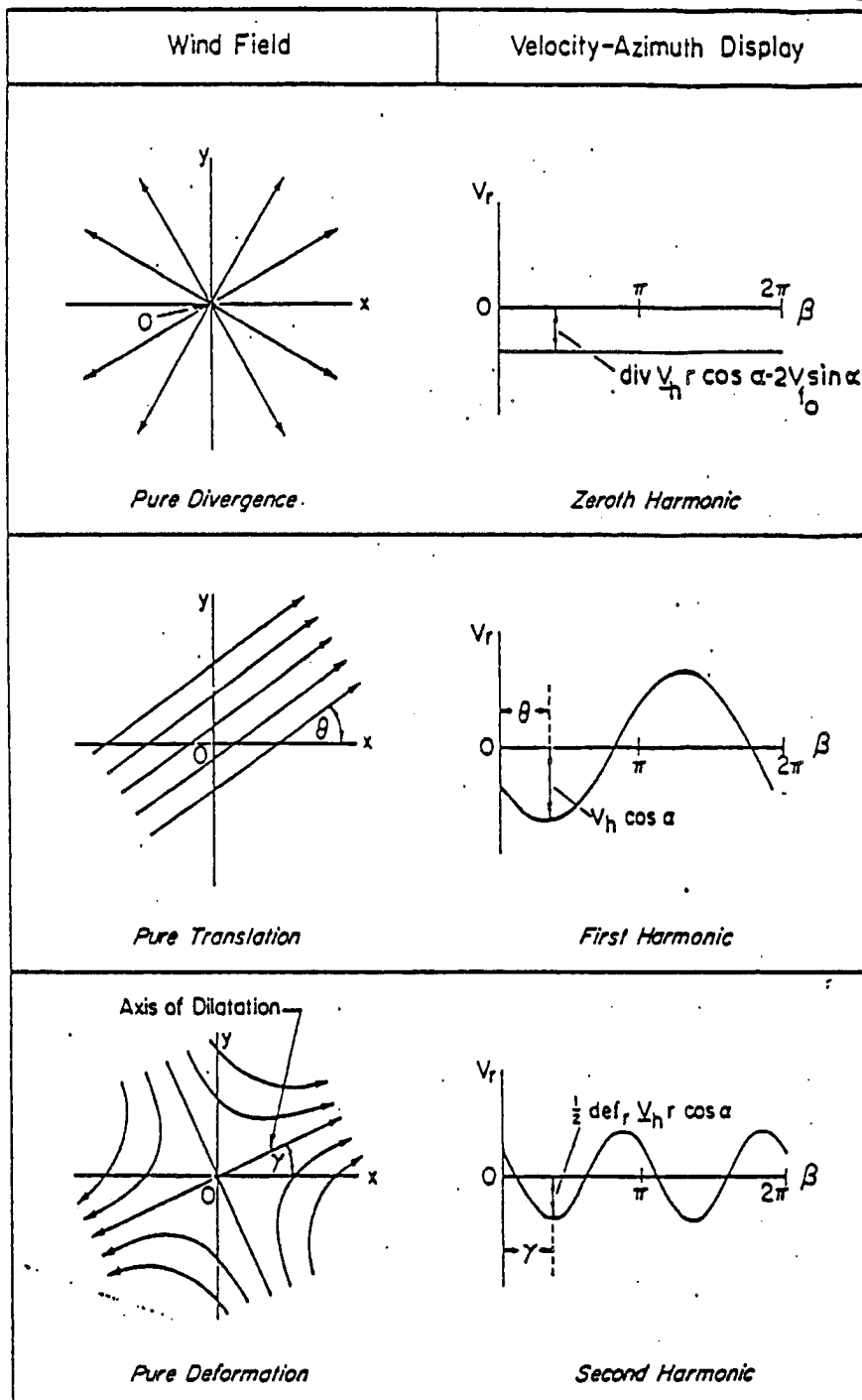


Figure B.2. Sample wind fields and their reflection as seen on a VAD (from Browning and Wexler, 1968).

APPENDIX C

VELOCITY-AZIMUTH TECHNIQUE EQUATION DERIVATION

For horizontal homogeneous flow

$$V_r = -V_h(\beta) \cos\theta \cos(\beta - \beta_0) + W(\beta) \sin\theta$$

$$= V_x(\beta) \cos\beta \cos\theta - V_y(\beta) \cos\theta \sin\beta + W(\beta) \sin\theta \quad \text{let } \beta_0 = 0$$

In Cartesian coordinates let

$$x = r \cos\beta \quad \text{and} \quad y = r \sin\beta \quad \text{and} \quad \text{express } V_x \text{ and } V_y$$

as center values
 V_{x0} and V_{y0}
 and deviations along
 the path

so

$$V_x = V_{x0} + \frac{\partial V_x}{\partial x} x + \frac{\partial V_x}{\partial y} y$$

$$V_y = V_{y0} + \frac{\partial V_y}{\partial x} x + \frac{\partial V_y}{\partial y} y$$

expanding

$$V_r = - \left[V_{x0} + \frac{\partial V_x}{\partial x} x + \frac{\partial V_x}{\partial y} y \right] \cos\beta \cos\theta \quad \begin{matrix} r \cos\beta = x \\ r \sin\beta = y \end{matrix}$$

$$- \left[V_{y0} + \frac{\partial V_y}{\partial x} x + \frac{\partial V_y}{\partial y} y \right] \cos\theta \sin\beta + W(\beta) \sin\theta$$

$$\begin{aligned}
V_r &= V_{x0} \cos\beta \cos\theta - V_{y0} \sin\beta \cos\theta + W(\beta) \sin\theta \\
&- \left[\frac{\partial V}{\partial x} r \cos\beta + \frac{\partial V}{\partial y} r \sin\beta \right] \cos\beta \cos\theta \\
&- \left[\frac{\partial V}{\partial x} r \cos\beta + \frac{\partial V}{\partial y} r \sin\beta \right] \sin\beta \cos\theta \\
&= -V_{x0} \cos\beta \cos\theta - V_{y0} \sin\beta \cos\theta + W(\beta) \sin\theta \\
&- \frac{\partial V}{\partial x} r \cos^2\beta \cos\theta - \frac{\partial V}{\partial y} r \sin\beta \cos\beta \cos\theta \\
&- \frac{\partial V}{\partial x} r \cos\beta \sin\beta \cos\theta - \frac{\partial V}{\partial y} r \sin^2\beta \cos\theta \\
&= -V_{x0} \cos\beta \cos\theta - V_{y0} \sin\beta \cos\theta + W(\beta) \sin\theta && \text{term A} \\
&- \left[\frac{\partial V}{\partial y} r + \frac{\partial V}{\partial x} r \right] \cos\theta \frac{2 \sin\beta \cos\beta}{2} && \text{term B} \\
&- \left[\frac{\partial V}{\partial x} r \cos^2\beta + \frac{\partial V}{\partial y} r \sin^2\beta \right] \cos\theta && \text{term C}
\end{aligned}$$

Term B can be written $(2 \sin\beta \cos\beta = \sin 2\beta)$

$$- \left[\frac{\partial V}{\partial y} r + \frac{\partial V}{\partial x} r \right] \frac{\cos\theta}{2} \sin 2\beta$$

Term C can be written $(\cos 2\beta = -\sin^2\beta + \cos^2\beta)$ $\cos 2\beta = 2 \cos^2\beta - 1$
 $\cos 2\beta + 1 = 2 \cos^2\beta$
 $-\cos 2\beta + 1 = 2 \sin^2\beta$

$$\begin{aligned}
&- \left[\frac{\partial V}{\partial x} r \left(\frac{\cos 2\beta + 1}{2} \right) + \frac{\partial V}{\partial y} r \left(\frac{-\cos 2\beta + 1}{2} \right) \right] \cos\theta \\
&- \left[\frac{\partial V}{\partial x} r + \frac{\partial V}{\partial y} r + \left(-\frac{\partial V}{\partial y} r + \frac{\partial V}{\partial x} r \right) \cos 2\beta \right] \frac{r \cos\theta}{2}
\end{aligned}$$

separating

$$\left[\frac{\partial V}{\partial x} r + \frac{\partial V}{\partial y} r \right] \frac{r \cos\theta}{2} + \left[\frac{\partial V}{\partial x} r + \frac{\partial V}{\partial y} r \right] \frac{r \cos\theta}{2} \cos 2\beta$$

which gives us

$$\begin{aligned}
V_r(\beta) &= \frac{r \cos \theta}{2} \left[\frac{\partial V}{\partial x} \frac{x}{y} + \frac{\partial V}{\partial y} \right] + W(\beta) \sin \theta \quad (\alpha_0) \\
&+ [-V_{x_0} \cos \beta - V_{y_0} \sin \beta] r \cos \theta \quad (\alpha_1 \cos \beta + b_1 \sin \beta) \\
&+ \left(- \left[\frac{\partial V}{\partial y} \frac{x}{\partial x} + \frac{\partial V}{\partial x} \frac{y}{\partial y} \right] \sin 2\beta + \left[\frac{\partial V}{\partial x} \frac{x}{\partial x} + \frac{\partial V}{\partial y} \frac{y}{\partial y} \right] \cos 2\beta \right) \frac{r \cos \theta}{2} \\
&\quad (\alpha_2 \cos 2\beta + b_2 \sin 2\beta)
\end{aligned}$$

This decomposes into the traditional Fourier Transfer Form:

$$V_r = \alpha_0 + \sum_{N=1}^{\infty} (\alpha_N \cos N\beta + b_N \sin N\beta)$$

5 parameter Least Squares Curve Fit

$$\text{Minimum} = \sum_{i=1}^N (V_i - A_0 - A_1 \cos \theta_i - B_1 \sin \theta_i - A_2 \cos 2\theta_i - B_2 \sin 2\theta_i)^2$$

where N = number of points

V_i = radial velocity at point i

θ_i = beam azimuth angle.

APPENDIX D

Tower Atmospheric Data and Corresponding Stability Information
for Time Periods during Lidar/Tower Mean Wind Comparison

		u-bar	v-bar	w-bar	t-bar	t d	w't'	u'w'	v'w'	p sub 10	l sub 10	t lapse	da-la	bouy pro	mech pro	pro	flux
														*1000	u*1000	v*1000	rich
3-4-82	10.00	-3.33	-5.63	-0.35	1.29	-2.52	0.0152	-0.2075	-0.0567	830.0900		0.1200	0.00	11.55	69.10	3.19	-0.16
	22.00	-4.24	-6.75	-0.41	1.17		0.0184	-0.1103	0.0012		-2.5200	0.4100	0.14	15.41	8.36	-0.11	-1.87
	50.00	-4.18	-7.05	-0.28	0.76		0.0105	-0.0462	-0.0037		-75.5800	0.4800	-0.01	13.54	-0.10	0.04	228.10
	100.00	-4.58	-7.05	-0.16	0.28	-3.06	0.0073	-0.0147	-0.0185		-19.5100	0.4800	-0.01	25.55	0.12	0.00	-217.26
	150.00	-4.73	-7.11	-0.40	-0.20	-3.47	0.0044	-0.0179	-0.0158			0.4700	-0.02	-22.54	0.05	0.02	310.21
	200.00	-4.40	-6.97	-0.24	-0.67	-3.63	0.0024	-0.0071	-0.0599			0.6400	0.15	-3.51	0.05	-0.17	-29.05
	250.00	-4.22	-6.88	-0.23	-1.31	-3.93	0.0001	0.0602	-0.0832			0.3400	-0.15	-0.07	0.22	-0.15	1.12
300.00	-3.25	-6.86	-0.11	-1.65	-4.45	0.0171	-0.1624	-0.0069					-10.16	-3.15	-0.00	-3.22	
3-5-82	10.00	-0.16	-2.51	-0.07	-7.17	-8.46	0.0294	-0.0307	-0.0392	840.5700	-14.1800	0.1500	0.03	-4.02	0.49	0.98	7.72
	22.00	-0.55	-2.78	-0.29	-7.32		0.0001	-0.0047	-0.0329		-10.9900	0.5600	0.29	-0.01	0.15	0.74	0.01
	50.00	-0.31	-2.94	-0.14	-7.88		0.0002	0.0144	0.0083			0.5000	0.01	-0.02	0.12	-0.05	0.33
	100.00	-0.65	-2.86	-0.03	-8.38	-8.62	0.0001	0.0193	-0.0129			0.4800	-0.01	-0.01	-0.13	-0.02	-0.08
	150.00	-1.04	-2.31	-0.21	-8.86	-9.12	0.0001	0.0016	-0.0158			0.3400	-0.15	-0.01	-0.01	-0.17	-0.06
	200.00	-0.70	6.95	-0.19	-9.20	-9.28	-0.0001	0.0432	-0.0369			0.1500	-0.34	0.01	0.29	-6.83	0.00
	250.00	-1.12	-6.52	-0.27	-9.35	-9.42	-0.0008	0.0454	-0.0262			0.4800	-0.01	0.08	-0.38	7.06	-0.01
300.00	-1.06	-12.41	-0.16	-9.83	-9.49	-0.0108	0.0889	-0.0281					1.08	0.11	3.31	-0.32	
3-8-82	10.00	-2.40	-0.34	-0.12	7.00	-4.61	0.1541	-0.1256	0.1487	837.9400	-23.5800	0.3800	0.26	21.57	30.14	-0.51	-0.73
	22.00	-2.96	-0.56	-0.32	6.62		0.0001	-0.1669	0.1127			0.5700	0.30	0.01	7.79	-2.07	-0.00
	50.00	-2.66	-0.88	-0.22	6.05		-0.0003	-0.0110	0.3808		342.2700	0.5400	0.05	-0.05	-0.12	-4.35	-0.01
	100.00	-2.75	-1.32	-0.19	5.51	-4.71	-0.0003	-0.3946	0.1568		-1.1800	0.5600	0.07	-0.05	0.71	-1.38	-0.08
	150.00	-3.21	-1.29	-0.48	4.95	-4.60	-0.0005	-0.3124	0.2433			0.4200	-0.07	-0.10	2.87	0.15	0.03
	200.00	-3.38	-2.65	-0.26	4.53	-4.69	-0.0004	-0.1477	-0.0625			0.4500	-0.04	-0.09	0.50	1.70	0.04
	250.00	-3.95	-1.35	-0.60	4.08	-5.26	-0.0544	-0.3969	-0.0815			0.5500	0.06	13.07	4.52	-2.12	-5.43
300.00	-4.38	-1.96	-0.59	3.53	-5.39	0.0623	-0.9184	-0.0534					17.30	7.90	0.65	-2.02	
3-9-82	10.00	5.43	9.53	0.37	13.45	-9.60	0.2381	-0.3849	-0.0531	838.9500	-83.7900	0.5100	0.39	17.35	-209.00	-5.06	0.08
	22.00	6.26	10.76	0.01	12.94		0.2871	-0.6141	0.0129		-4.7700	0.6400	0.37	21.74	-42.48	1.32	0.53
	50.00	7.38	11.07	0.30	12.30		0.3566	-0.7848	-0.2083		-6.6100	0.7000	0.21	28.41	-31.39	-2.31	0.84
	100.00	7.38	11.31	-0.13	11.60	-9.97	-0.0762	-0.5443	-0.8304			0.5500	0.06	-6.44	0.00	-3.99	-1.62
	150.00	7.37	11.72	-0.01	11.05	-10.36	0.3256	-0.5185	-1.0028			0.5100	0.02	28.88	0.10	-8.22	3.56
	200.00	8.34	9.22	-0.31	10.54	-10.39	0.2958	-0.2718	-1.6731			0.4100	-0.08	27.50	-5.27	83.66	-0.35
	250.00	8.37	11.92	-0.11	10.13	-10.44	0.2633	-0.2925	-2.1847			0.6100	0.12	25.47	-0.18	-117.97	0.22
300.00	8.04	12.44	0.42	9.52	-10.64	0.2777	-0.5982	-2.6148					28.59	3.95	-27.19	1.23	
3-10-82	10.00	5.70	0.76	0.31	15.95	-8.33	0.0507	-0.1203	-0.0052	833.0200	-69.3000	0.3000	0.18	3.12	-68.57	-0.04	0.05
	22.00	6.25	0.96	0.01	15.65		0.0002	-0.1191	0.0561			0.4800	0.21	0.01	-5.46	0.93	0.00
	50.00	7.07	0.98	0.26	15.17		0.0685	-0.1906	0.0806			0.5700	0.08	4.43	-5.58	0.06	0.80
	100.00	7.10	0.85	0.22	14.60	-8.57	0.0708	-0.1854	0.1605			0.4900	0.00	4.75	-0.11	-0.42	8.99
	150.00	6.42	1.34	0.35	14.11	-8.85	0.0112	-0.1075	0.1603			0.5100	0.02	0.78	1.46	1.57	-0.26
	200.00	6.68	0.27	0.28	13.60	-8.92	0.0865	-0.1455	0.1491			0.5100	0.02	6.23	-0.76	-3.19	1.58
	250.00	6.09	1.79	0.28	13.09	-9.04	0.0521	0.0541	0.1412			0.4500	-0.04	3.90	-0.64	4.29	-1.07
300.00	5.81	2.01	0.24	12.64	-9.15	0.0278	0.2838	0.1791					2.16	-1.59	0.79	2.69	
3-12-82	10.00	-0.14	6.18	0.25	9.25	-9.54	0.3444	1.7522	0.2962	825.8400	-3.1300	0.6700	0.55	36.49	-24.53	18.31	5.86
	22.00	-0.34	14.14	-0.15	8.58		0.2977	-0.5953	-0.0006			0.7400	0.47	34.00	9.92	-0.40	-3.57
	50.00	0.42	13.50	0.09	7.84		0.3006	-0.1091	-0.1888		-9.8100	0.6800	0.19	37.57	-2.96	4.32	-27.75
	100.00	0.43	14.78	-0.10	7.16	-11.06	0.5147	-0.4684	-0.3206		-50.8700	0.5600	0.07	70.45	-0.09	-8.21	8.49
	150.00	0.31	15.03	-0.04	6.60	-11.12	0.0175	-1.0551	-0.3155			0.5200	0.03	2.60	2.53	-1.58	-2.72
	200.00	1.30	3.35	-0.45	6.08	-11.56	0.3076	1.3148	-0.5995			0.4300	-0.06	49.58	26.03	140.04	-0.30
	250.00	1.49	4.08	-0.46	5.65	-10.72	0.2838	0.7772	-0.6147			0.5900	0.10	49.23	2.95	-8.97	8.18
300.00	1.17	8.02	0.06	5.06	-10.64	0.1602	0.2196	-0.6728					31.03	-1.41	-53.02	0.57	
3-15-82	10.00	5.93	1.66	0.34	14.12	-6.99	0.1304	0.0689	-0.0788	819.4700	-84.4600	0.4200	0.30	9.05	40.86	-1.31	-0.23
	22.00	6.47	1.94	0.13	13.70		0.0003	-0.0676	0.1101		-40.8400	0.5400	0.27	0.02	-3.04	2.57	0.05
	50.00	7.28	1.97	0.46	13.16		0.1869	-0.3056	0.2722		-75.4200	0.6800	0.19	13.92	-8.84	0.29	1.63
	100.00	7.42	1.85	0.29	12.48	-7.18	0.2321	-0.5694	0.3271			0.4800	-0.01	18.23	-1.59	-0.79	7.66
	150.00	7.08	2.21	0.60	12.00	-7.47	0.0002	-0.7235	0.2999			0.5700	0.08	0.02	4.92	2.16	-0.00
	200.00	6.66	1.22	0.06	11.43	-7.44	0.2491	-0.4706	0.2117			0.4900	0.00	21.36	3.95	-4.19	89.50
	250.00	7.56	2.44	0.64	10.94	-7.69	0.2611	-0.6217	0.2932			0.5400	0.05	23.39	-11.19	7.15	5.79
300.00	7.06	2.95	0.75	10.40	-7.02	0.1928	0.0486	0.1998					18.17	-0.49	2.04	-11.71	

3-17-82	10.00	-0.25	-1.14	-0.05	12.49	-10.47	0.2006	-0.0477	0.0192	832.2500	-4.3300	0.3600	0.24	15.74	1.19	-0.22	-16.17
	22.00	-0.55	-1.22	-0.23	12.13		0.2419	0.1699	0.0523		-2.5200	0.5600	0.29	19.54	-4.25	-0.35	4.25
	50.00	-0.44	-1.31	0.12	11.57		-0.0007	0.4347	0.1561		-75.5800	0.6200	0.13	-0.06	1.71	-0.50	0.05
	100.00	-0.89	-1.58	0.46	10.95	-10.66	0.0875	0.7617	-0.2381		-19.5100	0.5800	0.09	7.83	-6.86	1.29	1.41
	150.00	-1.51	-1.66	0.95	10.37	-10.85	0.1548	0.4535	-0.7928			0.4500	-0.04	14.63	-5.62	1.27	3.36
	200.00	-1.49	-2.93	1.01	9.92	-10.95	0.1548	-0.1014	-0.7463			0.3900	-0.10	15.29	-0.04	18.96	-0.81
	250.00	-1.92	-1.64	1.03	9.53	-10.90	0.2241	-0.7652	-0.7635			0.6700	0.18	23.04	6.58	-19.70	1.76
	300.00	-1.88	-1.83	1.27	8.86	-11.03	0.2555	-1.4461	-0.7008					28.26	-1.16	2.66	-18.76
3-24-82	10.00	9.69	-8.45	0.24	10.73	-9.71	1.1024	-1.4402	-0.9233	831.4900		0.2800	0.16	100.69	-1395.55	78.02	0.08
	22.00	70.79	-9.11	0.07	10.45		1.0216	-1.3247	-0.6442		-2.5200	1.0800	0.81	95.81	-6744.93	35.43	0.01
	50.00	11.63	-8.67	0.23	9.37		0.7531	-0.6427	-0.0233		-75.5800	1.4700	0.98	78.77	1357.93	-0.37	-0.06
	100.00	10.74	-4.15	0.35	7.90	-10.18	-0.0435	1.0237	1.2477		-19.5100	0.3600	-0.13	-5.40	-18.22	112.79	0.06
	150.00	11.54	-10.29	0.44	7.54	-9.63	0.5015	-0.0931	0.0156			0.1100	-0.38	65.18	-1.49	-1.92	19.14
	200.00	9.63	-0.55	0.53	7.43	-9.57	0.0103	0.6131	-0.1959			0.2400	-0.25	1.36	-23.42	-38.16	0.02
	250.00	5.22	-2.17	3.24	7.19	-9.97	-8.8024	-0.5434	7.2383			0.2000	-0.29	-1199.77	47.93	-234.52	-6.43
	300.00	6.48	-4.58	-0.61	6.99	-10.29	4.0816	-3.6933	-2.7011	834.1300	-14.1800			572.24	-93.07	130.19	-15.42
3-24-82	10.00	8.19	-13.49	0.04	1.02	-7.79	0.1968	-0.6901	-0.0415		-10.9900	0.3000	0.18	189.08	-565.19	5.60	0.34
	22.00	9.14	-15.88	0.05	0.72		0.2134	-1.3012	0.0776		342.2700	0.7200	0.45	290.46	-103.01	-15.46	2.45
	50.00	10.49	-8.50	0.20			0.2077	1.8602	2.1063		-1.1800	0.7900	0.30	ERR	89.69	555.16	ERR
	100.00	9.73	-7.43	0.39	-0.79	-7.95	-0.0017	1.6807	1.7697			0.5700	0.08	2.11	-25.55	37.87	-0.17
	150.00	10.27	-17.82	0.20	-1.36	-8.04	0.1724	-0.6588	0.3315			0.4600	-0.03	-124.23	-7.12	-68.89	-1.63
	200.00	4.49	-0.51	0.34	-1.82	-7.88	0.1334	-0.2017	-0.7323			0.4800	-0.01	-71.83	23.32	-253.52	-0.31
	250.00	3.12	-0.11	0.76	-2.30	-8.17	0.0877	0.0179	0.0254			0.5000	0.01	-37.37	-0.49	0.20	-130.08
	300.00	12.59	-17.93	0.21	-2.80	-8.20	0.0507	-0.1061	1.0653	835.6900	-59.7200			-17.75	-20.10	-379.67	-0.04
3-24-82	10.00	5.51	-12.58	-0.07	-0.20	-7.80	0.1652	-0.2487	0.0974		-4.7700	0.3000	0.18	-809.48	-137.03	-12.25	-5.42
	22.00	6.12	-14.72	-0.11	-0.50		0.1691	-0.7541	0.1311		342.2700	0.5800	0.31	-331.44	-38.33	-23.38	-5.37
	50.00	6.89	-13.09	-0.01	-1.08		0.1648	0.0836	0.4653		-1.1800	0.6900	0.20	-149.54	2.30	27.09	5.09
	100.00	6.50	-10.40	0.24	-1.77	-7.59	0.0001	1.4015	1.0895			0.5800	0.09	-0.06	-10.93	58.62	0.00
	150.00	5.96	-13.26	0.03	-2.35	-8.16	0.1004	-0.6646	0.2156			0.5000	0.01	-41.87	7.18	-12.33	-8.12
	200.00	8.22	1.96	0.09	-2.85	-8.06	0.0981	-0.2552	0.3431			0.4600	-0.03	-33.73	-11.54	104.44	0.36
	250.00	8.39	1.11	-0.10	-3.31	-8.34	0.0817	0.0337	0.3415			0.5700	0.08	-24.19	0.11	-5.81	-4.25
	300.00	9.06	-16.52	0.12	-3.88	-8.33	0.0714	-0.2294	0.2856	837.5500	-43.7500			-18.03	-3.07	-100.70	-0.17
3-24-82	10.00	4.94	-9.78	0.01	-1.04	-8.33	0.0877	-0.4322	-0.0616		-4.7700	0.2700	0.15	-82.64	-213.51	6.02	-0.40
	22.00	5.42	-11.05	-0.10	-1.31		0.0795	-0.4071	-0.0107		-6.6100	0.4800	0.21	-59.47	-16.28	1.13	-3.93
	50.00	6.26	-11.99	-0.01	-1.79		0.0745	-0.3564	-0.0304			0.6000	0.11	-40.79	-10.69	1.02	-4.22
	100.00	5.46	-12.64	-0.09	-2.39	-8.34	-0.0003	-0.2503	-0.1389			0.5400	0.05	0.12	4.00	1.81	-0.02
	150.00	4.75	-9.27	-0.10	-2.93	-8.62	0.0459	-0.1881	-0.0284			0.4900	-0.00	-15.35	2.67	-1.91	20.28
	200.00	7.08	3.23	-0.07	-3.42	-8.47	0.0456	-0.0921	0.0572			0.4800	-0.01	-13.07	-4.29	14.30	1.31
	250.00	6.88	-3.04	-0.21	-3.90	-8.73	0.0482	0.3264	0.2103			0.5100	0.02	-12.11	-1.31	-26.37	-0.44
	300.00	7.39	12.35	-0.01	-4.41	-8.76	0.0462	-0.0571	0.0451	838.7100	-69.3000			-10.27	-0.58	13.88	0.77
3-24-82	10.00	3.72	-8.14	-0.05	-1.55	-8.64	0.0518	-0.2471	-0.0806			0.2000	0.08	-32.75	-91.92	6.56	-0.38
	22.00	3.98	-9.01	-0.06	-1.75		0.0702	-0.3406	-0.0371		-9.8100	0.4600	0.19	-39.31	-7.38	2.69	-8.38
	50.00	4.47	-10.06	0.13	-2.21		0.0783	-0.3086	-0.0277		-50.8700	0.5400	0.05	-34.72	-5.40	1.04	-7.96
	100.00	3.95	-10.49	0.23	-2.75	-8.30	0.0001	-0.0876	0.0506			0.5300	0.04	-0.04	0.91	-0.44	0.07
	150.00	3.77	-9.04	0.19	-3.28	-8.91	0.0713	-0.3318	-0.0029			0.4800	-0.01	-21.30	1.19	-0.08	19.19
	200.00	4.79	3.70	0.34	-3.76	-8.79	0.0973	-0.0088	-0.0016			0.5000	0.01	-25.36	-0.18	-0.41	-43.19
	250.00	4.90	-8.94	0.27	-4.26	-9.00	0.0931	0.0289	-0.0352			0.5100	0.02	-21.42	0.06	8.90	2.39
	300.00	5.59	-10.11	0.48	-4.77	-9.02	0.0883	-0.2885	-0.1262	840.4600	-3.1300			-18.14	-3.98	2.95	-17.64
3-24-82	10.00	2.86	-7.15	-0.12	-2.98	-7.41	0.0284	-0.1699	-0.0002		-40.8400	0.1700	0.05	-9.34	-48.59	0.01	-0.19
	22.00	2.93	-7.93	-0.14	-3.15		0.0228	-0.1914	0.0405		-9.8100	0.4100	0.14	-7.09	-1.12	-2.63	-1.89
	50.00	3.49	-8.34	-0.01	-3.56		-0.0071	-0.2503	0.0449		-50.8700	0.4900	-0.00	1.95	-5.01	-0.66	0.35
	100.00	2.95	-8.63	0.21	-4.05	-7.36	-0.0002	-0.3872	0.0424			0.5100	0.02	0.05	4.18	-0.25	-0.01
	150.00	2.84	-8.02	0.20	-4.56	-7.80	-0.0308	-0.2936	0.2238			0.4800	-0.01	6.62	0.65	2.73	-1.96
	200.00	3.17	6.55	0.20	-5.04	-7.64	-0.0391	-0.2321	0.3101			0.4700	-0.02	7.60	-1.53	90.36	-0.09
	250.00	3.05	-8.12	0.08	-5.51	-7.92	-0.0551	-0.4424	0.1675			0.4700	-0.02	9.80	1.06	-49.14	0.20
	300.00	3.32	-8.47	0.29	-5.98	-8.05	-0.0432	-0.1598	0.2278					7.08	-0.86	-1.59	2.88

3-31-82	10.00	-1.83	0.07	-0.07	14.12	-11.92	0.1255	0.0078	0.1829	835.6600	-84.4600	0.4500	0.33	8.71	-1.43	0.13	6.70
	22.00	-2.13	-0.02	-0.35	13.67		0.2284	0.0269	0.0288		-40.8400	0.5800	0.31	16.37	-0.67	-0.22	18.43
	50.00	-1.85	-0.08	-0.08	13.09		0.1745	-0.0139	-0.1211		-75.4200	0.6200	0.13	13.06	-0.14	0.26	-108.42
	100.00	-2.34	-0.23	-0.56	12.47	-11.92	0.0001	-0.0813	-0.2246		-19.5100	0.5500	0.06	0.01	0.80	0.67	-0.01
	150.00	-2.75	0.12	-0.32	11.92	-12.37	0.4375	-0.3121	-0.8689			0.4300	-0.06	35.97	2.56	-6.08	10.21
	200.00	-2.30	-1.10	-0.27	11.49	-12.35	0.3289	-0.1052	-0.5631			0.4400	-0.05	28.05	-0.95	13.74	-2.19
	250.00	-2.46	0.11	-0.44	11.05	-12.40	0.3717	-0.1378	-0.4417			0.5400	0.05	32.97	0.44	-10.69	3.22
	300.00	-3.08	0.38	-0.44	10.51	-12.54	0.3443	-0.0821	-0.1185					32.10	1.02	-0.64	-84.90
4-05-82	10.00	1.71	-4.56	-0.12	7.70	-17.86	0.0719	-0.0436	-0.1108	836.0100	-10.3500	0.2700	0.15	9.15	-7.46	5.05	3.81
	22.00	1.76	-5.03	-0.19	7.43		0.0556	0.0693	0.0047		-2.5200	0.4100	0.14	7.33	0.29	-0.18	-70.07
	50.00	2.09	-5.45	-0.18	7.02		0.0458	0.3022	0.0282		-75.5800	0.5000	0.01	6.39	3.56	-0.42	2.04
	100.00	1.82	-5.74	-0.27	6.52	-18.19	0.0434	0.4721	-0.0952		-19.5100	0.5100	0.02	6.52	-2.55	0.55	3.27
	150.00	1.73	-5.29	-0.42	6.01	-18.45	0.0621	0.4335	-0.0121			0.4900	0.00	10.13	-0.78	-0.11	11.39
	200.00	2.25	-6.64	-0.49	5.52	-18.52	0.0578	0.1948	0.0389			0.4300	-0.06	10.26	2.03	-1.05	-10.52
	250.00	2.58	-4.90	-0.64	5.09	-18.76	0.0656	-0.0584	0.2324			0.5100	0.02	12.63	-0.39	8.09	-1.64
	300.00	3.34	-4.61	-0.37	4.58	-18.86	0.1196	0.2569	-0.0271					25.59	3.90	-0.16	-6.83
4-20-82	10.00	3.52	-3.84	-0.02	-0.31	-4.91	0.0047	-0.1501	-0.0471	849.2900		2.9890	2.87	-14.81	-52.84	1.81	-0.29
	22.00	3.81	-4.19	0.06	-3.30		-0.0138	0.2262	-0.0325		-2.5200	0.3900	0.12	4.10	5.47	0.95	-0.64
	50.00	4.53	-4.55	-0.15	-3.69		0.0276	-0.1684	0.0238		-75.5800	0.4700	-0.02	-7.33	-4.33	-0.31	-1.58
	100.00	4.15	-4.98	-0.01	-4.16	-5.55		-0.2667	0.0691		-1.1500	0.5000	0.01	0.00	2.03	-0.59	0.00
	150.00	4.25	-4.95	0.02	-4.66	-6.06	0.0013	-0.3282	0.0031			0.4400	-0.05	-0.27	-0.66	0.00	-0.42
	200.00	4.64	6.21		-5.10	-6.12	0.0002	-0.1785	0.2364			0.4500	-0.04	-0.04	-1.39	52.76	0.00
	250.00	3.87	-5.52		-5.55	-7.38	0.0034	-4.3274	1.6418			0.4800	-0.01	-0.60	66.64	-385.17	-0.00
	300.00	5.02	0.47	0.02	-6.03	-6.70	0.0001	0.8104	1.9185					-0.02	18.64	229.84	0.00
4-23-82	10.00	-0.44	-1.95	-0.05	16.67	-10.32	0.3171	-0.0754	-0.1587	837.8900	-5.5100	0.3400	0.22	18.64	3.32	3.09	-2.91
	22.00	-0.50	-2.27	-0.48	16.33		0.3602	0.0846	-0.0725		-10.9900	0.5100	0.24	21.62	-0.42	1.93	-14.31
	50.00	-0.24	-2.57	-0.09	15.82		0.3481	0.1081	0.0388		342.2700	0.5800	0.09	21.56	1.00	-0.42	-36.67
	100.00	-0.47	-2.98	-0.28	15.24	-10.54	0.3291	0.3139	0.0597		-1.1800	0.6400	0.15	21.16	-1.44	-0.49	10.95
	150.00	-0.82	-2.45	0.04	14.60	-14.48	0.3389	0.2741	0.2371			0.4700	-0.02	22.75	-1.92	2.51	-38.26
	200.00	-0.27	-2.63	0.02	14.13	-11.19	0.2662	0.3424	0.3412			0.2600	-0.23	18.46	3.77	-1.23	-7.27
	250.00	-0.09	-2.66	-0.18	13.87	-11.20	0.1015	-0.2032	0.1129			0.7100	0.22	7.17	-0.73	-0.07	8.97
	300.00	0.38	-2.97	-0.19	13.16	-11.39	0.0483	-0.1437	0.3265					3.60	-1.35	-2.02	1.07
4-23-82	10.00	-0.69	-2.97	-0.13	17.44	-11.01	0.2744	-0.1440	-0.0744	837.5800	-16.9300	0.3000	0.18	15.42	9.94	2.21	-1.27
	22.00	-0.69	-3.44	-0.52	17.14		0.3535	0.0501	0.0068		-4.7700	0.5500	0.28	20.21	0.00	-0.27	75.89
	50.00	-0.59	-3.73	-0.28	16.59		0.3769	0.1201	0.0753		342.2700	0.6200	0.13	22.26	0.43	-0.78	63.44
	100.00	-0.77	-4.34	-0.38	15.97	-11.23	0.4711	0.1124	-0.1307		-1.1800	0.7000	0.21	28.91	-0.40	1.59	-24.30
	150.00	-0.87	-4.23	-0.08	15.27	-12.13	0.3776	0.0706	-0.0488			0.4800	-0.01	24.23	-0.14	-0.11	97.50
	200.00	-0.41	-4.27	0.18	14.79	4.76	0.3727	0.1335	0.0491			0.3300	-0.16	24.70	1.23	-0.04	-20.77
	250.00	-0.46	-4.03	0.17	14.46	3.41	0.4161	-0.0945	0.1253			0.7000	0.21	28.20	0.09	0.60	-40.52
	300.00	-0.09	-3.57	0.16	13.76	-12.13	0.3986	-0.1843	0.3445	839.6600	-0.3500			28.39	-1.36	3.17	-15.72
4-27-82	10.00	1.53	-2.74	-0.04	7.71	4.81	0.0891	-0.0053	-0.0166		-4.7700	0.2500	0.13	11.33	-0.81	0.45	31.81
	22.00	1.58	-2.96	-0.27	7.46		0.0556	0.0156	0.0035		-6.6100	0.4200	0.15	7.30	0.07	-0.06	-8764.83
	50.00	1.99	-3.20	-0.13	7.04		0.0318	0.0765	-0.0078		-50.8700	0.5200	0.03	4.43	1.12	0.07	-3.73
	100.00	1.77	-3.32	-0.13	6.52	4.33	0.0238	0.0165	-0.0225			0.5800	0.09	3.58	-0.07	0.05	194.17
	150.00	1.57	-2.88	-0.20	5.94	4.01	0.0035	0.1037	-0.1565			0.4500	-0.04	0.58	-0.41	-1.38	0.32
	200.00	1.68	-2.89	-0.29	5.49	9.11	-0.0025	0.1344	-0.0861			0.2900	-0.20	-0.45	0.30	0.02	1.43
	250.00	1.30	-2.61	1.09	5.20	3.71	-0.1956	0.0589	0.0176			0.4900	0.00	-36.86	-0.45	0.10	-105.60
	300.00	1.14	-2.34	-0.25	4.71	3.53	-0.0119	0.0991	0.0167	836.1500	-69.3000			-2.48	-0.32	0.09	-10.91
4-29-82	10.00	1.64	-6.76	-0.16	15.88	-0.21	0.0302	-0.1864	0.0063		-40.8400	0.1800	0.06	1.86	-30.57	-0.43	0.06
	22.00	2.01	-7.76	-0.30	15.70		0.0333	-0.2086	0.0831		-9.8100	0.4200	0.15	2.08	-6.43	-6.93	0.16
	50.00	2.43	-8.26	0.01	15.28		0.0607	-0.3309	0.0902		-50.8700	0.5000	0.01	3.89	-4.96	-1.61	0.59
	100.00	2.22	-8.89	0.09	14.78	-0.58	0.0759	0.0297	0.1532			0.5300	0.04	5.03	-0.12	-1.93	2.45
	150.00	2.49	-8.85	0.09	14.25	-0.92	0.0479	0.0195	0.0791			0.4800	-0.01	3.29	0.11	0.06	-19.54
	200.00	2.79	-8.76	0.16	13.77	-0.99	0.0272	0.2531	0.1333			0.4700	-0.02	1.94	1.52	0.24	-1.10
	250.00	2.80	-9.08	-0.05	13.30	-1.14	0.0145	0.2623	0.1591			0.5000	0.01	1.07	0.05	-1.02	1.11
	300.00	3.32	-8.89	0.14	12.80	-1.23	0.0041	0.3338	0.2306					0.31	3.47	0.88	-0.07

4-29-82	10.00	2.46	-9.81	-0.20	11.31	2.72	0.1123	-0.0262	0.1325	838.2800	-3.1300	0.3300	0.21	9.73	-6.45	-13.00	0.50
	22.00	2.77	-12.67	-0.23	10.98		0.1601	-0.4379	0.0243		-40.8400	0.5000	0.23	14.29	-11.31	-5.79	0.84
	50.00	3.30	-13.33	-0.05	10.48		0.1243	0.1101	0.0357		-9.8100	0.6300	0.14	11.62	2.08	-0.84	-9.35
	100.00	2.85	-11.40	0.13	9.85	2.70	0.1626	0.2631	-0.0388		-50.8700	0.5800	0.09	16.18	-2.37	-1.50	4.19
	150.00	3.25	-14.27	-0.13	9.27	2.27	0.0507	-0.3632	-0.1176			0.4900	0.00	5.36	-2.91	6.75	-1.39
	200.00	3.17	-11.17	0.01	8.78	2.31	0.0105	0.1871	0.0299			0.4500	-0.04	1.17	-0.30	1.85	-0.75
	250.00	3.11	-10.11	-0.27	8.33	2.12	-0.0099	0.7833	0.1452			0.5300	0.04	-1.16	-0.94	3.08	0.54
300.00	3.73	-14.23		7.80	2.09	0.0029	-0.1048	0.0111					0.36	-1.30	-0.91	0.16	
5-10-82	10.00	-1.04	-0.64	-0.11	17.97	-9.39	0.2292	-0.3734	0.1107	830.5000	-84.4600	0.3300	0.21	12.50	38.83	-0.71	-0.33
	22.00	-1.25	-0.73	-0.47	17.64		0.2756	-0.2603	0.1128		-40.8400	0.6500	0.38	15.31	4.56	-0.85	-4.13
	50.00	-1.05	-0.86	-0.06	16.99	-9.56	0.3039	-0.0332	-0.2521		-1.6800	0.7800	0.29	17.53	-0.24	1.17	-18.78
	100.00	-1.54	-1.28	-0.19	16.21	-9.47	0.2842	0.3988	-0.6522		-19.5100	0.5300	0.04	17.18	-3.91	5.48	-10.94
	150.00	-2.19	-1.08	-0.05	15.68	-8.70	0.2641	0.9133	-0.9427			0.4100	-0.08	16.51	-11.87	-3.77	1.06
	200.00	-1.99	-1.02	-0.02	15.27	-0.29	0.2861	0.8871	-1.2086			0.3600	-0.13	18.36	3.55	-1.45	-8.75
	250.00	-2.44	-0.70	0.18	14.91	-9.14	0.3389	0.7324	-1.1457			0.5800	0.09	22.28	-6.59	-7.33	1.60
300.00	-2.56	-0.58	0.33	14.33	-9.94	0.3222	0.4292	-0.7366					22.03	-1.03	-1.77	7.88	
5-12-82	10.00	1.91	-0.18	0.05	5.55	-3.84	0.0144	0.0126	-0.0245	833.0900	-10.3500	0.1800	0.06	2.54	2.41	0.04	-1.04
	22.00	2.00	-0.17	-0.31	5.37		0.0114	0.0466	-0.0441		-2.5200	0.3500	0.08	2.08	0.35	-0.04	-6.65
	50.00	2.36	-0.23	-0.07	5.02	-3.49	0.0033	0.0521	-0.0593		-75.5800	0.4800	-0.01	0.64	0.67	0.13	-0.81
	100.00	2.27	-0.35	-0.07	4.54	-3.54	-0.0047	0.0386	-0.0246		-1.1500	0.4900	0.00	-1.01	-0.07	0.06	-97.18
	150.00	1.82	-0.15	-0.16	4.05	-3.06	0.0024	0.0002	-0.0173			0.4200	-0.07	0.58	-0.00	-0.07	8.18
	200.00	2.44	-0.68	-0.18	3.63	-2.95	0.0086	-0.0068	-0.0328			0.4300	-0.06	2.32	-0.08	0.35	-8.82
	250.00	2.13	-1.24	-0.21	3.20	-2.53	0.0065	0.0351	-0.0373			0.3400	-0.15	1.99	-0.22	0.42	-9.95
300.00	10.25	-1.78	0.03	2.86	-2.24	0.0003	0.0109	-0.0149					0.10	1.77	0.16	-0.05	
5-12-82	10.00	2.56	0.08	0.07	5.83	-4.06	0.0241	-0.0181	-0.0054	832.5500	-8.2100	0.1700	0.05	4.05	-4.63	-0.00	0.87
	22.00	2.67	0.12	-0.23	5.66		0.0284	-0.0376	-0.0077		-20.8400	0.3300	0.06	4.92	-0.34	-0.03	13.28
	50.00	3.09	-0.10	-0.03	5.33	-3.76	0.0342	-0.0507	-0.0598		342.2700	0.5000	0.01	6.29	-0.76	0.47	21.64
	100.00	2.98	-0.24	0.05	4.83	-3.76	0.0067	-0.0705	-0.0217		-1.1800	0.4900	0.00	1.36	0.16	0.06	-6.30
	150.00	2.71	-0.13	-0.06	4.34	-3.21	0.0143	-0.0128	-0.1049			0.4200	-0.07	3.23	0.07	-0.23	19.97
	200.00	3.15	-0.56	-0.16	3.92	-3.08	0.0122	-0.0046	-0.0979			0.5900	0.10	3.05	-0.04	0.84	-3.81
	250.00	2.88	-0.92	0.03	3.33	-2.63	0.0129	0.0251	-0.0603			0.2300	-0.26	3.80	-0.14	0.43	-12.71
300.00	2.76	-0.98	0.15	3.10	-2.37	0.0061	0.0207	-0.3001					1.93	-0.05	0.36	-6.21	
5-12-82	10.00	2.55	-0.11	0.06	5.95	-3.98	0.0148	-0.0099	-0.0014	830.3800	-5.3900	0.1700	0.05	2.44	-2.52	0.00	0.97
	22.00	2.64	-0.17	-0.29	5.78		0.0184	-0.0069	-0.0011		-2.5200	0.3600	0.09	3.12	-0.05	0.01	67.45
	50.00	3.03	-0.28	-0.07	5.42	-3.61	0.0272	0.0026	0.0038		342.2700	0.4800	-0.01	4.92	0.04	-0.01	-231.05
	100.00	2.84	-0.44	-0.10	4.94	-3.64	0.0111	0.0132	-0.0308		-1.1800	0.4900	0.00	2.20	-0.05	0.10	-45.50
	150.00	2.58	-0.48	-0.15	4.45	-3.14	0.0016	0.0074	-0.0383			0.4300	-0.06	0.35	-0.04	0.03	44.94
	200.00	2.95	-0.96	-0.14	4.02	-7.91	0.0027	0.0241	-0.0259			0.6500	0.16	0.66	0.18	0.25	-1.54
	250.00	2.71	-1.30	-0.02	3.37	-2.64	-0.0008	0.0123	-0.0584			0.1800	-0.31	-0.23	-0.06	0.40	0.69
300.00	2.64	-1.35	0.13	3.19	-2.37	0.0004	0.0311	-0.0902					0.12	-0.04	0.09	-2.63	
5-21-82	10.00		0.96	-0.05	15.91	-1.53	0.2146	0.3505	0.1064	841.0400	-0.3500	0.2900	0.17	13.22	0.00	1.02	-12.94
	22.00	1.19	-1.24	-0.40	15.62		0.1713	-0.0794	0.0539		-10.9900	0.6400	0.37	10.75	-7.87	-9.88	0.61
	50.00	1.45	-2.02	-0.05	14.98	-1.18	0.1113	0.0309	0.0526		-6.6100	0.6400	0.15	7.28	0.29	-1.47	6.18
	100.00	1.24	-2.67	-0.11	14.34	-1.04	0.1154	0.0931	0.2571		-50.8700	0.5500	0.06	7.89	-0.39	-3.34	2.11
	150.00	0.57	-2.49	-0.05	13.79	-0.67	0.0879	0.0104	0.1374			-0.7100	-1.20	6.25	-0.14	0.49	-17.58
	200.00				14.50	-0.67	0.0000	0.0000				1.3800	0.89	0.00	0.00	0.00	ERR
	250.00	0.27	-3.67	-0.60	13.12	-0.67	0.0699	-0.3354	0.3504			0.7300	0.24	5.22	-1.81	-25.72	0.19
300.00	0.34	-3.65	-0.36	12.39	-0.45	0.1391	-0.3583	0.2279					11.00	-0.50	0.09	26.80	

5-25-82	10.00	2.09	-4.65	-0.04	12.14	-3.71	0.1341	-0.2663	0.0141	836.7500	-85.2800	0.3900	0.27	10.83	-55.66	-0.66	0.19
	22.00	2.98	-5.50	-0.07	11.75	-3.57	0.1062	-0.3414	0.1296		-40.8400	0.5600	0.29	8.86	-25.32	-9.18	0.26
	50.00	3.33	-6.02	0.22	11.19		0.0931	-0.3046	0.1214		-9.8100	0.5300	0.04	8.15	-3.81	-2.25	1.35
	100.00	2.76	-5.94	0.28	10.66	-2.73	0.0781	-0.0107	0.1519		-1.1800	0.5200	0.03	7.18	0.12	0.24	-19.67
	150.00	2.90	-6.53	0.32	10.14	-2.18	0.1091	-0.1809	0.2212			0.0500	-0.44	10.54	-0.51	-2.61	3.38
	200.00		-6.89	0.33	10.09	-2.22	0.1115	0.4286	-0.8099			0.8800	0.39	10.83	-24.86	5.83	0.57
	250.00	3.06	-7.00	0.24	9.21	-1.85	0.1048	0.0549	0.3256			0.5500	0.06	11.15	3.36	-0.72	-4.22
300.00	3.22	-6.96		8.66		0.0796	0.0121	0.2213					9.01	0.04	0.18	-41.75	
5-26-82	10.00	-2.12	0.48		17.57	-2.53	0.0911	-0.1303	0.0834	832.0000	-43.7500	0.4400	0.32	5.08	27.62	0.40	-0.18
	22.00	-2.58	0.16	-0.49	17.13		0.1142	0.0346	0.0772		-4.7700	0.6500	0.38	6.53	-1.33	-2.06	1.93
	50.00	-2.48	0.25	-0.10	16.48	-2.24	0.0857	-0.0356	0.0551		-6.6100	0.5800	0.09	5.10	-0.13	0.18	-102.00
	100.00	-2.69	-0.01	-0.05	15.90	-2.17	0.1141	0.0364	-0.0446			0.5800	0.09	7.03	-0.15	0.23	-88.97
	150.00	-3.02	0.07	0.01	15.32	-1.89	0.0361	0.0674	0.0594			-1.6700	-2.16	2.31	-0.44	0.10	6.60
	200.00	-2.67	-0.08	-0.13	16.99	-1.77	0.0327	0.1116	0.1081			2.4900	2.00	1.89	0.78	-0.32	-4.13
	250.00	-2.80	-0.27	-0.25	14.50	-2.51	0.0628	0.2552	0.1048			0.6100	0.12	4.24	-0.66	-0.40	4.00
300.00	-2.81	-0.35	-0.31	13.89	-1.32	0.0987	-0.0398	0.2785					6.96	0.01	-0.45	15.91	

APPENDIX E

ANALYSES OF THE MEAN WIND

E.1 Analysis of the Mean Wind with a First Harmonic Fit

The mean wind is identified in the Browning and Wexler (1968) equations as the first harmonic (FH) analysis of the return. In order to better understand and identify the characteristics of the first harmonic (FH) fit using the least squares (LS) approach for actual field returns, the LS-FH technique was applied to synthetic conditions where known harmonic patterns would be analyzed. The LS-FH technique finds the minimum of

$$\sum (V_i - A_0 - A_1 \cos\theta_1 - B_1 \sin\theta_1)^2$$

for $i = 1$ to n . Noise, multiple higher harmonics, and portions of cycles were placed into the model data to help identify any problems that might be expected in using the LS-FH technique to analyze the mean wind.

Table E.1 gives the results for a number of runs on synthetic VAD data. Overall, it can be seen that the degree the LS-FH technique properly reflects the known first harmonic varies with the phase of the added multiple harmonics. With incomplete cycle data and no noise the first harmonic is always mirrored by the technique. Unfortunately, experimental conditions always contain noise, both from atmospheric and instrumental sources.

The first step in analyzing the LS-FH fit was to add noise (1 m/s) to a known first harmonic. Results of analyzing various tenths of complete cycles were evaluated. For two-tenths of a complete cycle (72°) using synthetic data, the LS-FH fit gave mean wind information that varies from 0.18° to 2.21° off in direction and from 88.6% to 109.7% off in wind speed. When the synthetic data were increased to 1440 or greater, the total wind speed and direction as estimated by the LS-FH fit was within 99% for all combinations of analyzed angles.

Since the original Browning and Wexler derivation included theoretical applications for the second harmonic, a second harmonic was added to the synthetic data and the LS-FH fit was again processed to a number of data combinations. Theoretically, analyzing harmonic data over less than a full cycle requires analysis of multiple harmonic cross terms. The LS-FH technique calculates only cross terms for the first harmonic values. Some degree of uncertainty was

expected in the wind estimate, owing to the absence of the additional cross terms. When the synthetic data without noise were processed, the routine overestimated the wind speed for portions of a cycle greater than 40% and for all angles of incidence. The LS-FH calculated wind direction ranges from more than 90° to less than 2° off the expected values for the differing cycles. Once the data covered more than one cycle, the wind direction estimate was within 5° of the actual value but the wind speed was still overestimated.

When noise was added to the first and second harmonic synthetic data, the LS-FH fit gave a wide range of errors in both the wind speed and wind direction estimates. In addition to the difficulties in estimating wind speed and direction, a large offset was calculated by the LS-FH fitting routine. Since the offset number theoretically represents the vertical velocity over the area, large calculated offsets remove any possible uses for the vertical velocities calculated by the technique.

Finally, other possible experimental conditions were modeled through the LS-FH fitting routine. Twenty-first, sixth, and third harmonics were added to the synthetic data to attempt a reasonable estimate of a boundary layer. Cases representing the different phase relationships to the first harmonic were tested. The added harmonics caused erratic behavior in the fitted LS-FH, and no pattern emerged.

E.2 Analysis of the Mean Wind with a First and Second Harmonic Fit

An alternative technique to a first harmonic fit for VAD data is to combine the first and second harmonics (FSH) in a least-squares (LS) fit. The LS-FSH technique minimizes

$$\sum (V_i - A_0 - A_1 \cos\theta_1 - B_1 \sin\theta_1 - A_2 \cos\theta_2 - B_2 \sin\theta_2)^2$$

for $i = 1$ to n . In circumstances where a first and second harmonic are expected to be present in the experimental data, the combination fit should better estimate the mean wind in the first harmonic section of the fit. When synthetic data were processed through the LS-FSH fit, various degrees of accuracy resulted.

When only a first harmonic without noise was present in the synthetic data and the LS-FSH fit was used, the fit exactly reproduced the test harmonic. When noise (10% to 20% of the mean wind value) was added to a first harmonic and fitted, the results were erratic. For 72° of data, the fit was off as much as 180° in direction and gave speeds that ranged from half the expected value to 3 times the model data. When the percentage of a complete cycle was increased to 30%, the fit improved with only a slight overspeeding of the mean wind and a small directional offset. When the amount of the cycle available was increased to over 40% the LS-FSH fit reproduced the model data better than the LS-FH fit did.

The final case study was a synthetic data set containing both a first and second harmonic with and without noise. The results for the LS-FSH fit indicated erratic behavior even in some cases where 75° of the cycle was available. The degree the LS-FSH reproduced the synthetic data was dependent on the exact relationship of the phases of the harmonics used in the fit.

E.3 Conclusions

Since pro forma information of the phase of experimental data is not available, it was judged that the LS-FSH approach was too erratic to be used for experimental data sets. Model results were inconsistent for incomplete cycles so in addition to specifying a LS-FH fit, it was concluded that data sets representing complete cycles would best recover the first harmonic, and fit the mean wind and direction over the areas used in the lidar VAD data analysis.

Table E.1. Samples of least squares algorithm fit test results

Case 1	Noise = 0		Offset = 0	Second Harmonic - 2.5 m/s						LS-FSH fit perfect	
al - input value											
4.9749	4.8990	4.7697	4.5826	4.3301	4.0000	3.5707	3.0000	2.1797	0.0000		
al - LS-FH fit											
11.2269	11.1509	11.0216	10.8345	10.5820	10.2519	9.8226	9.2519	8.4314	6.2519	% Wave 20	
8.5473	8.4713	8.3420	8.1549	7.9025	7.5723	7.1430	6.5723	5.7518	3.5723	40	
6.7313	6.6553	6.5260	6.3389	6.0865	5.7563	5.3271	4.7563	3.9358	1.7563	60	
6.1644		5.9592	5.7720	5.5196	5.1895	4.7602	4.1895	3.3689	1.1895	80	
4.9749	4.8990	4.7697	4.5826	4.3301	4.0000	3.5707	3.0000	2.1797	0.0000	100	
5.2943	5.2184	5.0891	4.9020	4.6495	4.3194	3.8901	3.3194	2.4988	0.3194	120	
a2 - input value											
0.5000	1.0000	1.5000	2.0000	2.5000	3.0000	3.5000	4.0000	4.5000	5.0000		
a2 - LS-FH fit											
6.7339	7.2339	7.7339	8.2339	8.7339	9.2339	9.7339	10.2339	10.7339	11.2339	% Wave 20	
3.6903	4.1903	4.6903	5.1903	5.6903	6.1903	6.6903	7.1903	7.6903	8.1903	40	
-1.4739	-0.9739	-0.4739	0.0261	0.5261	1.0261	1.5261	2.0261	2.5261	3.0261	60	
-0.4595	0.5405	1.0405	1.5405	2.0405	2.5405	3.0405	3.5405	4.0405	4.5405	80	
0.5000	1.0000	1.5000	2.0000	2.5000	3.0000	3.5000	4.0000	4.5000	5.0000	100	
0.8099	1.3099	1.8099	2.3099	2.8099	3.3099	3.8099	4.3099	4.8099	5.3099	120	
offset - LS-FH fit											
-6.3598	-6.3598	-6.3598	-6.3598	-6.3598	-6.3598	-6.3598	-6.3598	-6.3598	-6.3598	% Wave 20	
-2.7910	-2.7910	-2.7910	-2.7910	-2.7910	-2.7910	-2.7910	-2.7910	-2.7910	-2.7910	40	
1.4444	1.4444	1.4444	1.4444	1.4444	1.4444	1.4444	1.4444	1.4444	1.4444	60	
0.8088	0.8088	0.8088	0.8088	0.8088	0.8088	0.8088	0.8088	0.8088	0.8088	80	
0.0000	0.0000	0.0000	0.0000	0.0000	0.0000	0.0000	0.0000	0.0000	0.0000	100	
0.2294	0.2294	0.2294	0.2294	0.2294	0.2294	0.2294	0.2294	0.2294	0.2294	120	

Case 2	Noise = 1		Offset = 0	Second Harmonic - 0							
				a1 - input value							
9.9498	9.7980	9.5394	9.1652	8.6602	8.0000	7.1414	6.0000	4.3588	0.0000		
				a1 - LS-FH fit							% Wave
9.9501	10.6665	9.3995	8.2398	8.6441	7.6557	7.4374	5.8636	4.7202	0.3934	20	
9.9354	9.8304	9.6523	9.2262	8.6421	7.8842	7.1604	6.0214	4.4482	0.0084	40	
9.9195	9.8448	9.5251	9.1450	8.6334	8.0094	7.1625	5.9714	4.3778	0.0262	60	
9.9848	9.8400	9.5971	9.1557	8.6874	7.9955	7.2016	6.0959	4.3991	0.0061	80	
9.9203	9.8049	9.6028	9.1713	8.6894	8.0057	7.2150	5.9735	4.3019	0.0463	100	
9.9936	9.7748	9.5435	9.1182	8.7197	8.0233	7.1611	6.0533	4.3877	-0.0473	120	
				a2 - input value							
1.0000	2.0000	3.0000	4.0000	5.0000	6.0000	7.0000	8.0000	9.0000	10.0000		
				a2 - LS-FH fit							% Wave
0.9736	2.5426	2.9870	3.2491	4.9550	5.6304	7.1251	8.0488	9.2192	10.2087	20	
1.0713	1.8216	2.8348	4.1949	4.8943	5.9753	7.2803	7.9140	9.0649	10.2818	40	
0.9393	1.8974	3.0696	3.9659	4.9574	6.0320	7.0601	7.9393	8.9136	9.8830	60	
0.9446	2.0721	2.9896	3.9690	5.0696	5.9412	6.9734	8.0530	9.0036	10.0167	80	
0.9966	1.9693	3.0121	4.0437	5.1168	5.9408	6.9730	8.0110	8.9601	9.9663	100	
1.0060	2.0818	2.9447	3.9791	5.0321	5.9659	7.1397	8.0441	8.9984	10.0175	120	
				offset - LS-FH fit							% Wave
0.0527	-0.9619	0.1739	1.1412	0.0152	0.4597	-0.2487	0.0144	-0.3808	-0.4255	20	
-0.0731	0.1538	0.0658	-0.1855	0.0729	0.0026	-0.1814	0.1171	-0.0608	-0.2140	40	
0.0527	-0.0389	-0.0501	0.0247	0.0419	-0.0122	-0.0224	0.1021	0.0482	0.0577	60	
-0.1000	0.0204	0.0082	-0.0026	0.0197	0.0121	0.0417	-0.0525	0.0008	-0.0251	80	
-0.0162	0.0301	0.0322	0.0026	-0.0133	0.0333	-0.0193	0.0068	-0.0081	0.0467	100	
-0.0217	-0.0209	-0.0582	0.0004	-0.0537	-0.0334	0.0158	-0.0186	0.0156	0.0000	120	

Case 3 Noise = 1 Offset = 0 Second Harmonic - 5

a1 - input value										
4.9749	4.8990	4.7697	4.5826	4.3301	4.0000	3.5707	3.0000	2.1794	0.0000	
a1 - LS-FH fit										% Wave
4.0866	4.8852	3.7394	2.7671	3.4449	2.7711	2.9838	1.9786	1.6539	-0.4949	20
11.0356	11.0110	10.9579	10.7198	10.3883	9.9591	9.6645	9.0996	8.3451	6.0854	40
8.8325	8.8343	8.6452	8.4507	8.1911	7.8974	7.4800	6.8605	6.0868	3.9143	60
7.6413	7.5735	7.4580	7.2044	6.9893	6.6261	6.2631	5.7289	4.8521	2.6399	80
4.9467	4.9068	4.8345	4.5890	4.3585	4.0063	3.6438	2.9736	2.1213	0.0496	100
5.7528	5.6115	5.5093	5.2720	5.1286	4.7587	4.3270	3.7888	2.9430	0.6883	120
a2 - input value										
0.5000	1.0000	1.5000	2.0000	2.5000	3.0000	3.5000	4.0000	4.5000	5.0000	
a2 - LS-FH fit										% Wave
0.1478	1.2213	1.1609	0.9221	2.1428	2.3064	3.3036	3.7242	4.3943	4.8837	20
3.2573	3.5168	4.0211	4.8863	5.0832	5.6647	3.4644	6.6070	7.2551	7.9737	40
-4.6452	-4.1880	-3.4920	-3.1211	-2.6278	-2.0576	-1.5287	-1.1505	-0.6758	-0.2038	60
-1.5436	-0.9190	-0.4956	-0.0195	0.5530	0.9528	1.4849	2.0643	2.5149	3.0287	80
0.4983	0.9697	1.5123	2.0457	2.6150	2.9411	3.4725	4.0131	4.4593	4.9653	100
1.0417	1.6199	1.9808	2.5154	3.0662	3.5039	4.1740	4.5842	5.0335	5.5539	120
offset - LS-FH fit										% Wave
4.7100	3.6881	4.8326	5.8002	4.6501	5.1129	4.4018	4.6682	4.2745	4.2310	20
-2.4036	-2.1845	-2.2647	-2.5193	-2.2599	-2.3281	-2.5106	-2.2191	-2.3935	-2.5484	40
3.8051	3.7935	3.7043	3.7779	3.7953	3.7672	3.7321	3.8570	3.8026	3.8115	60
1.7544	1.7848	1.7731	1.7615	1.7841	1.7751	1.8063	1.7119	1.7659	1.7403	80
-0.0154	0.0305	0.0319	0.0030	-0.0131	0.0333	-0.0187	0.0062	-0.0090	0.0467	100
0.4671	0.4664	0.4294	0.4883	0.4334	0.4543	0.5026	0.4699	0.5031	0.4876	120

Case 3 Noise = 1 Offset = 0 Second Harmonic - 5

a1 - input value										
4.9749	4.8990	4.7697	4.5826	4.3301	4.0000	3.5707	3.0000	2.1794	0.0000	
a1 - LS-FSH fit										% Wave
*****	*****	*****	*****	*****	*****	*****	*****	*****	*****	20
-4.5794	-5.2063	-4.4154	-5.0123	-5.8509	-6.1379	-6.0793	-6.5469	-7.6292	-9.5694	40
6.1935	6.1100	6.0073	5.8642	5.5506	5.3605	4.9168	4.2123	3.4918	1.2124	60
5.4326	5.3206	5.1801	4.9745	4.7659	4.3949	4.0358	3.4931	2.6523	0.4032	80
4.9481	4.9091	4.8339	4.5871	4.3576	4.0071	3.6440	2.9708	2.1207	0.0435	100
5.1091	4.9627	4.8570	4.6274	4.4860	4.1067	4.6942	3.1607	2.3014	0.0458	120
a2 - input value										
0.5000	1.0000	1.5000	2.0000	2.5000	3.0000	3.5000	4.0000	4.5000	5.0000	
a2 - LS-FSH fit										% Wave
*****	*****	*****	*****	*****	*****	*****	*****	*****	*****	20
-28.4719	-30.0502	-27.0739	-26.4477	-28.3455	-27.0753	-25.5497	-24.6871	-25.0494	-23.7309	40
-3.2040	-2.5612	-1.9521	-1.7412	-1.3143	-0.9211	-0.3655	0.1564	0.7396	1.3048	60
0.2769	0.9168	1.3674	1.8135	2.3877	2.7842	3.3146	3.9146	4.3310	4.8735	80
0.5002	0.9726	1.5114	2.0478	2.6162	2.9444	3.4757	4.0102	4.4592	4.9656	100
0.4393	1.0098	1.3814	1.9134	2.4687	2.8962	3.5813	3.9939	4.4383	4.9531	120
offset - LS-FSH fit										% Wave
*****	*****	*****	*****	*****	*****	*****	*****	*****	*****	20
21.1690	22.6927	20.8527	20.8269	22.5320	21.9922	21.2719	21.0847	21.6234	21.0183	40
2.5034	2.3702	2.3462	2.5205	2.5657	2.6588	2.6024	2.6294	2.5232	2.5232	60
0.2398	0.2465	0.2176	0.2340	0.2605	0.2480	0.2816	0.1762	0.2574	0.2076	80
-0.0151	0.0316	0.0331	0.0047	-0.0164	0.0352	-0.0193	0.0076	-0.0090	0.0479	100
0.0074	0.0098	-0.0296	0.0517	-0.0204	-0.0075	0.0543	0.0266	0.0462	0.0348	120